CHARACTERISATION AND PREPARATION OF SUPERCONDUCTING DIAMOND FILMS FOR THE PRODUCTION OF NEMS AND SQUIDS

by

Jessica Mary Werrell

A THESIS SUBMITTED TO CARDIFF UNIVERSITY
FOR THE DEGREE OF DOCTOR OF PHILOSOPHY

SEPTEMBER 2018

'Human beings always do the most intelligent thing; after they've tried every stupid alternative and none of them have worked.'

R. BUCKMINSTER FULLER

Abstract

Boron doped nanocrystalline diamond has intrinsic properties (namely a high young's modulus to density ratio) that make it an appealing material for the construction of nano-electro-mechanical systems and superconducting quantum interference devices; which can then be used to investigate macroscopic quantum states. This thesis seeks to characterize the superconducting properties of films of this material, as measured by AC susceptibility and magnetic relaxation, in preparation for its use in the aforementioned fabrications. The properties under investigation using the AC susceptibility are the superconducting volume fraction of the sample, its critical temperature and critical current density. This thesis investigates how these properties change for diamond films grown to different thicknesses, 160 - 564 nm. It is shown that all films consist of a hundred percent superconducting material; although these typical volume fraction calculations simplify the results such that details of the transition are lost. The critical temperature is shown to be in close agreement with a critical temperature calculated considering fluctuating conduction behaviour from resistivity measurements. This thesis also gives further evidence for the recently discovered superconducting glass state within diamonds phase diagram. A pinning potential is also calculated for the thickest diamond sample in the set; which is a factor of 2 smaller than the only published value of diamond available. This difference is likely due to the growth and measurement set up variations. Finally this thesis shows how simple improvements can be made the chemical mechanical polishing of this material, which will ultimately improve device performance.

ACKNOWLEDGEMENTS

I have many people to thank for reaching this stage. The first must go to my supervisors Professor Oliver Williams and Dr Sean Giblin, without whom none of this would have been possible. Thank you for your guidance, your patience, your scientific knowledge and availability throughout the past four years of my life.

Next, everyone in the Cardiff Diamond foundry, old and new. Specifically thank you to the post-docs Dr. Soumen Mandal and Dr. Georgina Klemencic. Thank you Soumen for day to day lab assistance and training me on all the various diamond lab equipment over the years, in particular the CMP and CVD systems. Thank you also for growing the BNCD samples for this thesis. Thank you to Georgina for working with me in our collaborative efforts with diamond characterisation; your work is referenced in relation to mine in the appropriate chapters. Thank you both as well for all the scientific discussions over the years and answering all my questions. Without your skills and input I would not have found myself up to this task. Additionally thank you so much to Dr Evan Thomas and Dr Laia Ginés for helping me keep my sanity the past four years. Evan you were always able to support me if I needed it; Laia you will always be my PhD sister. My time in Cardiff was merrier with you both filling it with good food, cheer and terrible singing.

For assistance with AFM thanks are owed to Dr Emmanuel Brousseau here at Cardiff, while the XPS measurements of the sample were taken by Ryan Lewis, under the supervision of Professor Paola Borri.

Thank you to my housemates in Cardiff and various friends both near and far. Life should be filled with good people and I have been lucky that this has been the case. Special mention must go to my housemate of the past two years, the best of Chrises, Dr Christopher Clark. It truly was an excellent two years, I would not change a thing. Also thank you to Sarah Jaffa for being such a good study buddy.

Last but of course not least, I must thank my family. Especially Mum, Dad, Ed and Sammy, the four of you have rallied fantastically to supported me in all your unique ways over the past four years. The last few months of thesis writing, in particular, would have been almost impossible without my parents. I am lucky to have such a support group of love and encouragement, thank you.

PUBLICATIONS AND CONFERENCE TALK

1. Jessica Werrell, Soumen Mandal, Evan Thomas, Oliver Williams, "Chemical Mechanical Polishing (CMP) of Thin Diamond Film - Effect of Slurry Composition on Polishing", in 2016 MRS Fall Meeting & Exhibit, Symposium EM12 : Diamond Electronics, Sensors and Biotechnology-Fundamentals to Applications

2. G. M. Klemencic, S. Mandal, J. M.Werrell, S. R. Giblin, and O. A.Williams, "Superconductivity in planarised nanocrystalline diamond films", Science and Technology of Advanced Materials, vol. 18, no. 1, pp. 239-244, 2017.

3. G. M. Klemencic, J. M. Fellows, J. M. Werrell, S. Mandal, S. R. Giblin, R. A. Smith, and O. A. Williams, "Fluctuation spectroscopy as a probe of granular superconducting diamond films," Phys. Rev. Materials, vol. 1, p. 044801, Sep 2017.

4. J. M. Werrell, S. Mandal, E. L. H. Thomas, E. B. Brousseau, R. Lewis, P. Borri, P. R. Davies, and O. A. Williams, "Effect of slurry composition on the chemical mechanical polishing of thin diamond films", Science and Technology of Advanced Materials, vol. 18, no. 1, pp. 654-663, 2017.

5. G. M. Klemencic, J. M. Fellows, J. M. Werrell, S. Mandal, S. R. Giblin, R. A. Smith, and O. A. Williams, "Observation of a superconducting glass state in granular superconducting diamond", Submitted to Phys. Rev. Materials, March 2018

Contents

List of Tables

List of Figures

CHAPTER 1
INTRODUCTION

1.1 PROJECT MOTIVATION

The work conducted for this thesis is part of a larger project which aims to first, fabricate and characterise diamond superconducting nano-electro-mechanical systems (NEMS) and superconducting quantum interference devices (SQUIDS); then use these devices to investigate macroscopic quantum states.

The NEMS of particular interest is a doubly clamped bridge cantilever. The fundamental characteristics of a mechanical resonator are determined by the resonance frequency (f_0) and dissipation or inverse quality factor (Q^{-1}) (1). f_0 of a doubly clamped bridge cantilever is given by the following:

$$f_0 = 1.028\sqrt{\frac{E}{\rho}}\frac{d}{L^2} \tag{1.1}$$

where E is the Young's modulus, ρ the density and L and d are the length and thickness of the cantilever respectively (1). Importantly if it is assumed that all materials have similar micro-fabrication possibilities, then it can be seen from equation (1.1) that the material with the highest E/ρ quotient will result in the highest resonant frequency. Materials commonly used for NEMS are shown in figure 1.1.

There are various mechanisms which influence Q^{-1}. The total dissipation is the sum of contributions from each dissipation mechanism, and can be written as:

$$Q_{\text{tot}}^{-1} = \frac{\Delta W}{2\pi W} = \frac{1}{2\pi W}\sum_i \Delta W_i = \sum_i Q_i^{-1} \tag{1.2}$$

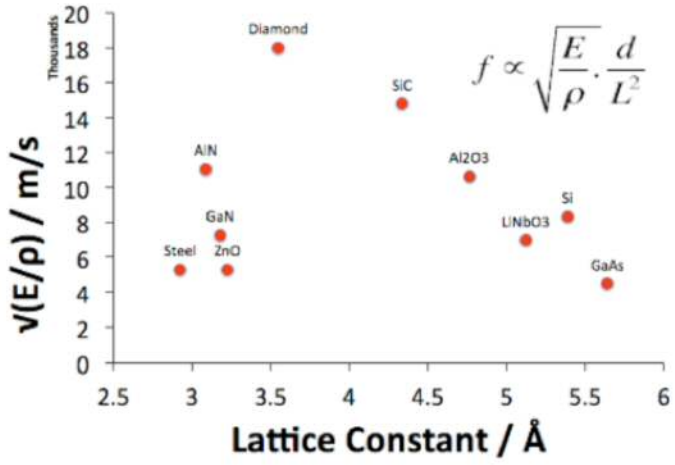

FIGURE 1.1 Comparison of the mechanical properties of diamond compared to other commonly used cantilever materials. *Å* being short hand for the unit *ångström*. Image taken from (2).

where W is the total mechanical energy in the system and ΔW is the energy lost per cycle of oscillation (1). It has been shown that two of the dominant dissipation mechanisms for a doubly clamped bridge cantilever are the clamping losses and surface losses (3). Clamping losses occur whenever mechanical strain energy is concentrated at the attachment points of the structure. The surface losses is a general term which includes contributions from surface defects, impurity atoms, dangling bonds, and crystal defects. These losses have the following forms

$$\begin{aligned} Q^{-1}_{\text{clamping losses}} &= \alpha \frac{w}{L} \\ Q^{-1}_{\text{surface losses}} &= \frac{2\delta(3w+t)}{wt} \frac{E^2_{\text{ds}}}{E} \end{aligned} \tag{1.3}$$

where w is the width of the beam, E_{ds} is the surface's Young's modulus, which differs from that of the bulk precisely due to the defects, and can be used to characterize the material up to a skin depth δ, α is a material dependent coefficient (1). These are only two examples of the dissipation methods that affect the doubly clamped bridge cantilever. For this discussion, it is not necessary to go into all the various forms of Q^{-1} as it has been found that broadly $Q_{\text{tot}} \propto \text{volume}^{1/3}$ over a large size range (1).

Natural diamond is an electrical insulator well known for its exceptional hardness. Nano-crystalline diamond (NCD) thin films grown by chemical vapour deposition (CVD) are able to retain many of the properties of single crystal diamond and can be produced with high quality at relatively low cost (4; 5). Diamond

can be made superconducting by doping it with boron (6; 7). Boron doped nanocrystalline diamond (BNCD) whilst having different electrical properties still has the same Young's modulus as NCD films (8). As can be seen in figure 1.1, diamond has a E/ρ quotient that is significantly higher than all other materials, including any other superconductors. Cantilevers in undoped diamond have already been shown to resonate at 1.4 GHz, although these are not of the clamped variety, and superconducting diamond cantilevers have been fabricated with resonant frequencies up to 10 MHz (8). Choosing diamond with its high E/ρ allows for construction of larger cantilevers of the same high f_0 according to equation (1.1), which in turn increases its Q_{tot}.

A f_0 of the order of a GHz and a high Q_{tot} is desirable because it allows a resonating cantilever to enter its quantum ground state (lowest-energy state) at temperatures below 20 mK (2); temperatures which are achievable in commercial dilution refrigerators. For a macroscopic object, such as a cantilever, to enter the ground state of a mechanical mode the thermal occupation factor (N) must approach $1/2$. N is set by the mode frequency ω and the device temperature T. A mode of the oscillating system is a pattern of motion in which all parts of the system move sinusoidally with the same frequency, and with a fixed phase relation. A cantilever oscillating at its f_0 is in a single mode of the system. The average fluctuating energy $< E >$ of a mode coupled to a thermal bath can be defined by:

$$< E >= \hbar\omega N = \hbar\omega\left(\frac{1}{2} + \frac{1}{\exp(\frac{\hbar\omega}{k_B T}) - 1}\right) \tag{1.4}$$

where k_B is the Boltzmann constant, and N follows the Bose-Einstein distribution. N is able to follow this distribution as it represents a mode coupled to a thermal bath which results in energy fluctuations. For high temperatures, this expression reduces to the classical equipartition of energy: each mode carries $k_B T$ of energy (9). Figure 1.2 shows how N varies with frequency and temperature. Broadly the ground state is reached at higher temperatures for higher resonant frequencies.

This project aims to insert this cantilever into the loop of a BNCD DC SQUID. A DC SQUID being a loop of superconducting material containing two Josephson junctions. A Josephson junction is made from two superconducting electrodes that are spatially separated by a thin barrier; which allows the electrons, or in the superconducting state, Cooper-paired electrons, to tunnel through. The current through the device is functionally dependent on the phase difference

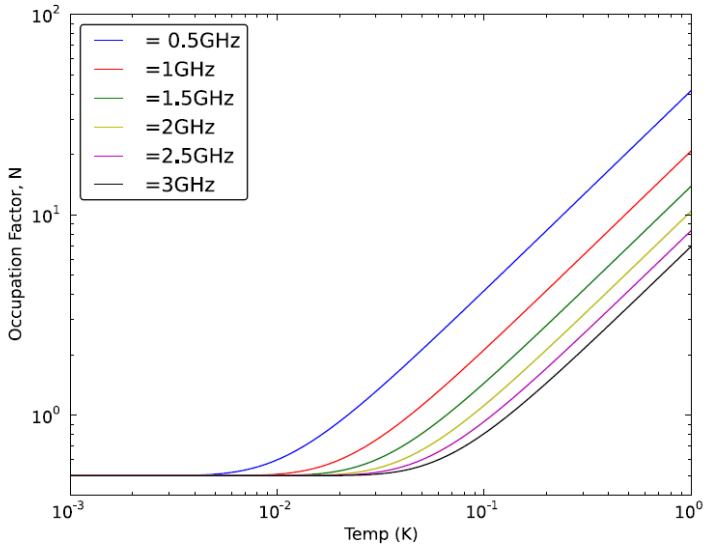

FIGURE 1.2 The occupation factor N of various mechanical cantilever frequencies as a function of temperature is shown for samples with different resonant frequencies. Image taken from (2).

across it. The SQUID acts as a highly sensitive on-chip position detector for the resonating cantilever. The use of BCND films will allow for the construction of a simple integrated circuit which can then serve as a stepping stone for an integrated cantilever entangled with a phase qubit. A phase qubit being a current-biased Josephson junction, operated in the zero voltage state with a non-zero current bias. Figure 1.3 shows a schematic of the integrated SQUID and cantilever.

The project uses the same set up as the work of Etaki *et al.* (10), which was instrumental in the motion detection of a micro mechanical cantilever embedded in a DC SQUID. However they were not able to get the niobium resonator to the ground state, only achieving an occupation factor of $N = 878$. The niobium cantilever constructed for the Etaki *et al.* project had a resonator with a natural frequency of 2 MHz with a E/ρ ratio of 3400 m/s (10; 2). This project aims to exploit diamond's higher E/ρ ratio of to reach the quantum ground state at higher temperatures.

In order to reach this final goal there are numerous fabrication and characterisation aims to achieve first. There are three areas of interest, split over three chapters, that this thesis focuses on with this overarching goal in mind. Firstly the superconductivity of the BCND films is still an area of active interest. This thesis has two components that focus on characterising particular superconducting aspects of the

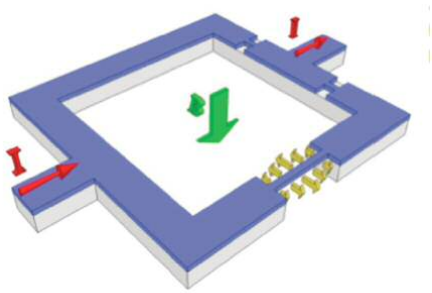

FIGURE 1.3 A schematic of the integrated SQUID and cantilever. B=applied magnetic field, I=current. (2)

BNCD films. The first uses an AC susceptibility technique to measure how the critical temperature, superconducting fraction of the film and critical current density changes with film thickness. The second is a discussion and measurement of the temperature dependence of what could be a vortex glass state within boron doped diamond's phase diagram. The final area of interest is concerned with improving the chemical mechanical polishing (CMP) of the thin films; a necessary production step, which improves device performance, before device construction. The organisation of the thesis content is as follows:

- Chapter 2 is an introduction to basics concepts within the field of superconductivity. It has been written as a guide to aid understanding of the diamond superconductivity discussion in chapter 3 and the magnetic experiments covered in chapters 4 and 5.

- Chapter 3 is split into three sections. The first discusses common diamond growth methods, in particular the CVD method which was used to grow the films for this thesis. Next this chapter gives a discussion on the current understanding of boron doped diamond's superconductivity. The final section details the growth conditions of the NCD and BNCD films grown for this thesis.

- Chapter 4 uses the AC susceptibility of the BNCD films to investigate how the critical temperature, critical current density and percentage of film which is superconducting changes with film thickness. These films are granular and therefore a change in thickness will result in a change in crystal size and number of grain boundaries; understanding how these changes affect the aforementioned properties is necessary for device construction. The critical temperature results of these films are compared and discussed against published resistivity results of the same films (11). Critical current density values

are calculated and compared against current literature values for diamond. Typical volume fraction calculations show that all the films, so regardless of thickness, are comprised of 100% superconducting material. These results however remove all superconducting transition details which suggests that the approach is too simplistic for these materials.

- Chapter 5 discusses the magnetic relaxation measurement of the thickest BNCD film. It is a continuation of the work set out in ref. (12) of a possible vortex glass state in boron doped diamond's phase diagram. These results are also used to calculate an effective pinning potential energy for the film which is found to be a factor of 2 smaller than the only other published result for diamond (13), a variation that could be due to differences in measurement set up and sample growth conditions.

- Chapter 6 concerns improvements made to the chemical mechanical polishing (CMP) of NCD thin films (14). This process is vital to reduce the as grown surface roughness of the films and improve the construction and performance of the NEMS and SQUIDS.

- Chapter 7 to finish draws together the results of the chapters and concludes the thesis.

CHAPTER 2
THEORY

This chapter will introduce some of the key ideas, in predominantly phenomenological terms, from the field of superconductivity that are essential for understanding the experimental results presented in chapters 4 and 5. More detailed material will be highlighted in later chapters as necessary.

2.1 SUPERCONDUCTIVITY BASICS

2.1.1 OVERVIEW

Superconductivity was first measured in mercury, by Onnes (15; 16; 17), as a sharp transition to an immeasurably small resistance at 4.2 Kelvin (K). All elemental metals show a decrease in electrical resistance with reduced temperature however this sharp transition to effectively zero resistance was a surprising discovery. Further measurements of known superconductors by Meissner and Ochsenfeld in 1933; found that whilst below their transition temperature (T_C) they also completely expelled any magnetic field from their interior. This property would not be shown by a perfect conductor and (with injustice to Ochsenfeld) it became known as the Meissner effect. This effect has an important impact on any electric currents that flow along it; currents cannot pass through the body of a superconducting material, but flow only on the surface. The London equations, proposed by Fritz and Heinz London in 1935 (18), relate the superconducting current to the electromagnetic fields in and around a superconductor. They will be discussed further in section 2.1.1.

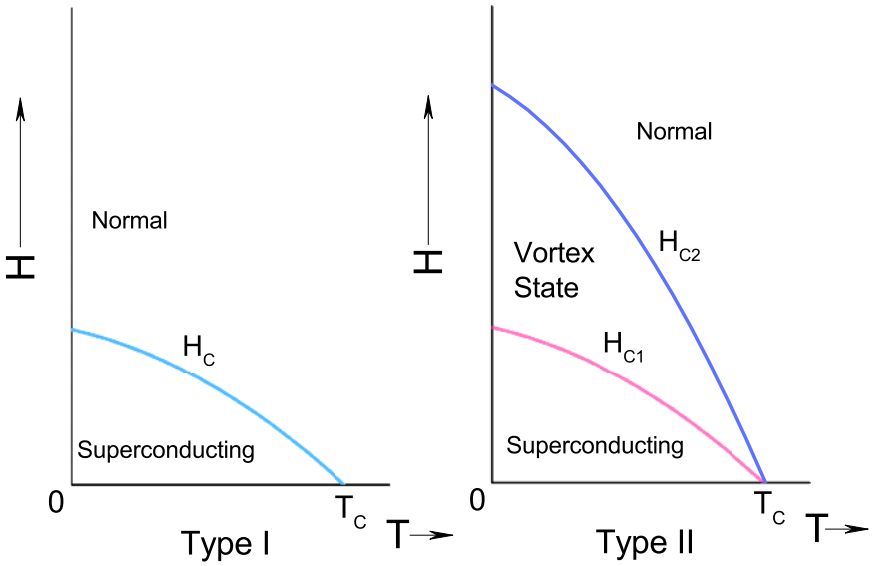

FIGURE 2.1 Phase diagrams of type I and type II superconductors. Adapted with permission from page 183 of Ref. (19), Copyright Elsevier (1969).

It was later discovered that there are two classes of superconductors, called Type I and II. Type I refers to superconductors which exhibit a Meissner effect below a critical field (H_C) and T_C. Type II superconductors were experimentally discovered in 1935 by Rjabinin and Shubnikov (20); they display the Meissner effect up to a lower critical field (H_{C1}) and then exhibit partial field penetration till an upper critical field (H_{C2}), when they become normal. The region of $H_{C1} \leq H \leq H_{C2}$ is called the vortex or mixed state. This thesis will refer to it as the vortex state and it will be discussed in more detail in section 2.2. Figure 2.1 shows examples of the phase diagrams of type I and II.

Preceding the discovery of high T_C superconductors all the important features of superconductivity could be explained by the Bardeen-Cooper-Schrieffer (BCS) theory (21), which will be discussed further in section 2.1.4. Boron doped nanocrystalline diamond (BNCD) films are granular in nature, their growth and the properties of the films grown for this thesis will be discussed in chapter 3. The BNCD grains have been shown to broadly agree with BCS-like superconductivity (22) (23). The grain boundaries have been reported to show predominantly metallic-like conductance (12). They are also dirty superconductors (7; 24; 23), a term which is defined in section 2.1.5. These results and the experiments that found them will be discussed in chapter 3.

This thesis is interested in the magnetization behaviour of said BNCD films, so section 2.2.3 describes the expected magnetization behaviour of type I and II superconductors. Section 2.2.4 introduces the Bean's Critical state model and section 2.2.5 the basics of magnetic relaxation which are relevant for calculations in chapters 4 and 5 respectively.

2.1.2 THE LONDON EQUATIONS

There are two equations, the first (2.1) describes the resistance less property of a superconductor, there being no electric field (**E**) in the material unless the current is changing; and the second (2.2) relating current to the magnetic flux density (**B**) inside the superconductor.

$$\frac{d\mathbf{J}_s}{dt} = \frac{n_s e^2}{m}\mathbf{E} \tag{2.1}$$

$$\mathbf{B} = -\frac{m}{n_s e^2}\left(\nabla \times \mathbf{J}_s\right) \tag{2.2}$$

where $\mathbf{J}_s$ is the superconducting current density, n_s is the density of the particles carrying the superconducting current, m and e are their mass and charge respectively in SI units. The London equations are only approximations, though for many purposes they are sufficiently accurate.

2.1.2.1 DERIVING THE FIRST LONDON EQUATION

The equation (2.1) was initially informally derived using classical mechanics (18). Substances across a very wide range of composition behave roughly according to Ohm's law, which states that current is proportional to electric field. However this linear relationship does not hold for superconductors because they have no resistance i.e. there is no opposition to the motion of the current so it will increase even as the field remains constant. The London brothers described the acceleration of the superconductor's electrons (super-electrons) with an applied **E** as

$$m\frac{d\mathbf{v_s}}{dt} = e\mathbf{E} \tag{2.3}$$

where $\mathbf{v_s}$ is the velocity for the super-electrons. Then they considered a unit volume (V) of the superconductor, represented by figure 2.2, where the super-electrons are uniformly distributed resulting in a charge (Q_s).

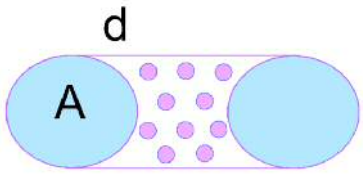

FIGURE 2.2 Schematic of a shape containing uniformly distributed charge where volume V = Ad.

In this situation the super-current can be represented by

$$I_s = \frac{Q_s}{t} \tag{2.4}$$

Q_s can be re-written to include the number of super-electrons (n_s) per unit volume

$$Q_s = V n_s e \tag{2.5}$$

The super-electrons have the drift speed v_s and as V=Ad it is possible to re-write (2.5) into

$$Q_s = A v_s t n_s e \tag{2.6}$$

So the current density (J_s) through this sample becomes

$$J_s = \frac{I}{A} = \frac{Q_s}{At} = v_s n_s e \longrightarrow J_s = v_s n_s e \tag{2.7}$$

Differentiating (2.7) gives

$$\frac{dJ_s}{dt} = n_s e \frac{dv_s}{dt} \tag{2.8}$$

which can be re-arranged to

$$\frac{dv_s}{dt} = \frac{1}{n_s e} \frac{dJ_s}{dt} \tag{2.9}$$

(2.9) can be substituted into (2.3)

$$\frac{m}{n_s e} \frac{d\mathbf{J}_s}{dt} = e\mathbf{E} \tag{2.10}$$

(2.10) can then be re-arranged to give (2.1) the first London Equation.

2.1.2.2 DERIVING THE SECOND LONDON EQUATION

A magnetic field is related to an electric field and current (**J**) by the following Maxwell equations

$$\frac{d\mathbf{B}}{dt} = -\nabla \times \mathbf{E} \tag{2.11}$$

$$\nabla \times \mathbf{H} = \mathbf{J} + \frac{d\mathbf{D}}{dt} \tag{2.12}$$

where **D** is the electric displacement field, **B** is the magnetic flux density and **H** is the magnetic field. The **H** and **B** fields are related by the relation

$$\mathbf{B} = \mu_0(\mathbf{H} + \mathbf{M}) \tag{2.13}$$

where μ_0 is the permeability of free space or vacuum permeability and **M** is the magnetization of the sample.

Substituting (2.10) into (2.11) gives

$$\frac{d\mathbf{B}}{dt} = -\frac{m}{n_s e^2}\left(\nabla \times \frac{d\mathbf{J}_s}{dt}\right) \tag{2.14}$$

The Meissner effect shows that inside a superconductor the flux density is not only constant but the value of this constant is always zero; so d**B**/dt and **B** must die away rapidly below the surface. This restricts (2.14) to

$$\mathbf{B} = -\frac{m}{n_s e^2}\left(\nabla \times \mathbf{J}_s\right)$$

hence giving the second London Equation.

2.1.2.3 PENETRATION DEPTH

As a result of the Meissner effect electrical currents cannot pass through the bulk of the superconductor and instead flow along its surface. If a magnetic field is applied then the screening currents that flow so as to cancel the flux density inside also circulate on the surface. The currents (screening or otherwise) must occupy a thin surface layer otherwise their density would be infinite, a physical impossibility. Consequently, an applied flux density does not abruptly fall to zero at the boundary of the material but dies away within the region where the screening currents are flowing. The depth within which the currents flow is called the penetration depth (λ), because it is the depth to which the flux of the applied magnetic field appears to penetrate. The London brothers defined the penetration depth as

the distance inside a material when the flux density falls to 1/e of its value at the surface.

The Meissner effect of superconductors means that the material behaves like a perfect diamagnet. Therefore to derive this definition first consider that (2.13) can be simplified to $\mathbf{B} = \mu_r \mu_0 \mathbf{H}$. Where μ_r is the relative permeability of the material. Adopting the view point that all flux density is the result of the super-currents then $\mu_r = 1$ and $\mathbf{B} = \mu_0 \mathbf{H}$. Also taking the view that the super-currents affect $\mathbf{B}$ but they do not affect $\mathbf{H}$ then the Maxwell equation (2.12) can be rewritten as

$$\nabla \times \mathbf{B} = \mu_0 \left(\mathbf{J}_s + \frac{d\mathbf{D}}{dt} \right) \tag{2.15}$$

Unless the fields are varying very rapidly in time, the displacement current $d\mathbf{D}/dt$ is negligible in comparison with $\mathbf{J}_s$ so (2.15) can take the form

$$\nabla \times \mathbf{B} = \mu_0 \mathbf{J}_s \tag{2.16}$$

Then the second London equation (2.2) can be put into terms of just magnetic field by substituting (2.16) into it

$$\mathbf{B} = -\frac{m}{\mu_0 n_s e^2} \Big(\nabla \times \Big(\nabla \times \mathbf{B} \Big) \Big) \tag{2.17}$$

If $k = -m/(\mu_0 n_s e^2)$ then

$$\mathbf{B} = -k \Big(\nabla \times \Big(\nabla \times \mathbf{B} \Big) \Big) \tag{2.18}$$

A curl of a curl can be simplified to

$$\Big(\nabla \times \Big(\nabla \times \mathbf{B} \Big) \Big) = \nabla \times \Big(\nabla \cdot \mathbf{B} \Big) - \nabla^2 \mathbf{B} \tag{2.19}$$

According to Maxwell's equations $\nabla \cdot \mathbf{B} = 0$, so (2.19) becomes

$$\mathbf{B} = k \nabla^2 \mathbf{B} \tag{2.20}$$

which can be rearranged to

$$\frac{1}{k} \mathbf{B} = \nabla^2 \mathbf{B} \tag{2.21}$$

or

$$\nabla^2 \mathbf{B} = \frac{\mu_0 n_s e^2}{m} \mathbf{B} \tag{2.22}$$

This is a differential equation that **B** must satisfy. To see what (2.22) implies about the magnetic flux within a superconductor consider such a material when it is in a uniform magnetic field of flux density B_a applied parallel to the surface (see figure 2.3). The flux density outside the material is B_a, its maximum will be called the z-direction and the direction normal to the boundary will be called the x-direction.

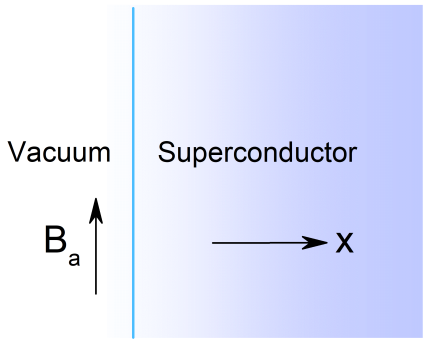

FIGURE 2.3 Magnetic field applied parallel to boundary of superconductor. Adapted with permission from page 34 of Ref. (19), Copyright Elsevier (1969).

Since the applied field is uniform, **B** will have the same direction everywhere therefore (2.22) can be regarded as a scalar equation; also there will be no gradients of the field parallel to the boundary, so (2.22) reduces to

$$\frac{\partial^2 B}{\partial x^2} = \frac{\mu_0 n_s e^2}{m} B \tag{2.23}$$

By inspection the solution to the above is [1]

$$B(x) = B_a \exp\left(\frac{-x}{\sqrt{m/\mu_0 n e^2}}\right) \tag{2.24}$$

Equation (2.24) shows that the flux density dies away exponentially insides a superconductor, falling to 1/e of its value at the surface at a distance x when $exp(-1)$. This distance is called the London penetration depth, λ_L. Therefore equation (2.24) can be re-written to

$$B(x) = B_a \exp\left(\frac{-x}{\lambda_L}\right) \tag{2.25}$$

[1] There is an alternative solution, $B_a \exp\left(\frac{x}{\sqrt{m/\mu_0 n e^2}}\right)$ but this is impractical as it approaches infinity as x increases.

where

$$\lambda_L = \sqrt{m/\mu_0 n_s e^2} \tag{2.26}$$

The London equations predict, therefore, a very rapid exponential decay of the flux density at the surface of a superconductor. See figure 2.4 for a graphical representation of (2.25).

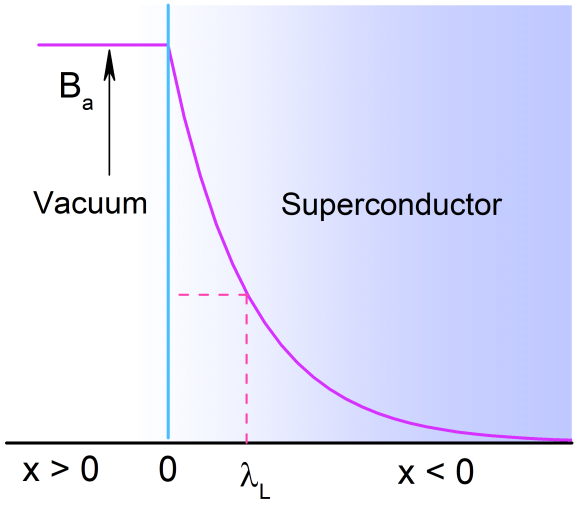

FIGURE 2.4 Variation of the flux density B(x) at the boundary of a superconductor. The magnetic flux density decays exponentially having crossed the boundary of the superconductor. λ_L is the London penetration depth, at this distance below the boundary of the superconductor the magnetic flux density will have decreased by 1/e from its surface boundary value B_a. Adapted with permission from page 36 of ref. (19), Copyright Elsevier (1969).

The London penetration depth predicted here when compared with experiment is smaller than the measured value by a factor of two or more. It is only an approximation and later theories would more accurately define this constant.

Finally, it was found that the penetration depth was not a fixed value but varies with temperature, page 29 of ref. (19). This is because the n_s of the superelectrons depends on temperature. For $T << T_C$ all of the free electrons are superconducting and since $\lambda_L \propto n_s^{-1/2}$ from (2.26) then λ_L is stable at a constant value. However as n_s falls steadily with increasing temperature, until it reaches zero at T_C, λ_L increases towards infinity, which corresponds to a uniform field in the material. Figure 2.5 shows this temperature dependence for tin, which is well

represented by the expression

$$\lambda_L(T) = \frac{\lambda_L(0)}{\sqrt{1-(T/T_c)^4}} \tag{2.27}$$

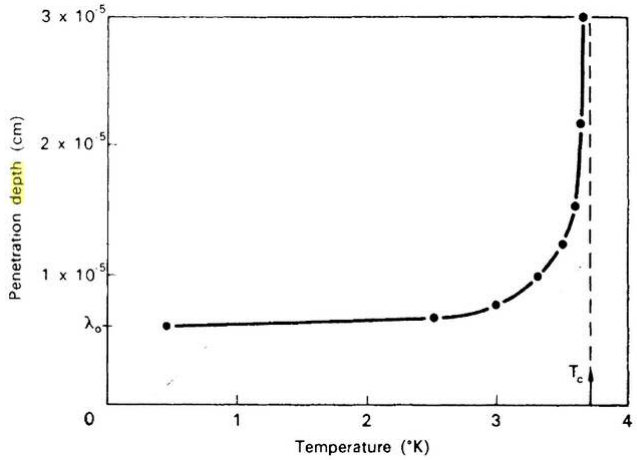

FIGURE 2.5 Variation with temperature of penetration depth in tin. Adapted with permission from page 29 of ref. (19), Copyright Elsevier (1969).

2.1.3 GINZBURG-LANDAU CONSTANT

The Ginzburg-Landau (GL) theory of superconductivity is a phenomenological model proposed in 1950 (25) and valid close to T_C. Recognition of this theory came after Gor'kov (26) showed that it could be derived from the microscopic BCS theory, which will be described in section 2.1.4.

The major assumption of the GL theory is that the behaviour of the superconducting electrons may be described by an "effective wave function" ψ, which has the significance that $|\psi|^2$ is equal to n_s. It is then assumed that the free energy F of the superconducting state differs from that of the normal state by an amount which can be written as a power series in $|\psi|^2$.

$$F = F_n + \Lambda\psi + \alpha|\psi|^2 + \gamma|\psi|^3 + \frac{\beta}{2}|\psi|^4 \tag{2.28}$$

In the equation (2.28), all the coefficients Λ, α etc. are functions of T, since the equilibrium values of F and ψ are functions of T. The second assumption of GL theory is that the coefficients can be expanded in powers of $T - T_C$. Therefore

(2.28) can be simplified to

$$\frac{\partial F}{\partial \psi} = 0 \tag{2.29}$$

In the normal phase, a minimum exists at $\psi = 0$, which implies $\Lambda = 0$ for $T > T_C$. Since it is assumed Λ can be expanded as a power series in $T - T_C$, this means $\Lambda = 0$ for all T and it was found that in most systems ψ^3 does not occur. Therefore

$$F = F_n + \alpha(T)\psi^2 + \frac{\beta}{2}(T)\psi^4 \tag{2.30}$$

Substituting (2.30) into (2.29) for the value, ψ_0, of ψ at the minimum gives

$$\alpha\psi_0 + \beta\psi_0^3 = 0 \tag{2.31}$$

with solutions $\psi_0 = 0$ and ${\psi_0}^2 = \alpha/\beta$. $\psi_0 = 0$ is the only solution for $T > T_C$, whereas for $T < T_C$ $\psi_0 \neq 0$. This is possible if the temperature dependence $-\alpha/\beta$ is negative for $T > T_C$, and positive for $T < T_C$. In addition, β must then be positive at all temperatures, since if β were negative F would decrease indefinitely for large values of ψ. Therefore α is positive for $T > T_C$, and negative for $T < T_C$. The simplest temperature dependencies that give this are

$$\begin{aligned} \alpha(T) &= A(T - T_C) \\ \beta(T) &= \beta(T_C) = \beta \end{aligned} \tag{2.32}$$

where A and β are positive constants. With α and β given by (2.32), the solutions for ψ_0 from equation (2.31) is

$$\begin{aligned} \psi_0 &= 0 \qquad && T > T_C \\ \psi_0 &= \pm A^{1/2}(T_C - T)^{1/2}/\beta^{1/2} \qquad && T < T_C \end{aligned} \tag{2.33}$$

The dependence of F on ψ which is shown in (2.30) is sketched in figure 2.6. For T well above T_C, F is simply a parabolic-shaped curve, with a well-defined minimum. As T approaches T_C, and $\alpha(T)$ decreases, the minimum becomes shallower. When T passes through T_C, and $\alpha(T)$ becomes negative, the minimum at $\psi = 0$ becomes a local maximum, and minima develop at $\psi = \pm\psi_0$. As T decreases further, the minima move out in ψ and slowly become deeper. F always increase for large enough ψ.

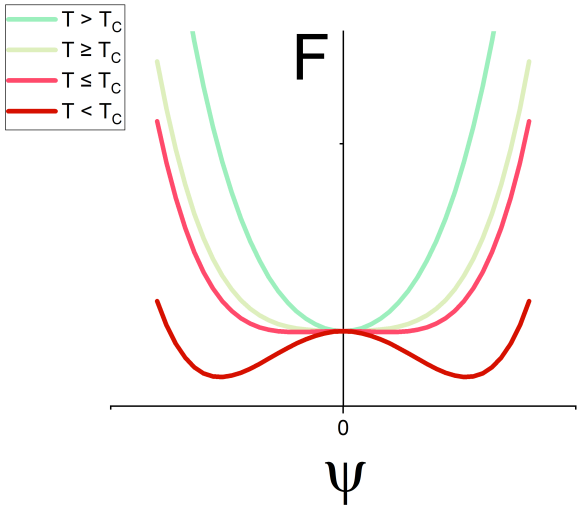

FIGURE 2.6 Variation of F with ψ at various temperatures.

(2.30) can be treated as the expression of the free energy density and from this relation it is possible to obtain the Gibbs free energy

$$G = f_n + \alpha|\psi|^2 + \frac{\beta}{2}|\psi|^4 + \frac{1}{2m}\left|(-i\hbar\nabla - 2e\mathbf{A})\,\psi\right|^2 + \frac{|\mathbf{B}|^2}{2\mu_0} - \mathbf{H}_0 \cdot \mathbf{B} + \frac{1}{2}\mu_0\mathbf{H}_0^2 \quad (2.34)$$

where f_n is the free energy in the normal phase, α and β in the initial argument were treated as phenomenological parameters, m is an effective mass, e is the charge of an electron, the magnetic vector potential $\mathbf{A}$ is defined as $\mathbf{B} = curl\mathbf{A}$ and $\mathbf{H}_0$ is the applied magnetic field. By minimizing the free energy with respect to variations in the order parameter and the vector potential, one arrives at the GL equations

$$\frac{1}{2m}\left(-i\hbar\nabla - 2e\mathbf{A}\right)^2\psi + \alpha\psi + \beta|\psi|^2\psi = 0 \quad (2.35)$$

(2.35) will give the variation of ψ within any specimen once the vector potential $\mathbf{A}$ is known. This has the boundary condition between a superconductor and an insulator

$$\mathbf{n} \cdot \frac{1}{2m}\left(-i\hbar\nabla - 2e\mathbf{A}\right) = 0 \quad (2.36)$$

$\mathbf{n}$ is the normal to the surface. (2.36) does not apply to metal/superconductor boundaries which requires consideration of proximity effects. The final GL equation for the dissipation-less electric current density $\mathbf{J}_e$ is given as

$$\mathbf{J}_e = -\frac{ie\hbar}{m}\left(\psi^*\nabla\psi - \psi\nabla\psi^*\right) - \frac{4e^2}{m}\psi^*\mathbf{A} \quad (2.37)$$

Further detail regarding this theory is beyond the scope of this thesis.

The GL equations predict a new characteristic length ξ in a superconductor called the coherence length. For $T > T_C$ (normal phase), it is given by

$$\xi = \sqrt{\frac{\hbar^2}{2m|\alpha|}} \tag{2.38}$$

while for $T < T_C$ (superconducting phase), where it is more relevant, it is given by

$$\xi = \sqrt{\frac{\hbar^2}{4m|\alpha|}} \tag{2.39}$$

This characteristic length is the distance which ψ can change without appreciable energy increase. The GL theory predicts the following penetration depth

$$\lambda = \sqrt{\frac{m}{4\mu_0 e^2 \psi_0^2}} \tag{2.40}$$

In the case of thin films, because of the boundary conditions, the variation of ψ_0^2 (i.e n_s) within the film depends on said film's thickness. The boundary conditions change for bulk materials and there is no significant variation between the London and GL penetration depth. GL theory uses λ and ξ to define the GL constant κ.

$$\kappa = \frac{\lambda}{\xi} \tag{2.41}$$

This ratio will become relevant in terms of surface energy which shall be discussed in section 2.2.1 of this chapter.

2.1.4 BARDEEN-COOPER-SCHRIEFFER THEORY

Bardeen-Cooper-Schrieffer (BCS) Theory is currently the most successful microscopic theory of superconductivity. It describes superconductivity as a microscopic effect caused by electrons forming Cooper pairs: which then behave as bosons and can condense coherently into a single quantum state. BCS set for themselves the task to formulate a theory that accounts for all the experimental observations namely: (a) the zero electrical resistance below T_C, (b) Meissner effect, (c) penetration depth and its temperature variation, (d) phase transition at T_C, (e) increase in the specific heat at T_C and an exponential in the electronic specific heat in the superconducting state, (f) an energy gap and (g) dependence of T_C on isotopic mass. The points (a) $-$ (c) have already been discussed. Those that have not will

be summarised in this section along with the BCS theory. Firstly this section will cover two concepts which pre-date BCS theory but were vital to its formation.

2.1.4.1 ELECTRON-PHONON INTERACTION

Electrons are fermions and therefore obey Fermi-Dirac statistics according to which no two electrons can occupy the same quantum state. They also experience Coulomb repulsion which prevents them from positively bonding. The first step towards the BCS theory was performed by Fröhlich (27) in 1950; who showed that two electrons can have an attractive interaction via a lattice distortion (phonon); which effectively couples them together. In the interaction one electron emits a phonon which is then immediately absorbed by another electron. The short time frame leads to an uncertainty in the phonon's energy, recalling the uncertainty principle $\Delta E \cdot \Delta t \geq \hbar/2$. Therefore the energy does not have to be conserved in the emission and absorption process; known as a virtual process. If the change in the first electrons energy after emitting a virtual phonon is less than the energy of said phonon then there will be an attraction between the two electrons. Figure 2.7 shows a schematic representation of electron-electron interaction transmitted by a phonon.

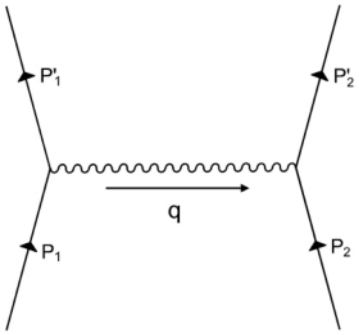

FIGURE 2.7 Schematic representation of electron-electron interaction transmitted by a phonon. p_1 is its momentum before scattering, p_1' its momentum after and q is the momentum of the phonon where $q = hv_q s$, v_q is the frequency of the phonon and s is the velocity of sound. Reprinted with permission from page 119 of Ref. (19), Copyright Elsevier (1969).

Fröhlich's suggestion that an electron-phonon interaction was responsible for superconductivity allowed him to independently predict the isotope effect, whose experimental discovery was also published the same year. The results of the experiments can be seen in figure 2.8, both experiments were performed on different

isotopes of mercury (28; 29). The isotope effect shows that for a given element's isotopes the relationship between its atomic mass and critical temperature is given by $M^{\alpha}T_C = constant$. For mercury it was found $\alpha = 0.5$ (28; 29). Further experiments then found $\alpha \leq 0.5$ (30) for all other known superconductors.

Figure 2.8 shows measured values of T_C for different isotopes of Mercury from the references (28; 29). T_C is plotted against $1/\sqrt{A}$ where A is the atomic mass of the sample. Through this relation a straight line can be fitted to the data. The T_C and atomic mass of mercury clearly following the relation $M^{0.5}T_C = constant$.

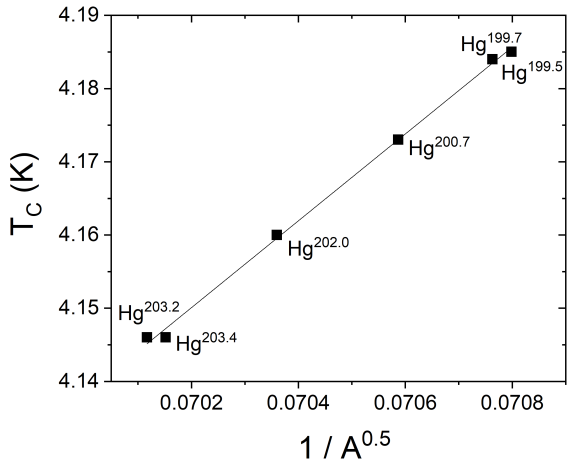

FIGURE 2.8 T_C of different isotopes of Mercury is plotted against $1/A^{0.5}$ where A is the atomic mass. Image adapted with permission from (29) DOI Copyright (1951) by the American Physical Society.

This result neatly explained why superconductors are bad normal conductors; a strong electron-phonon interaction at room temperature is required for superconductivity.

2.1.4.2 COOPER PAIRS

The next step towards a microscopic theory of superconductivity was taken by Cooper (31), who studied what happens when two electrons are added to a metal at absolute zero so that they are forced by the Pauli principle to occupy states where their momentum $\mathbf{p}$ is greater than the Fermi momentum p_F. If there is an interaction between these two electrons this will change the momentum of each electron, known at the time as 'scattering'. During a scattering event the electrons are subject to their mutual interaction and if this is an attractive one, the potential

energy which results from it is negative. Hence, over a period of time during which there are many scattering events, the energy of the two electrons is decreased by the time-average of this negative potential energy, and the amount of this decrease is proportional to the number of scattering events which take place.

Cooper then considered that if the interaction is the exchange of a virtual phonon the energy deficit between the initial and intermediate state is small $E_{1initial} - E_{1final} \simeq h\omega_q$, where ω_q is the frequency of the phonon. $E_{1initial}$ and E_{1final} must both be above the Fermi energy E_F so as to not violate Pauli's principle. The lowest values of $E_{1initial}$ and E_{1final} which still satisfy $E_{1initial} - E_{1final} \simeq h\omega_q$ lie within an energy $h\omega_L$ of E_F, where ω_L is an average phonon frequency typical of the lattice, about half the Debye frequency. Remembering that $E = p^2/2m$, this limitation on the allowed values of $E_{1initial}$ and E_{1final} means that $p_{1initial}$ and p_{1final} must lie within a range $\Delta_p = mh\omega_L/p_F$ of the Fermi momentum p_F. The total momentum of the interaction must also be conserved. Therefore the largest number of allowed scattering processes, yielding the maximum lowering of energy is obtained by pairing electrons with equal and opposite momenta. Further detailed quantum mechanical treatment of the problem revealed that the lowering of the energy is greatest if the two electrons also have opposite spin. This continued scattering that results in an energy state lower than $2E_F$ for the two electrons is called a Cooper pair. BCS theory uses a limiting case of the coherence length which it defines as the average 'size' of a Cooper pair when $T = 0$.

2.1.4.3 FORMATION OF THE MICROSCOPIC THEORY

Bardeen, Cooper and Schrieffer then created the BCS theory of superconductivity in 1957 by showing that Cooper's result could be extended to apply to many interacting electrons. The key assumption is that the only interactions which matter in the superconducting state are those between the electrons which make up a Cooper pair. The effect of any one pair on another is only to limit, through the Pauli principle, those states into which the interacting pair may be scattered, since some of the states are occupied.

The electrons of a Cooper pair are in a bound state which behaves as a composite particle. Since the individual electrons have opposite spins the composite particle has an integer spin and therefore obeys Bose-Einstein statistics. After formation the Cooper pairs are then able to condense into the same BCS ground state and an energy gap appears in the energy spectrum. An energy equal to this gap energy

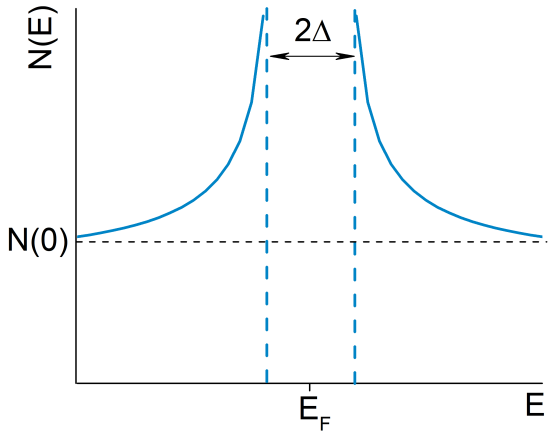

FIGURE 2.9 The BCS density of states.

is required to break a superconducting pair. Once a pair has been broken into quasi-electrons they will occupy the empty levels above the energy gap and Fermi energy (E_F). The density of states (number of states per an interval of energy at each energy level available to be occupied) for a superconductor is shown in figure 2.9, where $N(0)$ is a constant representing the normal density of states.

All the pairs in the ground state are indistinguishable and are in the same phase. The individual electrons are able to switch partners within a narrow energy band around the Fermi level. Momentum is conserved when a pair is formed $(k_1 + k_2) = (k_1' + k_2')$; where k_1 and k_2 are the wave functions of the electrons before exchanging a phonon and k_1' and k_2' are the post phonon exchange. According to this theory all pairs can be represented by a single wave function. This state is highly ordered and extends over the entire lattice and is responsible for most of the exotic properties of the superconductors.

A detailed analysis of the BCS theory is beyond the scope this thesis. The following sections will cover some examples for how BCS theory explains experimental observations.

2.1.4.4 SPECIFIC HEAT AND PHASE TRANSITIONS

At T_C the specific heat of superconductors is seen to change. For type II superconductors or type I's in the absence of a magnetic field at T_C there is a significant increase in their specific heat without any latent heat being released. An example of this measurement can be seen in Figure 2.10, which shows how the specific heat of niobium (Nb), a type II superconductor, varies with temperature.

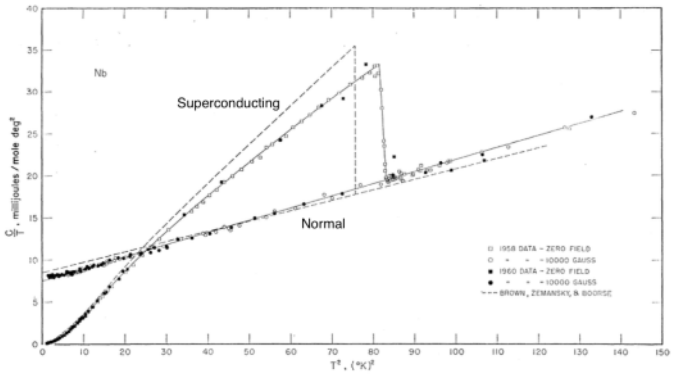

FIGURE 2.10 Specific heat of Nb. Normal state values are measured in a magnetic field greater than H_{C2}. Reprinted image with permission from (32) DOI Copyright (1962) by the American Physical Society.

This is a second-order phase transition, there is no latent heat measured and the change in specific heat at T_C is continuous. For type Is in the presence of a magnetic field a latent heat is measured (33). This latent heat arises because at temperatures between T_C and 0 K the entropy of the normal state is greater than that of the superconducting state, so heat must be supplied if the transition is to take place at a constant temperature. Further explanation for this difference is beyond the scope of this thesis.

There are two contributions to the specific heat: the lattice contribution and the electrons contribution. Through measurements of the properties of the lattice below T_C, such as its crystal structure and Debye temperature, it was found that its contribution did not change. Therefore it must be the electronic specific heat which is changing. This was experimental evidence that superconductivity is the result of the material's electrons undergoing a phase transition, in agreement with BCS theory. In the superconducting state, the electronic specific heat varies with temperature in an exponential manner

$$(C_{el})_s = ae^{-b/K_BT} \tag{2.42}$$

Where a and b are constants.

2.1.4.5 ENERGY GAP AND TRANSITION TEMPERATURE

The energy gap of a superconductor had been experimentally observed before BCS through infrared and microwave absorption (34; 35) and specific heat measurements (36), which were discussed in the previous section.

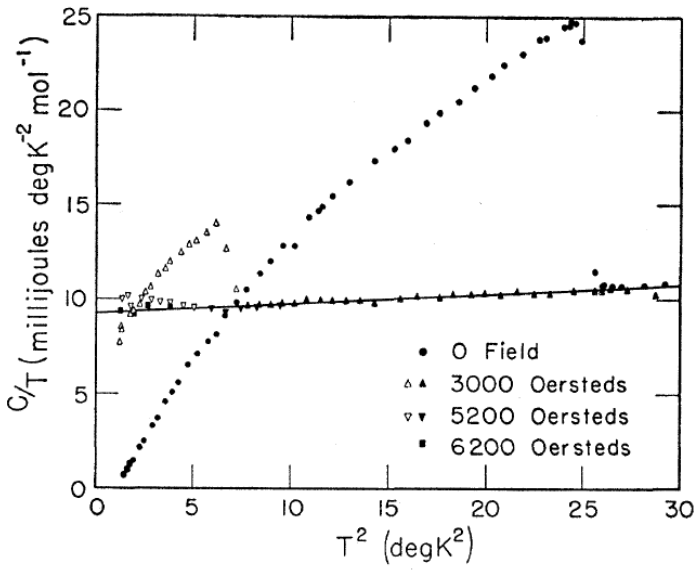

FIGURE 2.11 Shows C/T vs T^2 for normal and superconducting vanadium. The open symbols indicate incomplete quenching of superconductivity by the magnetic field. Clearly showing how there is an increase in the energy required to heat the same unit of mass by a given amount. Reprinted figure with permission from (36) DOI Copyright (1956) by the American Physical Society.

As has been already described BCS states this energy gap is the result of the electrons condensing into Cooper pairs; which then requires additional energy to break apart. BCS theory predicts the following relation between T_C and Δ

$$2\Delta = 3.5 k_B T_C \tag{2.43}$$

This relation however only applies when $T = 0$. As the temperature is raised above $T = 0$ pairs start being broken up by thermal agitation, and at any particular temperature the number of quasi-particles is given by the laws of statistical mechanics. An electron in a single state without a partner prevents that state from being occupied by a Cooper pair. The pair interaction energy is diminished because the number of scattering events in which they may participate is lessened. This decrease in the pair interaction energy leads to a decrease the energy gap. As the temperature rises, the number of quasi-particles increases and the energy gap continues to fall, until finally a temperature is reached at which the energy gap is zero. This is the critical temperature. Close to T_C, the energy gap versus temperature relationship is given by

$$2\Delta = 3.2 k_B T_C [1 - (T/T_C)]^{\frac{1}{2}} \tag{2.44}$$

The variation with T of the energy gap, as predicted by the BCS theory is given in figure 2.12. The shape of this curve has been well confirmed by experiment (37).

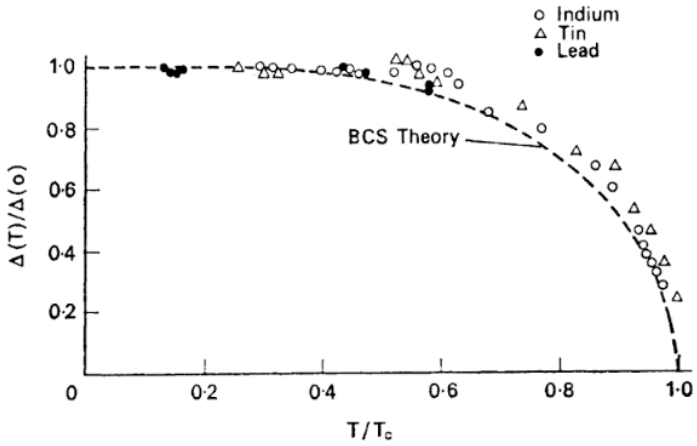

FIGURE 2.12 The energy gap of lead, tin, and indium versus temperature, as determined by tunnelling experiments. Reprinted from page 153 (37), DOI Copyright (1978), with permission from Elsevier.

2.1.4.6 ZERO RESISTANCE AND THE MEISSNER EFFECT

Relating the above to the first experiment for how superconductivity got its name, BCS theory explains zero resistance as a result of the Cooper pairs having a resultant moment which is the same for all pairs. A current carried by electrons or holes in a conventional conductor would scatter off of impurity atoms, lattice defects or thermal vibrations. In the case of a superconductor, the electrons which make up a Cooper pair are constantly scattering each other but their total momentum remains constant so there is no change in the current flow. The only scattering process which can reduce the current flow is one in which the total momentum of a pair in the direction of the current changes, and this can only happen if the pair is broken up.

A full explanation for the Meissner effect is a bit more complicated as it requires discussion of gauge symmetry which is beyond the scope of this thesis. BCS theory laid the groundwork for this latter theory.

2.1.5 DIRTY AND CLEAN SUPERCONDUCTORS

The notion of dirty superconductors was introduced by P.W. Anderson in 1959 (38). Anderson divided superconductors into two types regarding their

behavioural changes when physical and or chemical impurities are introduced. Clean superconductors critical temperature sharply reduces when these impurities are included, dirty superconductors on the other show little change in their transition temperature when additional impurities are added. The impurities introduce additional scattering which changes the mean free path (l) of the electrons when in the normal state. This is important when compared with ξ. Dirty superconductors are not sensitive to the introduction of additional impurities and defects to the material because $l << \xi$. Clean superconductors by contrast have the relation $l >> \xi$.

2.2 THE VORTEX STATE OF TYPE II SUPERCONDUCTORS

Type II superconductors were experimentally discovered in 1935 and it took until 1957, by Abrikosov (39), for the unusual transition to be explained as a vortex state. In this state the material is split into some mixture of superconducting and normal sections when $H_{C1} \leq H \leq H_{C2}$. BCS theory still holds true for the first type II superconductors discovered, pre-dating High T_C superconductors. Boron doped diamond shows type II superconducting in both poly (40; 41) and single crystal (6) films.

Abrikosov attributed the change in magnetic behaviour to a negative surface energy at the normal/superconducting boundary. This will be discussed further in section 2.2.1. The vortex state will be discussed in more detail in section 2.2.2. Section 2.2.3 discusses the change in type II superconductors magnetization which allows for the measurements of chapters 4 and 5. Section 2.2.4 describes the fundamental process of magnetic relaxation.

2.2.1 NEGATIVE SURFACE ENERGY

Surface energy is the excess energy at the surface of a material compared to the bulk. The surface energy of specific interest here is the total area of the boundary between the normal and superconducting phases. A situation which only arises for type II when $H_{C1} \leq H \leq H_{C2}$. In order to have a stable boundary between the two regions they must be in equilibrium i.e. their free energy per unit volume must be the same. Inside the superconducting region there are two contributions to the free energy. Firstly there is a positive 'magnetic' contribution to

the free energy which rises over the distance equal to λ. The result of the magnetization which the superconducting region acquires to cancel the flux density from the applied magnetic field. There is also a negative contribution to the free energy which is the result of the increase in order of the superconductors electrons. This ordering takes place over a distance ξ. Depending on which of these is greater determines whether the surface energy is negative or positive.

If the surface energy is positive, as is the case with type I superconductors, then the free energy of the system is minimized by having as small an area of interface boundary a possible, i.e. by having a few thick domains. Figure 2.13 shows the boundary when the surface energy is positive.

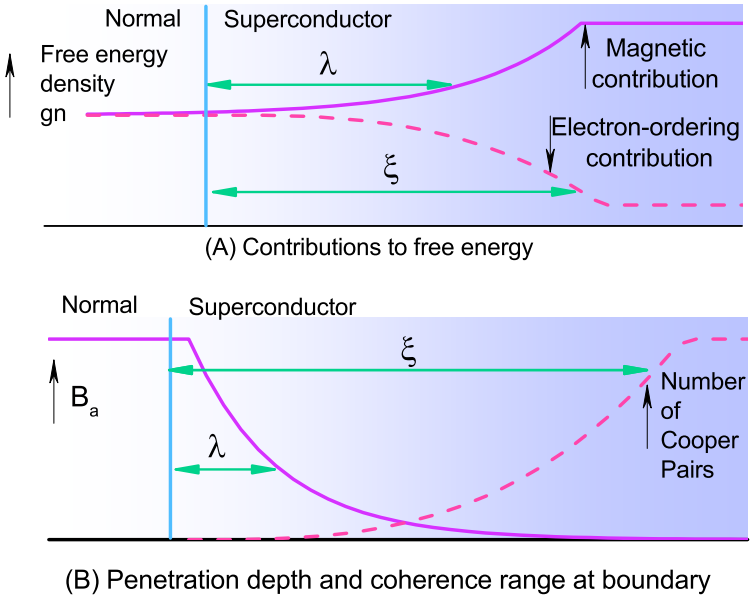

FIGURE 2.13 The interface at the superconducting and normal boundary has a positive surface energy for Type I superconductors. Adapted with permission from page 80 of ref. (19), Copyright Elsevier (1969).

Type II superconductors by comparison have a negative surface energy. If energy is released on forming the interface boundary, it is energetically favourable for the body to split up into a large number of thin domains so as to make the area of the interface boundary as large as possible. This is what leads to the aforementioned vortex state. Figure 2.14 shows the boundary when the surface energy is negative.

The GL parameter κ, introduced in section 2.1.3 as (2.41), is useful for determining whether a superconductor is type I or type II. The following relations

broadly hold true:

$$\kappa < 1/\sqrt{2} \qquad \text{Type I} \tag{2.45}$$

$$\kappa > 1/\sqrt{2} \qquad \text{Type II} \tag{2.46}$$

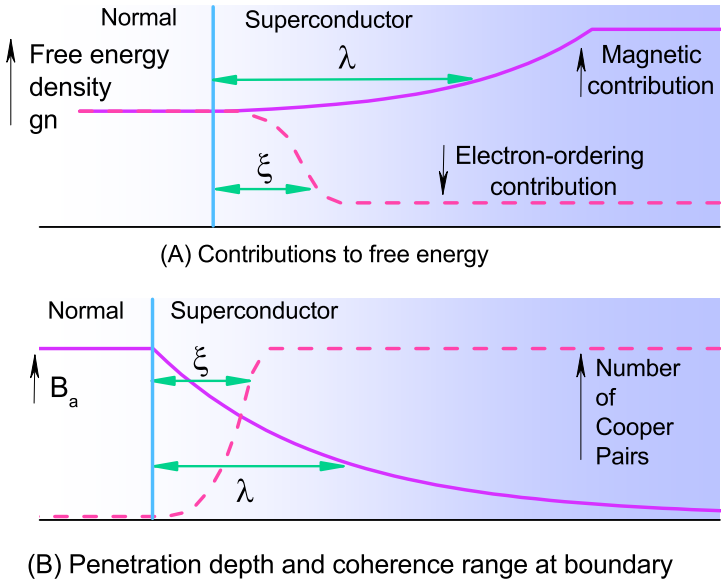

FIGURE 2.14 The interface at the superconducting and normal boundary has a negative surface energy for Type II superconductors. Adapted with permission from page 175 of ref. (19), Copyright Elsevier (1969).

2.2.2 VORTEX STATE AND FLUX QUANTA

The existence of a negative surface energy favours partial field penetration of the superconductor. The configuration of the normal regions threading the superconducting material is such that the ratio of surface area to volume of normal material is a maximum. The most favourable configuration is one in which the superconductor is threaded by cylinders of normal material, known as cores, lying parallel to the applied magnetic field strength. The cores radius will be very small, typically ξ, in order to increase the ratio of its surface area to volume. Each normal core has a magnetic flux density $\mathbf{B}$ which is generated by a vortex of persistent current that circulates around the core with a rotation opposite to that of the diamagnetic surface current. $\mathbf{B}$ will decay over a distance λ into the superconducting region. In this way there is no precise boundary but instead an inner core

which then diffuses as **B** drops off. Figure 2.15 shows an illustration of this internal structure.

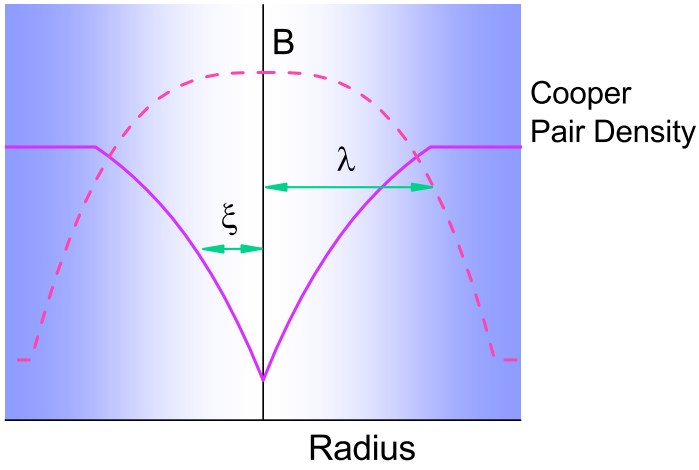

FIGURE 2.15 Illustration of the internal structure of an isolated vortex. Modified with permission from (42) DOI Copyright (1996) by the American Physical Society.

The total flux generated at each core by the encircling current vortex was predicted by Abrikosov to be one magnetic flux quantum ϕ_0, which is defined as

$$\phi_0 = \frac{h}{2e} = 2.068 \times 10^{-15} \text{ Wb} \tag{2.47}$$

The structure described above consisting of the core, vortex and magnetic flux density together shall be referred to simply as the vortex or vortices from this point on wards. The vortices during the vortex state of a perfect (no defects) ellipsoidally shaped isotropic superconductor, form into a meta stable hexagonal lattice. This is due to the fact the vortices repel each other. As the field strength increases the density of the vortices increases at the expense of the superconducting volume fraction and at H_{C2} the entire structure collapses. The material turns normal. BNCD films are not an ideal material and alter this simple idea this will be discussed more in section 2.2.3.1.

The ξ defined by GL theory is related to ϕ_0 and H_{C2} when $T = 0$ through the following equation:

$$\xi^2 = \frac{\phi_0}{2\pi H_{C2}}(T = 0) \tag{2.48}$$

2.2.3 MAGNETIZATION

The experiments of chapters 4 and 5 involve the measuring of the BNCD samples magnetization. Magnetization (M) of a material expresses the density of permanent or induced magnetic dipole moments. The expression of this that is used for this thesis is as follows

$$M = \frac{dm}{dV} \tag{2.49}$$

Where dm is the elementary magnetic moment and dV is the volume of the sample in question. The magnetization of a type II superconductor behaves likes type I below H_{C1} so exhibits perfect diamagnetism. For chapter 4 experiments the fields applied are considerable below the BNCD samples possible H_{C1}. Figure 2.16 (A) gives an example of a type I superconductors magnetic behaviour versus temperature. Figure 2.16 (B) shows the magnetization versus the change in field.

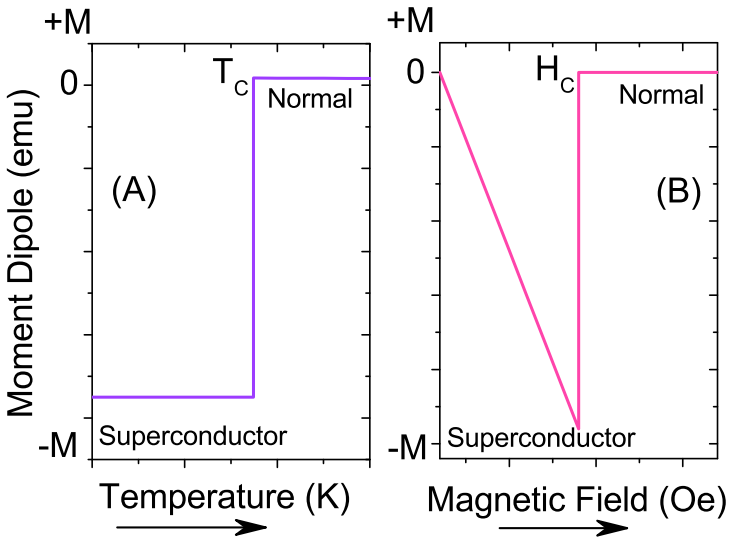

FIGURE 2.16 (A) is an example of a type I superconductors magnetic behaviour versus temperature. (B) shows the magnetization versus the change in field.

2.2.3.1 IRREVERSIBILITY

Type II superconductors have a more complex magnetization than that shown in figure 2.16 (B) as a result of the mixed state. An example of which can be seen in figure 2.17 (A). This image is then further changed for non-ideal samples i.e. those that contain impurities or crystalline faults. BNCD films are granular which means they have grain boundaries and defects: both of which pin the vortices

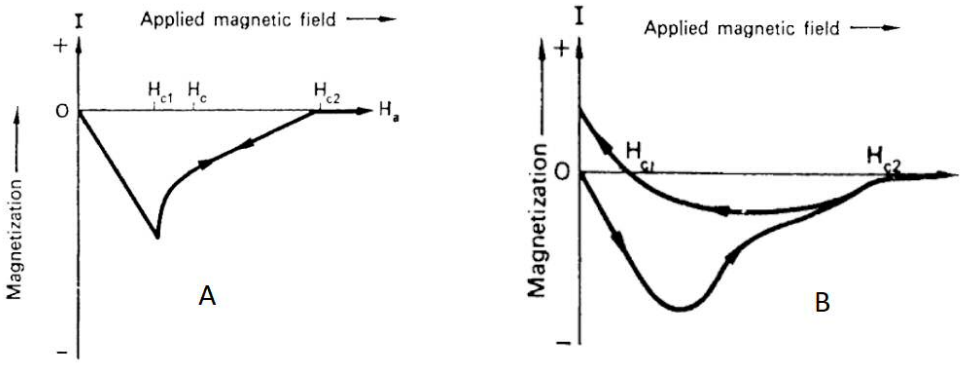

FIGURE 2.17 A shows the magnetization of a type II superconductor. B shows irreversible type II magnetization curves. Adjustment of images with permission from pages 186 and 188 of (37) DOI Copyright (1978) by the American Physical Society.

causing the magnetization to show irreversibility. Consequently, on increasing the applied field strength from zero there is no sudden entry of flux at H_{C1} because the cores formed at the surface are hindered from moving into the interior. Similarly, on reducing the applied field strength from a value greater than H_{C2}, there is hysteresis, and flux may be left permanently trapped in the sample as a result of the pinning sites. The amount of pinning sites can be altered in the production of the type II superconductors. It is possible to have type II materials free of such defects. The only way to effectively reverse this behaviour is to warm the superconductor up and 'restart' the system. An example of irreversible magnetization can be seen in figure 2.17 (B).

2.2.4 BEAN'S CRITICAL STATE MODEL

The first phenomenological model of type II's magnetization was given by Beans (43; 44). Bean assumed a 'filamentary mesh structure' for the sake of simplified calculations. Figure 2.18 shows an example of this structure. The filaments have a diameter less than λ_L and sustain a super-current up to a critical field current density J_C, which is a function of magnetic field. Bean's calculations only considered a case where J_C is independent of the magnetic field which is equivalent to $H_{applied} << H_{C2}$. A situation which can be applied to the experiment described in chapter 4.

The mesh interstices consist of a 'soft' superconductor of critical field H_{C1} which shields the material until H_{C1}; beyond this field the shielding is provided by magnetising currents induced in the filaments at a critic value J_C in a depth

necessary to the reduce the field. Bean introduced a field dependent penetration depth Δ_{Bean} which is defined as

$$\Delta_{Bean} = \frac{10H}{4\pi J_c} \tag{2.50}$$

Whilst this filament model does not accurately explain the vortex state in terms of cores it does give accurate predictions of the magnetization of the type II superconductors. The key result from the Bean's critical state model required for the calculation of critical current in chapter 4 is that (a) each type II superconductor is characterized by a limiting critical current density $J_c(B)$ and (b) that even the smallest electromotive force induces this full current that flows locally. The critical current density is a maximum that applies to both a current passed along the sample from a external source and to screening currents passed along its surface. As there is a critical field so to is there a critical current, equation (2.2).

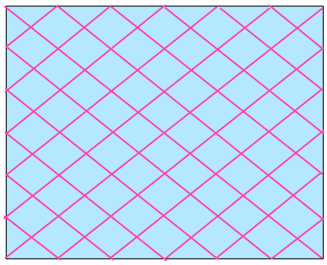

FIGURE 2.18 Example of filamentary mesh structure. The filaments (pink) have a diameter less than the London penetration depth. The space between the filaments (blue) consists of a 'soft' superconductor of critical field H_{C1}.

2.2.5 VORTEX CREEP

Another effect of the pining centres is to disturb the simple hexagonal arrangement of the ideal Abrikosov vortex lattice. This was recognised by Larkin and Ovchinnikov (45), who predicted that the lattice would break up into domains with a size corresponding to a finite correlation length for hexagonal order perpendicular to the vortex axis. The higher the pinning strength compared to the vortex interaction energy, the smaller the correlation length. This concept was extended to consider correlation lengths both parallel to the vortex axis and perpendicular to it. The vortices pinned in this way are in a meta-stable state.

In the absence of pinning, the vortex array can always reach its thermodynamic equilibrium state. The magnetic moment or magnetization in this case is reversible, so does not depend on the magnetic field or temperature history of the sample. The meta-stable state that arises in the presence of pinning can also be a thermodynamic equilibrium state. However, there is also the possibility of non-equilibrium or non-uniform spatial distribution of vortices, which are are stabilized temporarily by the pinning of vortices.

The relaxation of this non-equilibrium state back towards thermodynamic equilibrium is the basic phenomenon underlying the experimentally observed magnetic relaxation. Magnetic relaxation is defined as the spontaneous motion of the vortices out of the pinning sites, such motion usually arises from thermal excitation or quantum tunnelling. A model explaining this effect was first described by Anderson and Kim (46; 47; 48). They introduced the basic concept of thermal activation of magnetic flux lines, see chapter 5, out of pinning sites, which proceeds at a rate proportional to $\exp(2U/K_BT)$, where U represents an activation energy (or pinning potential of the superconductor), k_B is Boltzmann's constant, and T is the absolute temperature. This process leads to a redistribution of the vortices, which redistributes the current loops associated with them, thus causing a change in the magnetic moment with time. The Anderson-Kim model predicted a magnetic moment changing logarithmically with time, as has been observed in experiment (48) which became known as 'magnetic flux creep'. This will be discussed in chapter 5.

CHAPTER 3
DIAMOND GROWTH AND PROPERTIES

This chapter contains a short introduction to the most common methods of diamond growth, specifically high pressure high temperature (HPHT), detonation synthesis and chemical vapour deposition (CVD). The process for making diamond superconducting is also summarised. A discussion of the current understanding of diamond's superconductivity is also presented. The diamond samples for this thesis were grown using the product of detonation synthesis as seeds in a CVD growth process. The specific growth processes for the films, their physical properties and which chapters they are used for are highlighted therein.

3.1 DIAMOND GROWTH

The diamond industry is predominantly interested in the diamond's exceptional hardness and high thermal conductivity at room temperature. This led to a widespread use of diamond in cutting and polishing tools and the scientific applications in diamond knives and diamond anvil cells. After the 1797 discovery that diamond was pure carbon (49), many attempts were made to convert various cheap forms of carbon (typically graphite) into diamond. Figure 3.1 shows the contrast between the crystal structures of graphite and diamond, which is the reason for the differences between their properties. Diamond's carbon atoms are arranged in a tetrahedral sp^3 lattice, whereas graphite's carbon is sp^2 bonded into hexagonal planar structures which are held together by van der Waals forces.

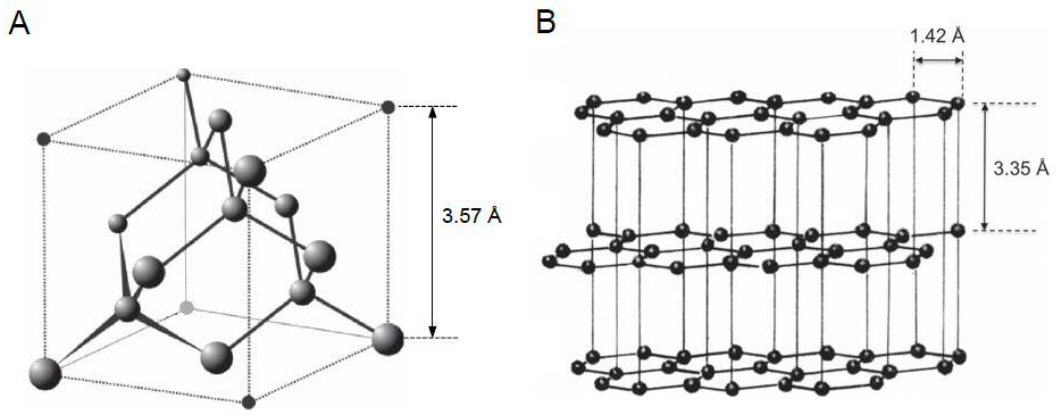

FIGURE 3.1 (A) Shows the diamond lattice and its tetrahedral sp^3 bonding configuration. (B) Shows an example of the graphite lattice, with its hexagonal planar structures provided by sp^2 bonds and held weakly together by van der Waals forces. Taken from (50).

Carbon is stable in graphite form at room temperatures and atmospheric pressures, converting this to diamond requires significantly higher temperatures and pressure. Figure 3.2 shows a phase diagram of carbon highlighting the regions in which diamond and graphite are the thermodynamically favoured allotropes of carbon. The Berman-Simon line (B-S line) (51) represents equilibrium phase boundaries: above the line diamond is the stable carbon allotrope, while graphite is stable below the line.

The intense pressures and temperatures required to replicate the production of natural diamonds are infeasible for the commercial production of diamond, resulting in the development of alternative methods. The two most common processes used to create nm^3 to mm^3 sized diamonds are the high pressure high temperature (HPHT) technique and the chemical vapour deposition (CVD) technique. Diamonds grown via these methods can either be one single continuous crystal or be made up of many smaller crystals (polycrystal). Polycrystalline diamond (PCD) consists of numerous small grains and is often described by its average grain size. Grain sizes vary from nanometers, such as those grown for this thesis called nanocrystalline diamond (NCD), to micrometers. The third most common diamond growth process is called detonation synthesis and only produces nanodiamond particles.

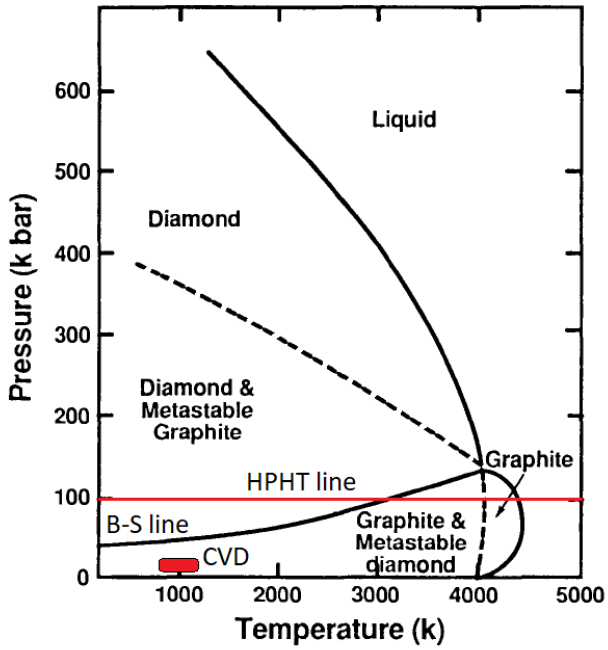

FIGURE 3.2 Carbon phase diagram detailing regions in which graphite and diamond are the thermodynamically favoured allotropes, separated by the B-S line. The horizontal red line marks the conditions above which diamond production takes place for catalyst-assisted HPHT. CVD circumvents thermodynamics and grows diamond kinetically at less than atmospheric pressures, this region is marked by a red rectangle on the graph. Detonation diamond is grown during the initial shock wave, where the pressure and temperature reach the stability region of diamond in the above diagram. Adapted from (52), Copyright (1993), with permission from Elsevier.

3.1.1 HPHT

This process was the first to demonstrate man made diamond growth in the 1950s (53). Typical HPHT uses a graphitic carbon source, seed diamond, and catalytic solvent which are compressed at reduced pressures and temperatures of the order of 5 GPa (50 kbar) and 1500 K respectively to produce diamond at a rate of mg h^{-1} (54). The use of a diamond seed and catalytic solvent, typically a transition metal such as Fe, Co, Cr, Ni, Pt, Pd or mix thereof, hastens the rate of diamond formation. During compression the catalytic solvent acts to break apart the C-C bonds within the graphitic carbon to saturate the molten metal at pressures and temperatures conducive to the formation of diamond, resulting in the transport of carbon and growth of the diamond seed.

The products of HPHT are predominantly used for industrial applications (55), due to the process being suitable for the mass-production of high-quality diamond crystals. However, HPHT is not capable of much flexibility in diamond growth and nitrogen impurities are common (55).

3.1.2 DETONATION DIAMOND

Ideal diamond growth conditions can be produced via an explosive charge and was first demonstrated in 1963 (56). In this process no carbon source is needed, although one can be used, as the explosion itself delivers the carbon. In an oxygen-deficient environment the incomplete combustion of organic explosives, such as CHNO (57), and $C_3H_6N_6O_6$ (known commercially as Research Department Explosive or RDX) leads to the formation of elemental carbon, in addition to the combustion products CO_2, CO, water and nitrogen (58; 59). There have been many experiments carried out to find the optimal mixture of explosives for a maximum production of diamond. The ideal is a 3:2 mixture of highly under-oxygenated TNT, the source of the carbon, and RDX is used to reach the conditions necessary for diamond formation (57; 58).

The diamonds produced under these conditions are rounded nano-diamond particles of 5 nm diameter with a narrow size distribution due to the microsecond formation time (57; 58; 56; 60). They are often referred to as detonation nanodiamond (DND) (56). As the pressure begins to rapidly drop the sustained high temperature leads to formation of graphitic onion like shells around the nano-diamond as a result of phase conversion, with graphitic structures binding the particles together to form core aggregates of $100 - 200$ nm in size (57; 60). An example of which can be seen in figure 3.3.

In order to accelerate cooling and minimise the formation and or conversion to graphitic structures the detonation takes places in an inert gas or water (61). These core aggregates are then in turn weakly bound through electrostatic attraction to create large aggregates ranging in size from hundreds of nm to μm (58). As a result, nano-diamond forms up to 75% of the resulting soot along with $25 - 85\%$ graphitic carbon and $1 - 8\%$ incombustible material (61).

The DND aggregates are then retrieved via a series of purification processes. First the soot from the detonation is filtered with sieves and magnets to remove large foreign debris arising from the chamber walls, metal from the detonator, and polyethylene should a water container surrounding the charge be used (57; 58). The remaining material is then acid treated to remove any remaining metallic contamination and oxidise the non-diamond carbon in the soot (57; 58).

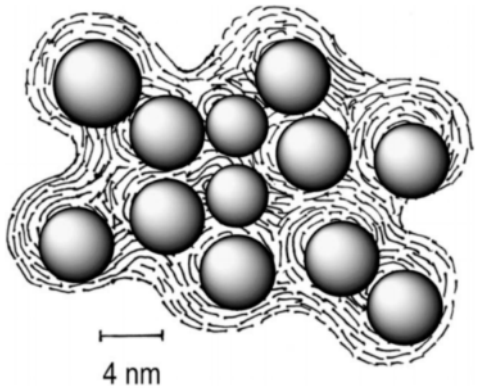

FIGURE 3.3 Nano-diamond particles surrounded by onion like shells and graphitic carbon. The result of cooling after the initial explosion. Taken from (50).

For this thesis stable mono-dispersed hydrogen terminated H_2O colloids were used as a seeding step in the CVD growth process for the nanocrystalline diamond films. This solution is created from the DND aggregates powder, after the purification steps, via hydrogen annealing, ultrasonic dispersion and centrifuging. The resulting colloids are then suitable for the aforementioned seeding step (4), this will be described further in the CVD section.

3.1.3 CHEMICAL VAPOUR DEPOSITION

Diamond growth by chemical vapour deposition (CVD) was first pioneered in the early 1950's by Eversole and independently by groups within the United States and the former Soviet Union (62). CVD is a chemical process where a substrate is exposed to one or more volatile gases, which react and/or decompose on to the substrate surface to produce the desired deposit. Eversole observed the growth of natural diamond samples when they were heated to 960 °C at less than atmospheric pressure in a CO environment. Subsequent experiments with ^{13}C enriched CO_2 showed an increase in the abundance of ^{13}C within the diamonds, conclusively demonstrating the metastable growth of diamond (55). Improvements were made to this process with the addition of atomic hydrogen which preferentially etches the co-deposited graphitic component (62) and developments in reactor design. Through this technique diamond is grown kinetically rather than thermodynamically with the associated high pressures and temperatures. Diamond growth via CVD requires simpler equipment and cheaper running costs than HPHT, it also provides very fine control of the diamond growth (due to the fine control of the conditions e.g. gas flow) and minimises impurities (55; 62).

The CVD technique grows diamond films by feeding the carbon carrying precursor gases into a vacuum containing the substrate for growth. The gases are then activated (ionised) in order to create a plasma and start off the deposition of the carbon. Activation method can involve thermal process (e.g. a hot filament), electric discharge (e.g. DC, RF or microwave), or a combustion flame (such as an oxyacetylene torch) (55). The films for this thesis were grown using a Seki AX6500 series microwave plasma reactor supplied by Seki Technotron, now Cornes Technologies Limited, Japan.

The activation methods differ in detail but all involve the same basic components. The carbon carrying precursor gas, typically methane (CH_4), is diluted in an excess of hydrogen ($\approx$ 1% CH_4) (55). During the growth process as the gas is activated the molecular hydrogen decomposes and is able to separate methane to form the methyl radical (CH_3), demonstrated through in situ spectrometry to be the dominant species for diamond growth (63). This leads to a plasma containing a mixture of hydrogen, methane and hydrogen and methyl radicals at temperatures approaching a few thousand kelvin. Beyond the activation zone, these reactive fragments continue to mix and undergo a complex set of chemical reactions until they strike the substrate surface, typically held at temperatures exceeding 700°C, before either reacting or diffusing across or through the surface. At the surface the species either adsorb and react with the surface, adsorb again back into the gas phase, or diffuse around close to the surface until an appropriate reaction site is found. If a surface reaction occurs, one possible outcome, if all the conditions are suitable, is diamond (55).

3.1.3.1 NUCLEATION

Growth of diamond begins when individual carbon atoms nucleate onto the surface in such a way as to initiate the beginnings of an sp^3 tetrahedral lattice. If a diamond substrate is being used then this provides the template for the diamond lattice which is then just extended atom-by-atom as the deposition proceeds, this is called homoepitaxial growth. Successful and efficient growth on the majority of foreign substrates requires a nucleation enhancement step. This is because a non-diamond substrate does not provide a template for the C atoms to follow, so those C atoms deposited will often immediately be etched back into the gas phase by reaction with atomic H. This means that the initial induction period before which diamond starts to grow can be prohibitively long (hours or even days). One such method to provide a template, and decrease the initial induction period, involves

seeding the substrates with detonation nanodiamond (DND) particles (64). A process which is used for the NCD films grown in this thesis.

3.1.3.2 GROWTH

Once diamond has begun growing the structure is continued by the addition of the methyl radicals resulting in an atom by atom growth of diamond (62). The radical hydrogen atoms are vital for the production of high quality diamond as they aid in the fracturing of CH_4, keep the sp^3 formations of the surface intact therefore preventing reconstruction to the thermodynamically favoured allotrope graphite, and preferentially etching away sp^2 sites at a rate exceeding that of their growth (55). Figure 3.4 gives shows an example of this process. This is a very simplified description of the picture and further reviews of the behaviour of the gases and growth is beyond the scope of this thesis but can be found in (62; 55).

The initial diamond template for the films grown for this thesis came from DND particles. These initial DND particles grow via a Volmer-Weber model (65), i.e. the DND particles grow longitudinally and laterally in the plane on the surface of the substrate until they coalesce to form a film. This film will be comprised of diamond grains of varying sizes and facet orientations, a polycrystalline structure. CVD growth for each grain from this point onwards will be predominantly normal to the surface. The diamond grains growth rate will depend upon its facet orientation in accordance with the Van der Drift growth model (66). As has already been stated there is a variation in facet orientation between each individual diamond grain. As a result there is a variation in growth rate between the different grains. This leads to competitive growth between the individual grains and results in an uneven final film layer, or surface roughness, which evolves with film thickness. Chapter 6 deals with attempts to optimise the chemical mechanical polishing (CMP) of this surface roughness and the motivations for doing so.

Additionally whilst this roughness increases with film thickness the increase in crystal size leads to a decrease in grain boundaries and defects. This means that the outer layers of thicker films are often of much better quality than the initial nucleating layers. This factor is relevant for the films grown for this work of varying thicknesses. As a change in crystal size and grain boundaries will be seen to influence the superconductivity.

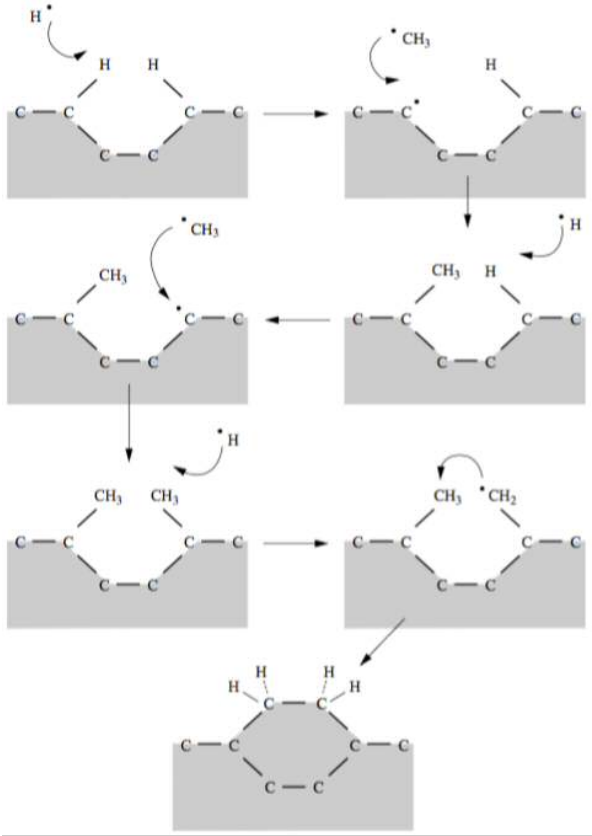

FIGURE 3.4 Model of CVD diamond growth. Activated atomic hydrogen removes the sp^3 stabilising hydrogen atoms bonded to the diamond surface, forming the diatomic H_2 and leaving a reactive surface site. While typically terminated by another hydrogen atom a methyl radical can alternatively react with the site, adding a lone carbon atom to the surface. Further H abstraction and methyl deposition can then occur until the carbon atoms are locked within the tetrahedral lattice, growing the diamond surface atom by atom. Republished with permission of Royal Society, from (55); permission conveyed through Copyright Clearance Center, Inc.

Crystal sizes are also dependent upon methane concentrations, the crystals decrease as methane increases. Above 3% CH_4 in H_2 the crystalline morphology is reduced to the scale of nano crystals (4). This is the method employed for the films used in this work. This type of film can be considered to be an aggregate of diamond nano crystals and disordered graphite. The NCD film however still possesses many of the desirable properties of diamond while being much smoother, the surface roughness is kept to nano meter scales although this is still a problem for device product which will also be discussed in chapter 6, and considerably faster to deposit (5). Decreasing the methane concentration would have the reverse effect. Thus by simple variation in methane conditions diamond films can be deposited with properties ranging from almost graphic to essentially those of natural diamond.

3.2 SUPERCONDUCTING DIAMOND

3.2.1 SUPERCONDUCTING SEMICONDUCTORS

The possibility of a degenerate semiconductor, a semiconductor with such a high level of doping that the material starts to act more like a metal, or a semimetal, a material with a very small overlap between the bottom of the conduction band and the top of the valence band, having a superconducting state was theoretically explored in the late 1950's and early 1960's (67; 68; 69). In particular, n-type doping was investigated and it was stressed that superconductivity should be favored in doped semiconductors having a many-valley band structure, because of the additional attractive interactions provided by inter-valley phonons (68). Experimentally type II superconducting transitions were observed in doped GeTe (70), SnTe (7) and SrTiO3 (71) between 50 mK and 500 mK. In all three cases, $H_C(T_C)$ phase diagrams were obtained while specific heat measurements established the bulk character of the transition. The doping dependence of T_C of the two p-type tellurides was also investigated. The slower increase of T_C at higher carrier concentrations was attributed to an increased screening of the phonon-mediated coupling. The same argument was put forward to explain the maximum T_C observed (71) in n-type SrTiO3 for a carrier concentration on the order of $10^{20} cm^{-3}$. The energy gap of GeTe was measured using tunnel spectroscopy studies (70). The energy gap was shown to have the relation $2\Delta = 4.3 k_B T_C$. These results were considered at the time to further validate the BCS model for superconductivity (69). Despite these initial successes, 'superconducting semiconductors' was not of much interest until the result of Eskimov *et al.*(6) was published, which renewed interest and lead to discoveries such as the superconductivity of heavily boron doped silicon (72).

3.2.2 INCORPORATION OF BORON INTO DIAMOND

The superconductivity of boron doped diamond was first discovered by Eskimov *et al.*(6) in a polycrystalline sample synthesized using HPHT; shortly after this superconductivity was also found in CVD grown polycrystalline films (40; 41) and single crystal films (73; 74).

Boron has one less electron than carbon and, because of its small atomic radius, is relatively easily incorporated into diamond. As boron acts a charger acceptor the resulting diamond is effectively hole (p type) doped. In CVD diamond

growth boron is introduced using boric gases such as diboran (B_2H_6) or trimethylboron (TMB) (75). The later method was used for growing the BNCD films for this thesis. Changing the mixture ratio of methane and TMB is used to control the concentration of boron in the diamond samples. The exact boron concentration in the diamond films depends upon the preparation conditions (7). The metal-insulator transition line for diamond has been found to lie between 2×10^{20} and 5×10^{20} cm^{-3} (76; 7), with superconductivity appearing above about 6×10^{20} cm^{-3} (7).

The T_C of the superconducting diamond has been shown to be strongly dependent on boron concentration (7). The greater the concentration of boron, the greater the T_C, figure 3.5 shows an example of this relation. The T_C values were calculated from resistivity curves and the boron concentration from secondary-ion mass spectrometry (SIMS). SIMS measures the composition of solid surfaces and thin films by sputtering the surface of the specimen with a focused primary ion beam and collecting and analysing the ejected secondary ions. The mass/charge ratios of these secondary ions are measured with a mass spectrometer to determine its elemental, isotopic, or molecular composition.

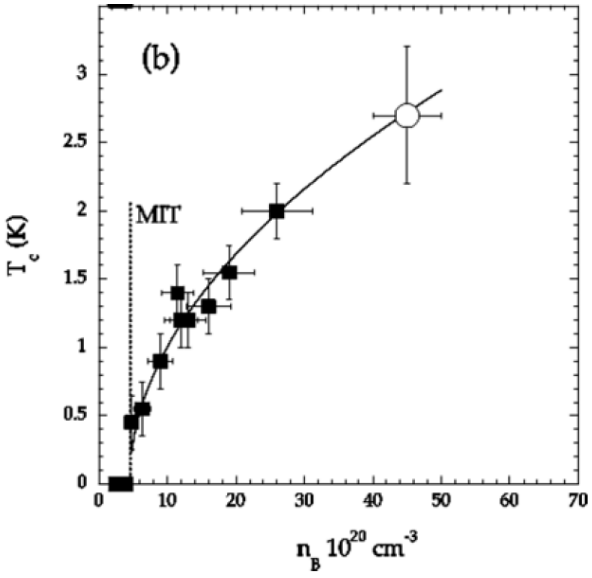

FIGURE 3.5 Critical temperature T_C deduced from resistivity curves (at 90% of the normal state resistance) as a function of the boron content n_B deduced from SIMS measurements. The open circle was taken from ref. (6) and full image reprinted from (7), Copyright (2008), with permission from Elsevier.

The exact values of T_C depend upon the preparation method and conditions along with the exact experimental characterization and data analysis procedures

applied to the transition. With this in mind, the films grown for this thesis of varying film thickness ought to show an increase in T_C with increasing film thickness. The methods were identical and the crystals and films left to grow larger for each case.

3.2.3 DIRTY TYPE II SUPERCONDUCTIVITY

The first experimental studies that published H_C vs. T_C phase diagrams shows diamond to be a type II superconductor (6; 40). Figure 3.6 shows the temperature dependence of H_{C2} for the sample measured in Eskimov *et al.* (6). They use the resistive mid-point to define H_{C2}. The results show a wide transition width $\approx$ 2 K, which suggested the presence of a vortex state.

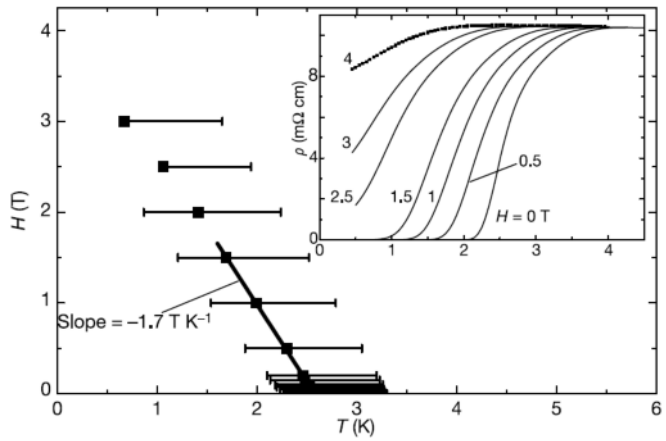

FIGURE 3.6 Temperature dependence of the upper critical field for polycrystalline boron doped diamond. The resistive mid-point is used to define H_{C2}. The inset shows the evolution of the resistivity near T_C at different magnetic fields 0-4 T. Reprinted by permission from Springer Nature, Nature (6) DOI, Copyright (2004).

Eskimov *et al.* calculated that their diamond sample had $\xi_{GL} = 10$ nm. Ref. (77) found the ξ_{GL} for their CVD grown polycrystalline films was 10 nm to 30 nm. Ref. (74) found their single crystal films to have ξ of 15 nm and 20 nm. All these values were calculated using equation (2.48).

Ref. (77) estimated a mean free path l for the holes in the normal state; which were determined through a a combination of Hall effect and conductivity measurements at 4.2 K. l was on the order of 0.5 nm in samples where $\xi = 10$ nm. These authors then evaluated a London penetration length λ_L of 150 nm (using the

equation (2.26)) for the same film. As $l << \xi << \lambda_L$ they concluded that boron-doped diamond was a dirty superconductor. A reminder from section 2.1.5 dirty superconductors are not sensitive to the introduction of additional impurities and defects to the material because $l << \xi$. Clean superconductors by contrast have the relation $l >> \xi$.

Further confirmation of type II superconductivity for single crystals came in the form of vortex images obtained by ultra-low temperature scanning tunnel microscopy (23). Scanning tunnel microscopy (STM) is based on the concept of quantum tunneling. When a conducting tip is brought very near to the surface to be examined, a bias (voltage difference) applied between the two can allow electrons to tunnel through the vacuum between them. The resulting tunneling current is a function of tip position, applied voltage, and the local density of states of the sample. Once tunneling is established, the tip's bias and position with respect to the sample can be varied (with the details of this variation depending on the experiment) and data are obtained from the resulting changes in current.

If the tip is moved across the sample in the x-y plane, the changes in surface height and density of states causes changes in current. These changes are mapped in images. This change in current with respect to position can be measured itself, or the height, z, of the tip corresponding to a constant current can be measured. The single crystal sample STM measurements were performed in a dilution refrigerator down to a base temperature of 50 mK. The images can be seen in figure 3.7.

Ref. (23) from H_{C2} measurements and use of the relation (2.48) found that $\xi = 15nm$. Through optical and electrical transport measurements they estimated a mean free path for the carriers of $l = 1.5$ nm.

3.2.4 BCS-LIKE SUPERCONDUCTIVITY

Since its discovery there was discussion regarding whether superconducting diamond could be explained by the standard BCS approach. There were two main alternative models that challenged the BCS superconductivity of diamond. The first called 'impurity band resonating valence bond' and was introduced for diamond in (78). Resonating valence bond (RVB) theory was first introduced to explain the high temperature superconductivity in copper oxide lattices (79). The simple premise is electrons from neighboring copper atoms interact to form a valence bond. According to this theory a covalent bond is formed between atoms by the overlap of half filled valence atomic orbitals of each atom containing one

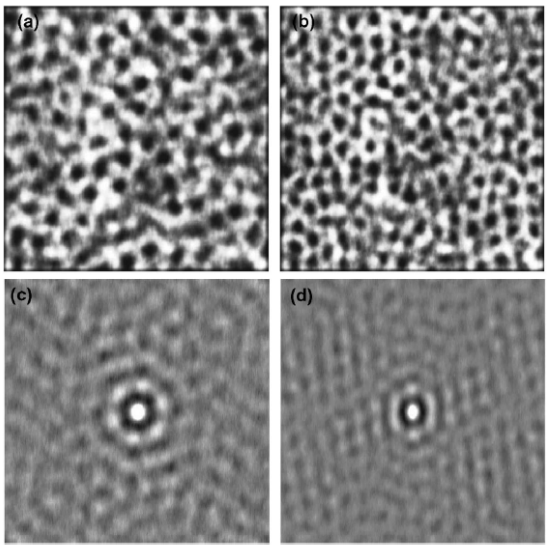

FIGURE 3.7 Top: vortex images ($1.5 \times 1.5 \mu m^2$) at two different magnetic fields: (a) 1200 Oe, (b) 1900 Oe. Bottom: two dimensional auto correlation function calculated from the above vortex images. Reprinted figure with permission from (23) DOI Copyright (2006) by the American Physical Society.

unpaired electron. Valence bond theory considers that the overlapping atomic orbitals of the participating atoms form a chemical bond. Valence bond theory views bonds as weakly coupled orbitals (small overlap). Increased doping increases the electrons within this band which can act as mobile Cooper pairs which are able to superconduct.

Initial measurements of the band structure of diamond supported this theory (80). Although a staple observation for this theory is the measurement of a the pseudo gap (81). This energy gap is different from the usual energy gap in superconductors which appears at T_C and is termed 'pseudo-gap' because it has no direct relationship with T_C. It refers to an energy range (normally near the Fermi level) which has very few states associated with it as opposed to no states. The pseudo-gap exists over a wide range of temperature and doping.

Figure 3.8 shows the temperature-Sr doping concentration (x) phase diagram for the $La_{2x}Sr_xCuO_4$ compound. The doping concentration is proportional to the hole concentration and x is number of holes per CuO_2 layer, page 123 of (82).

The under-doped region of the material is an anti ferromagnetic insulator. Below a temperature T^* and above T_C the material has a pseudo-gap phase. The transition between the Fermi liquid and strange metal occurs gradually and there is no sharp boundary between the two phases. Superconductivity occurs between

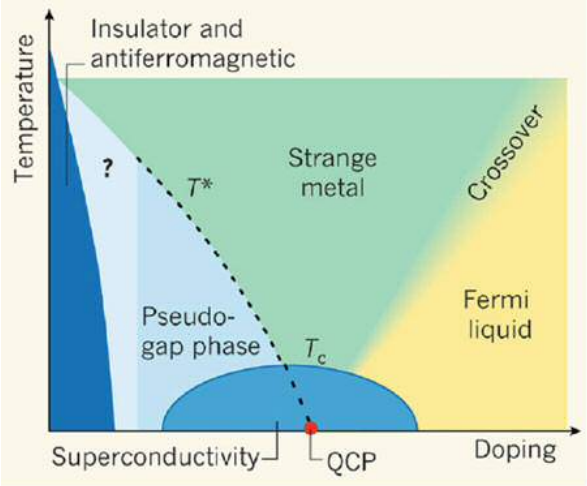

FIGURE 3.8 Temperature-Sr doping (x) phase diagram of the $La_{2x}Sr_xCuO_4$ compound. Reprinted by permission from Springer Nature, Nature (83) DOI Copyright (2010).

$x = 0.06$ and $x = 0.3$, with the the highest value of T_C found at $x = 0.2$. QCP indicates the quantum critical point, where T^* becomes zero. Over doping the sample ($x \geq 0.34$) leads to the disappearance of superconductivity. There is uncertainty over whether the pseudo gap is a precursor to the superconducting gap (79) and or coexists alongside the superconducting gap (84). Further discussion of this competing is beyond the scope of this thesis. To date no such phase diagram (figure 3.8) exists for boron doped diamond, nor has a pseudo gap been measured.

The second scenario suggested that the experimentally observed weak localization effects at low temperatures were a precursor to an unconventional pairing mechanism involving spin-flip transitions (85; 86). Spin fluctuation theory is based upon the premise that the full treatment of charge and spin degree of freedom of the electrons predicts an attractive component of the interaction between electrons without invoking the phonon mediation. The energy gap for this theory is significantly greater than for BCS theory.

None of these results explain the superconductivity of diamond as well as BCS theory. The major experimental results which showed that superconducting diamond had BCS-like behaviour came from the measurement of the energy gap. Such measurements have been undertaken below T_C and mainly though STM measurements (87; 22; 23).

Ref. (23) measured single-crystalline boron-doped diamond using scanning tunnel spectroscopy (STS), as previously discussed. The authors probed the density of states of the sample by applying a small ac modulation of 10 V to the sample-tip DC bias voltage and measuring the differential conductance

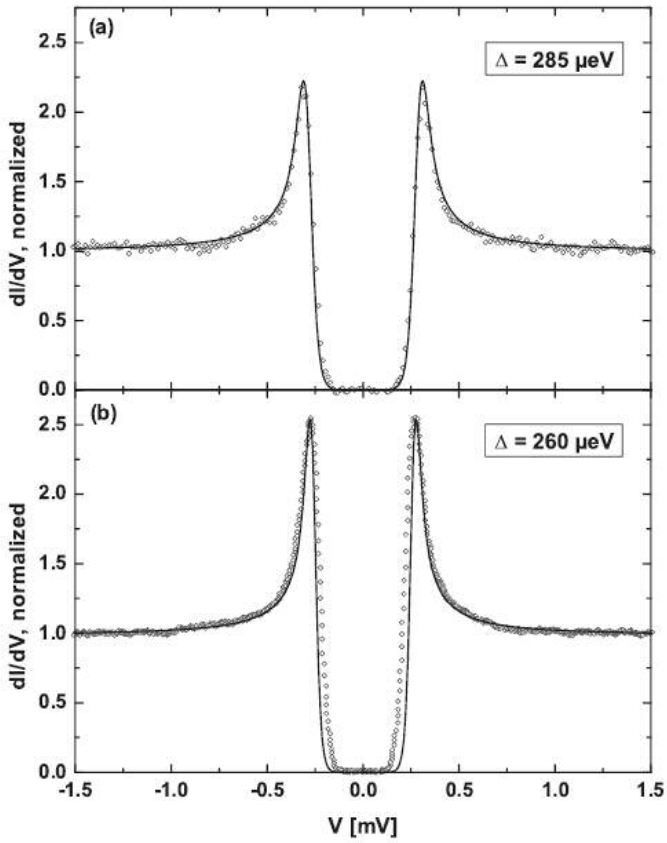

FIGURE 3.9 Experimental normalized tunneling conductance measured at 70 mK (open circle). Solid lines correspond to BCS fits with: (a) $\Delta = 285\mu$eV and (b) $\Delta = 260\mu$eV. Reprinted figure with permission from (23) DOI Copyright (2006) by the American Physical Society.

$G(V) = \frac{dI}{dV}(V)$ measurements. Figure 3.9 show two representative differential conductance curves performed at 70 mK with a tunnel resistance of 20 MΩ. Most of the experimental spectra can be well reproduced by a theoretical BCS density of states as can be seen in figure 3.9(a). The fit gives a superconducting order parameter $\Delta = 285 \pm 2\mu$ eV. The authors obtained slightly smaller values of Δ for the same sample in a separate experiment (23), see figure 3.9(b). They attribute the differences to either the result of spatial macroscopic in homogeneity of the doping or be the consequence of variation in the chemical cleaning of the surface prior to each run.

The temperature dependence of Δ displayed in figure 3.10 is well described by the BCS theory with a critical temperature of 1.85 K very close to the superconducting transition temperature of 1.9 K obtained by AC susceptibility and transport measurements. This clearly demonstrates that boron-doped diamond is well described by BCS superconductivity with a measured ratio $2\Delta(0)/(k_B T_C) = 3.48$.

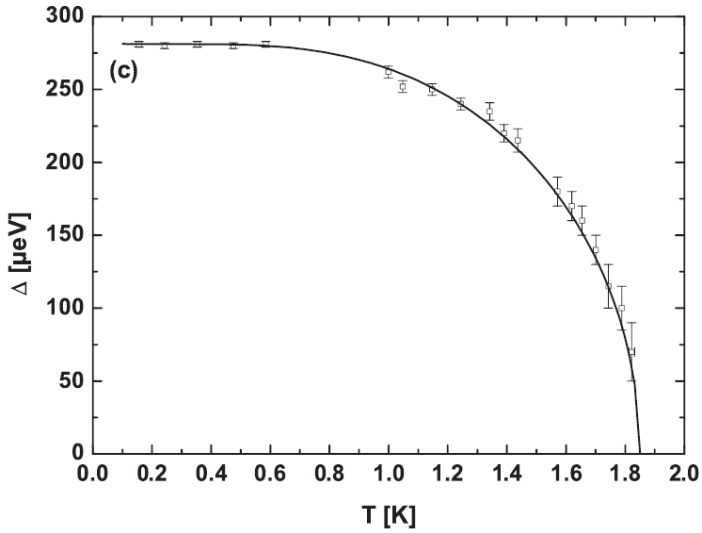

FIGURE 3.10 Temperature dependence of the BCS gap (open squares) compared with the BCS law (2.44) with Tc = 1.85 K (solid line). Reprinted figure with permission from (23) DOI Copyright (2006) by the American Physical Society.

Ref. (87) and (22) used STS measurements on polycrystalline films to demonstrate BCS like superconductivity. Ref. (87) finding that their temperature dependence of the energy gap followed (2.44) and $2\Delta/(k_B T_c) = 3.7$ when $T < T_C$. Ref. (22) went further and showed that whilst the intrinsically superconducting grains of diamond follow the BCS model, the grain boundaries predominantly show metallic-conduction. The connection between the superconducting grains likely being due to the superconducting proximity effect. It is therefore appropriate to consider the BNCD samples looked at in this work as a disordered collection of coupled superconducting grains. (12).

3.3 FILM GROWTH

3.3.1 SUBSTRATE

All the films used for this thesis were grown on a a 500 nm thick buffer layer of silicon dioxide, which coated a 500 μm thick p-type silicon (100) wafer of 2-inch diameter. Before growth these wafers were cleaned using the standard SC1 process of 30% H_2O_2:NH_4OH: deionized (DI) H_2O (1:1:5) at 75 °C for 10 minutes. The substrates were then rinsed in DI H_2O in an ultrasonic bath for 10 minutes

and spun dry. For the seeding step (or nucleation enhancement) the wafers were placed in a mono-dispersed nanodiamond (with a diameter of $\sim$ 5 nm) and DI H_2O colloid which was then agitated in an ultrasonic bath for 10 minutes. This process encourages the nanodiamond particles to bond to the surface of the substrate via electrostatic attraction and is known to produce nucleation densities exceeding $10^{11} cm^{-2}$ (88). After this the wafers were rinsed, spun dry at 3000 rpm, and then immediately placed inside the CVD chamber.

3.3.2 BORON DOPED FILMS

In an effort to study how film thickness, and by extension grain size, effects BNCD superconductivity a series of BNCD films were grown to a range of different thickness's between 160-564 nm. Chapter 4 characterises the J_C, T_C and the superconducting volume fraction of these films using AC susceptibility measurements. This will all be discussed further in said chapter. The thickest sample in the (564 nm) is used in both the AC susceptibility experiment and in chapter 6 a pinning potential is calculated for it using a magnetic relaxation process.

During CVD growth these films substrates were held at $\approx 720^{\circ}C$ in a dilute gas mixture of methane and trimethylboron in hydrogen, with a 3% methane concentration and a B/C ratio of 12,800 ppm, and a chamber pressure and microwave power of 40 Torr and 3.5 kW, respectively. The growth time was varied across the set such that the film thickness's were in the aforementioned range; the B/C ratio was not changed between samples and therefore the boron concentrations can be assumed to be consistent (89).

Scanning electron microscope (SEM) images were taken of these films surface using the in-lens detector of a Raith eline system operated at 20 kV and a working distance of 10 mm. Figure 3.11 shows said SEM images and one panel shows the mean grain diameter as a function of film thickness. Panel A) being the thinnest film and panel E) the thickest. Panel F) shows grain-size analysis results performed by Klemencic from (11). These give a measure of the mean grain diameter, shown as a function of film thickness. As has already been stated it is expected that the crystal size increases with film thickness; however these results show that the effect is noticeable within the thickness range of 160 nm to 564 nm. This difference in crystal size compared with grain boundaries will have an influence on the T_C, volume fraction and J_C, which will be discussed more in chapter 4.

3.3.3 INSULATING FILMS

The final experimental chapter of this thesis uses NCD thin films. The NCD thin films were grown $\approx$ 360 nm thick on the chosen substrate. CVD was carried out under 3% CH_4/H_2 conditions at 47 Torr and 4.2 kW microwave power. Upon termination of growth the films were cooled down in hydrogen plasma to ensure hydrogen termination and prevent deposition of non-sp^3 material. Substrate temperatures were $\approx$ 830 °C as determined by dual-wavelength pyrometer, with substrate heating solely from the microwave induced plasma. Film thickness was determined *in situ* through the use of laser interferometry, and *ex situ* with a Filmetrics F-20 Spectral Reflectance system. The system was modelled as roughness on diamond on silicon dioxide on silicon. Known values of k and n were used for the diamond, silicon dioxide and silicon from the Filmetrics database to determine the thickness.

Since the boron is simply incorporated into the diamond films its surface is as rough as NCD films. The effect of CMP upon the superconductivity of a BNCD film was studied in (90). This paper showed that their BNCD film retains superconductivity following more than 10 hours of polishing. The BNCD film used for this study was grown in the same system and on the same substrate as the aforementioned samples grown for this thesis. After an identical seeding of the substrate the film was grown in a dilute gas mixture of methane and trimethyl-boron in hydrogen, with a 3% methane concentration and a B/C ratio of 12,800 ppm. The chamber pressure and microwave power were 40 Torr and 3.5 kW respectively. The substrate temperature was $\approx$ 720°C during growth, as measured in situ with a dual wavelength pyrometer. The as-grown film thickness was determined by in situ pyrometric interferometry to be 520 nm. This thickness was obtained after a deposition time of 150 min, after which the film was cooled in a hydrogen plasma and subsequently removed from the reactor chamber. This result will be discussed further in chapter 6 and shows that the conclusions can be applied to BNCD films as well as the NCD films.

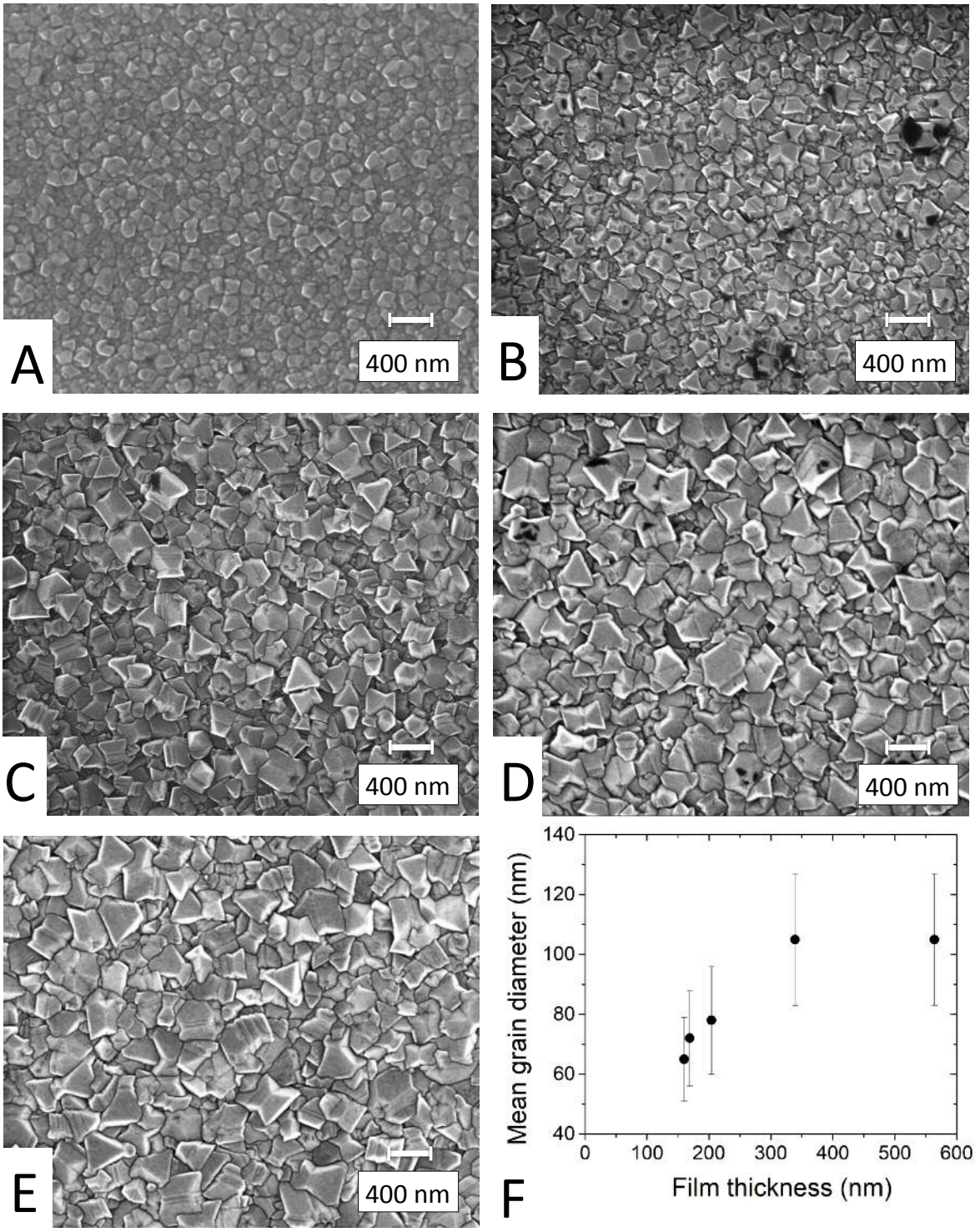

FIGURE 3.11 SEM of the films, with panel A) being the thinnest increasing sequentially until the thickest film shown in panel E). F) shows grain-size analysis results from ref. (11). These give a measure of the mean grain diameter, shown as a function of film thickness. It is clear from these images that as the thickness of the film increases so does the grain size. This variation will influence the films superconductivity.

CHAPTER 4
AC SUSCEPTIBILITY OF BNCD FILMS

This chapter deals with the measurement of the AC susceptibility of BNCD five films with thickness variation between $160 - 564$ nm. AC susceptibility and its relation to magnetization will be defined therein. This study investigates how T_C, J_C and the percentage of film which is superconducting changes with film thickness. As described in the previous section these films were grown under identical conditions with only the thickness, and therefore the crystal size and grain boundary varying. This chapter shows that as expected the increase in thickness and crystal size shows an increase in T_C. The measured T_C values for these films are then compared and discussed against published resistivity results of nominally the same films (11). The AC susceptibility behaviour of all the BNCD films through the transition are shown to follow that of granular high temperature superconductors. The thickest film's J_C is calculated and compared with current typical values for diamond films. Finally typical volume fraction calculations are shown to be inadequate for the calculation of the superconducting fraction of the BNCD films.

4.1 INTRODUCTION

Susceptibility (χ) is a dimensionless proportionality constant that indicates the degree of magnetization of a material in response to an applied magnetic field, defined as

$$\chi = \frac{M}{H} \tag{4.1}$$

(91; 92) M is the magnetization of the sample and H is the magnetic field applied to the sample. In an AC susceptibility measurement the applied field H is varying

so (4.1) is changed to

$$\chi = \frac{dM}{dH_{ac}} \tag{4.2}$$

During a single AC susceptibility measurement the sample is kept stationary whilst the field oscillates causing a time-dependent moment response. This is in contrast to DC measurements where the field is constant and the sample is oscillated. This type of measurement will be discussed in chapter 5. The AC χ is not the same as the DC χ but in a low frequency regime they are similar (93).

The benefit of taking AC susceptibility measurements is that this process is able to probe the entire sample volume and provide a volume average of the sample's AC magnetic response. This can be contrasted with resistivity measurements, which only require a superconducting pathway between contacts to measure zero resistance. AC susceptibility has become wide spread as a method of measuring different features of polycrystalline high-T_C superconductors (91; 94; 95; 93).

The AC susceptibility measurement yields two quantities: the magnitude of the susceptibility, χ, and the phase shift, θ (relative to the drive signal). These values are converted into their more useful form (manually or via experimental set up) of an in-phase, or real, component χ' and an out-of-phase, or imaginary, component χ''. The two representations are related by

$$\chi' = \chi \cos\theta \tag{4.3}$$

$$\chi'' = \chi sin\theta \tag{4.4}$$

$$\chi = \sqrt{\chi'^2 + \chi''^2} \tag{4.5}$$

$$\theta = \arctan(\chi''/\chi') \tag{4.6}$$

(96) In the limit of low frequency where AC measurement is most similar to a DC measurement, the real component $\chi' \equiv$ DC χ. For the following experiments this condition was met by applying a frequency of 500 Hz. The imaginary component, χ'', indicates dissipative processes (energy loss) in the sample, which for superconductivity would predominantly be magnetic irreversibility and flux flow losses (96).

4.2 EXPERIMENTAL METHOD

4.2.1 EQUIPMENT

The films were measured in a Quantum Design Physical Properties Measurement System (PPMS), using the AC Measurement System (ACMS) option. A schematic of the AC susceptometer in the ACMS option can be seen in figure 4.1. The sample is suspended in a He_4 partial vacuum inside the ACMS coil set. Surrounding the sample space is two separate detection coils (called the secondary coils) and at the centre of each detection coil there are two single-turn calibration coils connected in series. Around this set up is the AC drive coil (or primary coil). Figure 4.2 shows a simplified close up of this section.

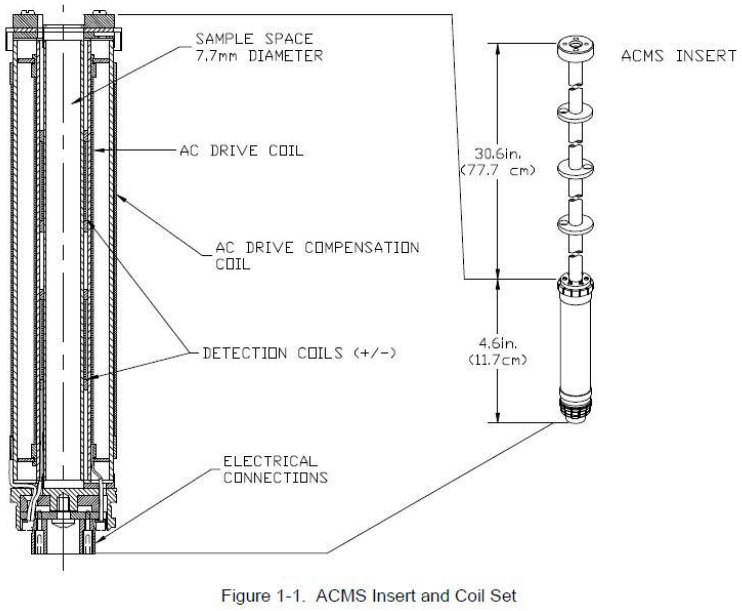

FIGURE 4.1 Reprinted acms coil set up schematic from (92), ©Quantum Design, Inc. 2019.

During the AC susceptibility measurement, an alternating magnetic field was applied to the measurement region using the primary coil. The system uses a 5 point measurement process that utilizes the calibration coils. The first measurement was taken with the sample positioned in the centre of the bottom detection coil. Then the sample was positioned in the centre of the top detection coil, and then in the centre of the bottom coil again. When the bottom-top-bottom coil readings were complete, the sample was placed at the centre of the detection coil array so that it is

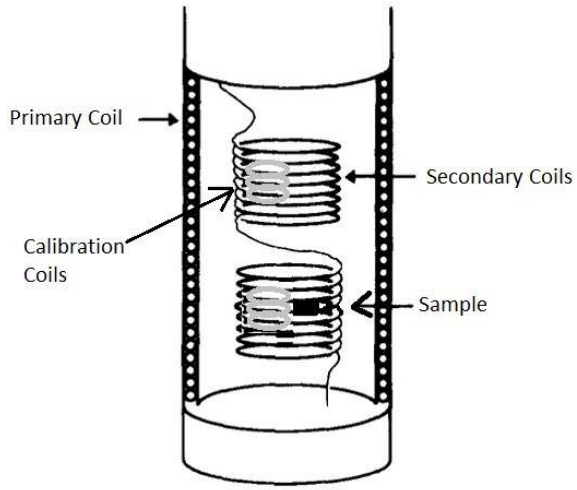

FIGURE 4.2 Simplification of the drive coil and detection coils. Reproduced from (91) DOI, with the permission of the American Association of Physics Teachers.

between the two detection coils. Two more readings are taken with the calibration coils switched into the detection circuit with opposing polarities.

During bottom-top-bottom coil readings, the signals from the detection coil array are amplified, low-pass filtered, and digitized by an analogue-to-digital converter (ADC). The points are fitted and compared to the driving signal to determine the real and imaginary components of the response when the sample is in the centre of each detection coil. (Real components are in phase with the driving signal and imaginary components are 90° out of phase with the driving signal.) The two calibration readings are subtracted to yield a calibration vector in the complex plane. Subtracting the two calibration readings subtracts out the sample signal, leaving only environmental and instrumental factors that affect the reading. The calibration vector is used to accurately place the sample vector at the origin with the proper orientation and scaling. The true values of interest for the sample are then reported: the moment amplitude and phase (magnitude and angle of the sample vector) and the in-phase and out-of-phase (or quadrature) components of the moment (real and imaginary components of the sample vector.)

4.2.1.1 A NOTE ON UNITS

The PPMS outputs the magnetic moment in units emu (92), which are part of the centimetre-gram-second (CGS) system. The applied fields were also stated

in CGS units. For ease all of these quantities are converted to SI units. It is for conversion purposes that the samples dimensions in the next section are stated in cm^3. The following conversions were used

Quantity	Symbol	CGS units	Conversion factor	SI units
Magnetic field strength	H	oersted (Oe)	$\frac{10^3}{4\pi}$	A/m
(Volume) magnetization	M	$\frac{emu}{cm^3}$	10^3	A/m
Magnetic moment	m	emu	10^{-3}	Am^2

4.2.2 PREPARATION OF SAMPLES

Small rectangular sections were cut from the grown wafers in order to fit into the PPMS. The samples needed to be $< 5 \times 5\ mm^2$ in order to fit into the sample chamber. They do not need to be the same size as the susceptibility calculation divides the signal by the volume, it is a measure of the material per unit volume. They were mounted into a clear plastic straw so that the field could be applied perpendicular to the samples. The separate samples had the following parameters:

Diamond Thickness (cm)	Length (cm)	Width (cm)	Diamond Volume (cm^3)
5.64 x 10^{-5}	0.41 ± 0.01	0.28 ± 0.01	6.47 ± 0.28 x 10^{-6}
3.39 x 10^{-5}	0.38 ± 0.01	0.33 ± 0.01	4.25 ± 0.17 x 10^{-6}
2.04 x 10^{-5}	0.35 ± 0.01	0.33 ± 0.01	2.36 ± 0.10 x 10^{-6}
1.68 x 10^{-5}	0.48 ± 0.01	0.29 ± 0.01	2.34 ± 0.09 x 10^{-6}
1.60 x 10^{-5}	0.41 ± 0.01	0.38 ± 0.01	2.49 ± 0.09 x 10^{-6}

4.2.2.1 SIGNAL OF SUBSTRATE

The substrate the films are grown on has a thickness of 0.05 cm. The volume of the diamond films and the volume of the substrate differs by at least 3 orders of magnitude. The substrate consists of a 500 nm layer of silicon dioxide coated on p-type silicon. Silicon dioxide is weakly diamagnetic with $\chi' \sim -10^{-6}$ (97). Heavily doped p-type silicon can behave like a superconductor when doped to a resistivity of 160 μ Ω.cm and below 0.5 K (72; 98). However the substrate was doped to a resistivity of 1-20 Ω.cm and will show a weak diamagnetic signal $\chi' \sim 10^{-6}$ (99; 97). Therefore these materials will not undergo a superconducting transition and the majority of the signal below the T_C will be due to the diamond film. The T_C for this chapter refers to the T_C onset for the AC susceptibility. BNCD also shows a weak diamagnetic signal above T_C; therefore the volume difference

becomes important at temperatures higher than this. The majority of the signal when the sample is above T_C will then be due to the substrate.

A sample (cross sectional area $\approx 0.16\ cm^2$) of the substrate only was measured in the same set up in order to obtain some magnetic moment estimations. Figure 4.3 shows the results of this measurement.

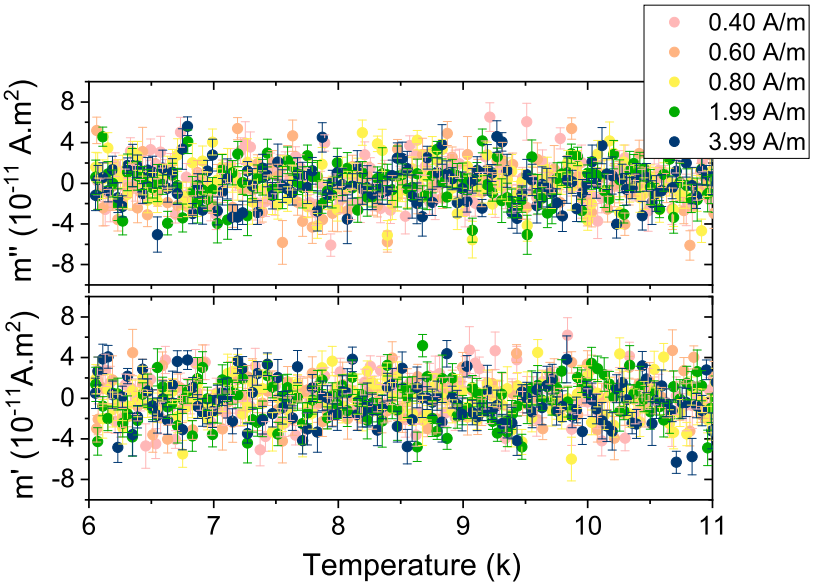

FIGURE 4.3 Moment versus temperature for a rectangle piece of the substrate without any diamond grown on it. The temperature range is higher than the measurement range for the diamond; there is no reason given the literature on these substrates to assume that this signal will change by at least 2 orders of magnitude between 6 K and 2 K. The measurement field range is the same as that of the diamond film measurements.

The temperature range is 1 K higher than that of the diamond film measurements, however there is nothing in the literature to suggest that the signal is going to change by 2 orders of magnitudes, see figure 4.7, for the diamond films. The increase in fields also does not increase the signal above the noise. The PPMS sensitivity is $\sim 10^{-11} A.m^2$, so the substrate does not give a clear signal above the background noise. Although there are some spikes in the noise that reach $6 \times 10^{-11} A.m^2$, which could be from the substrate.

Whilst there is only at best a very small signal in the noise the BNCD film measurement output has a signal of this scale above T_C, which will be seen in figure 4.7. Therefore the volume difference between substrate and diamond is considered for the calculation of the volume fraction. Since the majority of the signal is due to the diamond after T_C onset only this volume was used to calculate

the magnetization and the subsequent susceptibility. Before the T_C onset the diamond and the substrates are behaving in a similar way so the greater volume (i.e. the substrate) is used for the volume fraction calculations.

TABLE 4.1 Volume of the diamond and substrate for each thickness

Diamond Thickness (nm)	Diamond and substrate volume (cm^3)
564	5.75 ± 0.25 x 10^{-3}
339	6.27 ± 0.25 x 10^{-3}
204	5.73 ± 0.24 x 10^{-3}
168	6.96 ± 0.28 x 10^{-3}
160	7.79 ± 0.28 x 10^{-3}

4.2.3 METHOD

The chosen sample was cooled to 2 K with a constant residual background field of 3.48 A/m. An AC field with a frequency 500 Hz was then applied perpendicular to the sample and the system was warmed at a rate of 0.05 K/min to 5 K. There were 5 chosen measurement fields 0.40 A/m, 0.60 A/m, 0.80 A/m, 1.99 A/m and 3.99 A/m. After completion of measurement the sample was cooled again to 2 K with the same background field; the process was then repeated with a different higher applied AC field. These were chosen so that the full transition can be observed in the temperature range. T_C is taken to be at the onset of a significant non-zero value of χ' (100; 101).

The PPMS outputs real and imaginary components of the change in the measured magnetic moment of the sample. The magnetization can be calculated from the moment using the relation (2.49) and then χ' and χ'' can be calculated using (4.2).

Figure 4.4 shows an example of the measurement output in terms of the real and imaginary components of the change in magnetic moment (plotted in units of $A.m^2$) of a piece of niobium wire (Nb wire). This measurement was taken as a reference sample for the volume fraction calculations which diamond could be compared against. The sample was flattened to mimic a rectangular shape and had the dimensions 0.3371cm $\times$ 0.0663cm $\times$ 0.009cm (length$\times$width$\times$height).

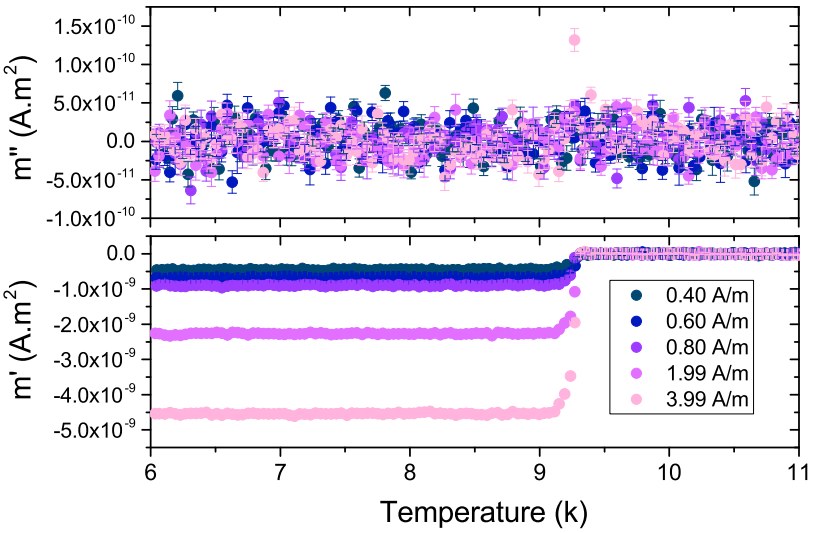

FIGURE 4.4 The real (m') and imaginary (m'') magnetic moment versus temperature data set for the flattened Nb sample, taken as a test run for the volume fraction calculations.

4.2.3.1 VOLUME FRACTION AND DEMAGNETIZATION

In SI units the volume susceptibility is calculated as a dimensionless factor. If the whole volume of the material is superconducting then it will have the idealised values $\chi' = -1$ and $\chi'' = 0$ when $T < T_C$. Further to this if $\chi' = -0.8$ then only 80% of the sample is superconducting and so on.

The χ discussed thus far is actually the external susceptibility. The sample's orientation and geometry influences the magnetic field it experiences (95; 93). External (χ_{ext}) can be measured to values of -2800 in SI units (95; 102) an absurd value unless such properties are considered. Typically the sample orientation and geometry can be accounted for by considering a numerical demagnetization factor N, which relates the internal and external field in a uniformly magnetized material

$$H_{in} = H_{ext} - NM \tag{4.7}$$

H_{in} is the internal magnetic field experienced by the sample and H_{ext} is the externally applied field.

The internal susceptibility χ_{in} which is characteristic of the material can then be given by

$$\chi_{in} = \frac{\chi_{ext}}{1 - N\chi_{ext}} \tag{4.8}$$

(95; 93; 103; 104)

AC susceptibility is complex, (4.5) shows therefore that $\chi_{ext}^2 = {\chi'}_{ext}^{\,2} + {\chi''}_{ext}^{\,2}$ or $\chi_{ext} \equiv {\chi'}_{ext} + \chi''_{ext}$. The internal susceptibility is also $\chi_{in} \equiv {\chi'}_{in} + \chi''_{in}$. The two susceptibilities are related by:

$$\chi'_{in} = \frac{\chi'_{ext} - N({\chi'_{ext}}^{\,2} + \chi''^2_{ext})}{N^2({\chi_{ext}}'^2 + \chi''^2_{ext}) - 2N\chi'_{ext} + 1} \tag{4.9}$$

$$\chi''_{in} = \frac{\chi''_{ext}}{N^2({\chi_{ext}}'^2 + \chi''^2_{ext}) - 2N\chi'_{ext} + 1} \tag{4.10}$$

(95; 93; 103)

A demagnetization factor only works for homogeneously magnetized ellipsoids with linear magnetic response; these three requirements usually are not satisfied in superconductors with vortex pinning (105), which as chapter 6 will discuss further these BNCD films show. The internal susceptibility of the Nb film is calculated using the above, the results of which are shown in the next section, as a comparison for the BNCD films.

4.2.3.2 DEMAGNETIZATION VALUES

A comprehensive list of demagnetization factors for completely shielded rectangular prisms was calculated in (106). When referring to the literature the demagnetization factor of interested is the "magneto-metric" demagnetizing factor N_m which shall just be referred to as N the alternative demagnetization is not relevant for this measurement set up. This is the average magnetization over the entire specimen and is therefore appropriate for the magnetometer measurements of small samples. These values are laid out according to the ratios c/a and $b/max[c,a]$ where $a \times b \times c$ which is equivalent to width×length×height. The height c being along the direction of the applied field. These ratios were calculated when considering just the diamond film volume and then considering the diamond film and substrate volume. For only the diamond film volume and therefore the signal below T_C N $= 0.98$; for the diamond and the substrate will be denoted as D to distinguish it. These values varied more across the films and are shown in table 4:2 The demagnetization for the Nb wire is $N_{Nb} = 0.79$.

TABLE 4.2 Table showing the value of the volume of the diamond and the substrate

Diamond Thickness (nm)	D
564	0.76
339	0.73
204	0.73
168	0.78
160	0.84

Figure 4.5 shows the result of using the method set out in section 4.2.3.1 on the Nb wire. As expected the sample is fully superconducting giving a value of $\chi_{in} \approx -1$. [1] There is some strong variation in signal before the transition and post transition it is clear there is a significant decrease in the AC losses. As a result of getting this expected measurement the same process is applied to the diamond in section 4.3.

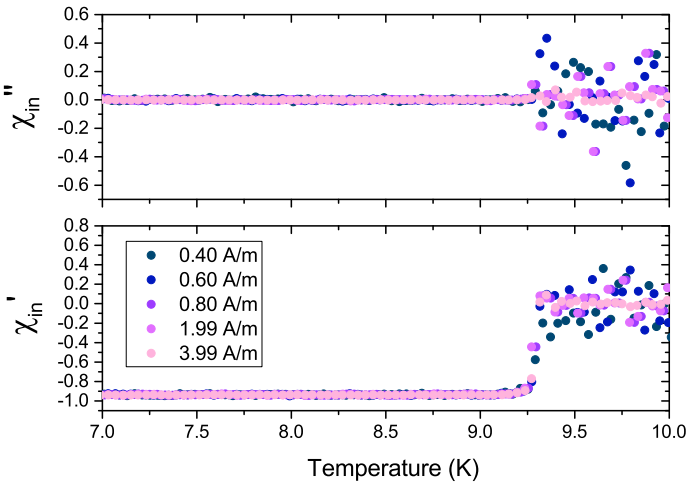

FIGURE 4.5 Real and imaginary components of the internal susceptibility versus temperature for the NbWire.

4.2.4 CALCULATION OF J_C

There are various different methods of calculating the J_C of a sample from AC susceptibility methods (107; 108; 109). This thesis utilises a method which finds

[1] The actual value, as can be seen from figure 4.5, of χ_{in} is -0.95. This variation from -1 is probably due to the approximation of the demagnetization factor N; which was found assuming the Nb sample was an ideal rectangle. When in fact, as stated earlier, it was a piece of niobium wire flatten to an approximate rectangle.

the peak in the imaginary susceptibility, introduced by Herzog *et al* (107).

The imaginary component of the susceptibility is non zero for temperatures slightly below T_C when dissipative losses occur in the sample. In such cases a curve or peak like the example in figure 4.6, taken from (103), is measured through the transition. This shape would be expected for measurements of BNCD films with it being a type II superconductor and the granular features resulting in pinning throughout the sample.

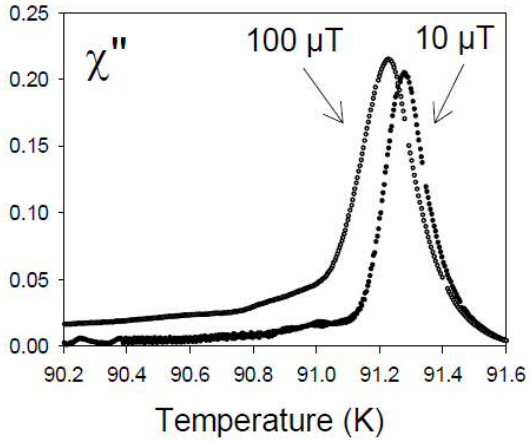

FIGURE 4.6 Showing the imaginary behaviour of the internal AC susceptibility vs. temperature measured for a large, single grain YBCO pellet. A fixed frequency f = 103 Hz was used and the amplitude of the AC field was either 10 μT or 100 μT. Image adapted from (103) DOI

As previously stated χ'' is equivalent to the AC losses in the sample. These losses relate to the obstruction of the motion of the alternating applied field in and out of the sample. In the specific case of a type II BNCD film the possible obstructions that lead to these losses will be due to the geometry of the film and its magnetic irreversibility. The latter will change through the transition and this in relation to the shielding of the same is what causes the shape. Before the onset of superconductivity there are no shielding currents and the applied magnetic field is able to penetrate into the sample's centre. As the temperature decreases type II superconductors will enter the vortex state. As this happens the area of the sample being shielded will start to increase but so to will its ac losses. The vortices will have less energy and more will be pinned and unable to move. The peak in the $\chi''(T)$ curve happens just before the centre of the sample becomes shielded. After this the shielding currents being to screen a greater volume of the sample and the losses

start to decrease due to narrowing the zone with non-zero shielding current. As the sample completes the transition $\chi'' = 0$.

Figure 4.6 also shows three important trends for χ''. Firstly, as the field increases the maximum of χ'' shifts to lower temperatures. This is due a lower temperature needing to be reached in order to achieve the same volume shielding. The peak also becomes more asymmetric and this will correspond with a broadening of the χ' transition. This behaviour reflects the temperature dependence of the effective lower critical field H_{C1}. The height of the peak χ'' will show some field dependence, increasing as the field does, until it saturates (107). These features have been identified as they will be relevant in the critical current density calculations.

Typically if the peak of the imaginary susceptibility is being used to calculate the critical current then Bean's critical state model is applied. If this is the case then J_C cannot exceed a critical value and vortices penetrate only so far that this holds true. Within the Bean's model then the magnetic moment depends only on the applied field magnitude, direction and the sample geometry. As described in section 4.2.3 the peak corresponds to the last point when the sample is in the vortex state but the applied field ($H_{applied}$) is still able to reach the centre of the sample. At this point $H_{applied}$ is equivalent to the penetration field ($H_{penetration}$). The penetration field is geometry specific and gives a value that relates this changing field to the constant critical current density (95; 110). Although equivalent as the field is increased the values of J_C will monotonically increase until $H_{applied} = H_{penetration}$, at which point J_C saturates. J_C calculations using AC susceptibility will typically focus on the temperature or field dependence in order to show its appropriate scaling behaviour (108; 109).

The samples in this thesis are rectangular (or strip) thin films with a field applied normal to the film plan. Analytical expressions for the AC susceptibility of thin disks in perpendicular field was derived in 1994 (110) followed by expressions for thin long strips and squares (108). Herzog *et al* compared measured and theoretical values of the real and imaginary components of the susceptibility of a disk, a strip and a ring. They compared these susceptibility components using a coles-coles plot, χ' versus χ'', the results of the comparison between the rectangle and the disk can be seen in figure 4.7.

The χ' and χ'' plotted are the external susceptibility of these samples normalized to ideal values when the sample has finished transitioning; so when $\chi' = -1$ and

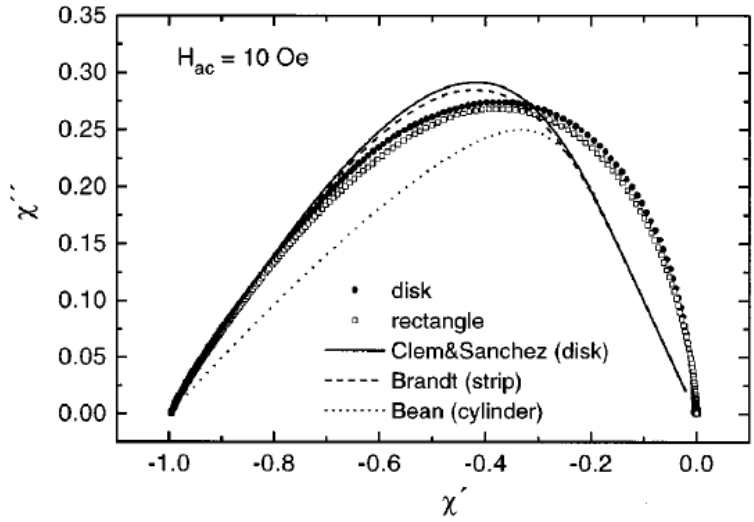

FIGURE 4.7 A coles-coles plot showing the temperature dependence of the susceptibility determined for a rectangle and a disk both patterned from a $YBa_2Cu_3O_{7-\delta}$ film. The corresponding theoretical predictions are added by the symbols defined in the inset. Reprinted figure with permission from (107) DOI Copyright (1997) by the American Physical Society.

$\chi'' = 0$. This decision hinges on the fact that the samples are polycrystalline films of the well-understood high temperature superconductor, $YBa_2Cu_3O_{7-\delta}$, which were produced using a method known to result in a 100% superconducting material. Given that part of this chapter is concerned with the calculation of the internal susceptibility this shall be attempted first as opposed to normalizing the susceptibility.

Herzog *et al* found, as can be seen in figure 4.7, that there was only 1% or less difference between the measured behaviour of the disk and the rectangle. Especially the slopes at the low and high temperature end corresponding to $\chi' = -1$ and 0, respectively, are found to be practically independent of the sample shape. The different shapes manifest themselves only in small characteristic variations of the height of χ'' in agreement with the Brandt and Clem and Sanchez models. The magnitude of χ'' is overestimated by the theory by $\approx 7\%$ which they conclude as due to the a weak dependence of χ'' on H_{ac}, which was measured to follow the trend seen in figure 4.8. An increase in the field will increase the peak towards this ideal value. There is also a discrepancy in the range $-0.2 \leq \chi' \leq 0$. Herzog *et al* attribute this to a field dependence of J_C which is not covered by the Bean model or being the result of alternative loss mechanisms like flux creep which can also increase χ''.

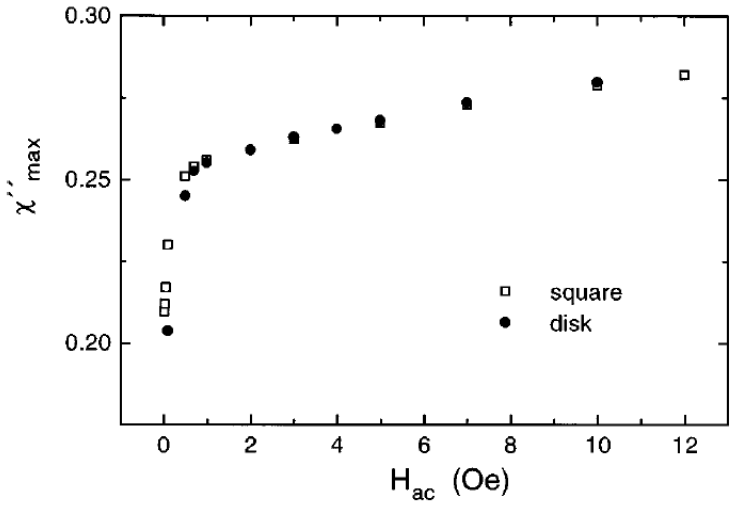

FIGURE 4.8 Maximum value of χ'' plotted as a function of the applied effective magnetic AC field H_{ac}. This is for a square and disk both patterned from a YBaCuO film. Reprinted figure with permission from (107) DOI Copyright (1997) by the American Physical Society.

This thesis compares the experimental results of the BNCD films via a coles-coles plot to the Brandt strip model shown in figure 4.7. The Brandt strip model has the following relations for χ' and χ'':

$$\chi' = -\frac{1}{h}\tanh h \tag{4.11}$$

$$\chi'' = -\frac{1}{h}\tanh h + \frac{2}{h}\tanh\frac{h}{2} \tag{4.12}$$

where

$$h = \frac{H_{applied}}{H_{penetration}} = \frac{H_{applied}\ \pi}{J_C\ d} \tag{4.13}$$

Comparing against this model it will be possible to see if the BNCD films show the same variations from the model as a polycrystalline type II superconductor. Secondly depending on how closely the experimental results follow this model then an approximation of J_C can be calculated. The J_C of interest is the value at the maximum of χ''. As described previously this value is the closest to a true value for the sample due to the nature of the film at this point in the transition. If the experimental results follow the model in the expected way above then the maximum of χ'' can be determined through a cubic spline fitting and subsequent maximum calculation. After determining the maximum of χ'' and a corresponding value of χ' a value of h can be calculated using (4.13). Figure 4.9 shows a plot of the theoretical Brandt model with a line fit and maximum of χ'' found.

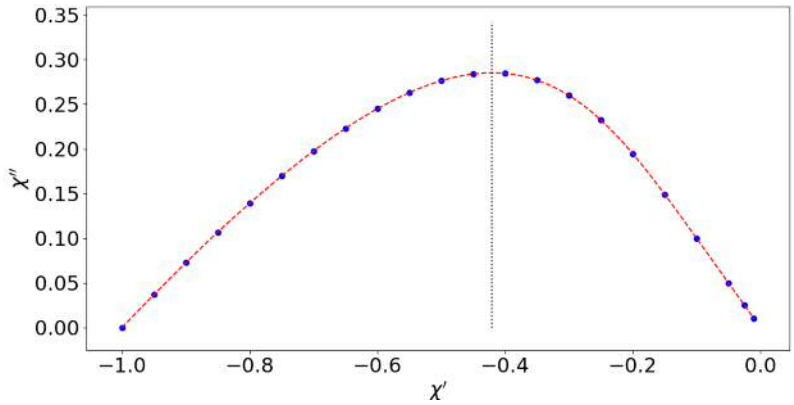

FIGURE 4.9 Calculated ideal values using the Brandt strip model within this χ' range, fitted with a cubic spline curve in order to determine the peak. This peak is marked by the black dotted line at $\chi' = -0.420$ and corresponds to $\chi'' = 0.285$.

4.3 RESULTS

4.3.1 T_C FROM AC SUSCEPTIBILITY

T_C onset was defined as the temperature when the magnetic moment signal was measured to be $\geq -10^{-10} Am^2$. Literature defines a T_C onset as the point when a significant non-zero value of χ' is measured. The measurement sensitivity is $10^{-11} Am^2$ so one order of magnitude greater than this was chosen as the required signal increase to demonstrate superconductivity. Figure 4.10 shows the measured real magnetic moment for all the measured films when a field of 0.40 A/m was applied and demonstrating T_C onset.

This process was performed for all the films and for the all the applied fields. The increase in the applied field was not sufficiently high enough to change the T_C onset for the above films. Therefore the T_C values in figure 4.10 will be compared to the T_C values from the resistivity measurements. The T_C offset by comparison varied depending upon the applied field. Therefore T_C offset will not be compared with the resistivity data. A T_C offset is not defined for typical AC susceptibility measurements.

Granular films can show two transitions, the first being intrinsic to the superconductor and the second characteristic of the coupling between the grains. This is

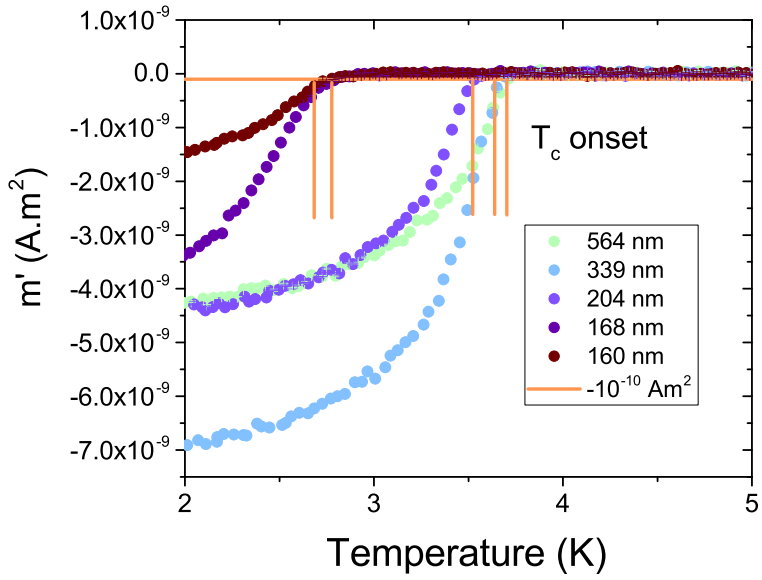

FIGURE 4.10 Real component of the moment measured with an applied field of 0.40 A/m for all the BNCD films. The T_C onset line is plotted in orange. The five vertical lines on the plot symbolise the point taken as the T_C onset for each film.

more typical of samples with greater grain boundaries and weakly coupled grains (95). None of the films showed a double transition in their behaviour. The lack of two transitions suggests that the BNCD film grains are coupled strongly enough that this field range can not separate them.

4.3.1.1 RESISTANCE DATA

Figure 4.11 shows an adjusted image of the data set from (11), where the measured resistance is normalised by its values at 10 K and plotted against the measured temperature. These measurements were taken by Klemencic on different sections of the same BNCD films. Silver paste contacts were made to the sample surface in a four-wire van der Pauw configuration by the author of this thesis.

Ref. (11) is concerned with the variation in conductivity (1 / resistivity) in the vicinity of T_C. In this paper and supplementary material they define T_C as the point when the conductivity diverges. They go onto show that 3D bulk superconducting behaviour only truly occurs at this point. These values are included on figure 4.11. This method of T_C definition varies from typical midpoint definitions in resistance measurements. Typically diamond's critical temperature is reported (40; 75; 111;

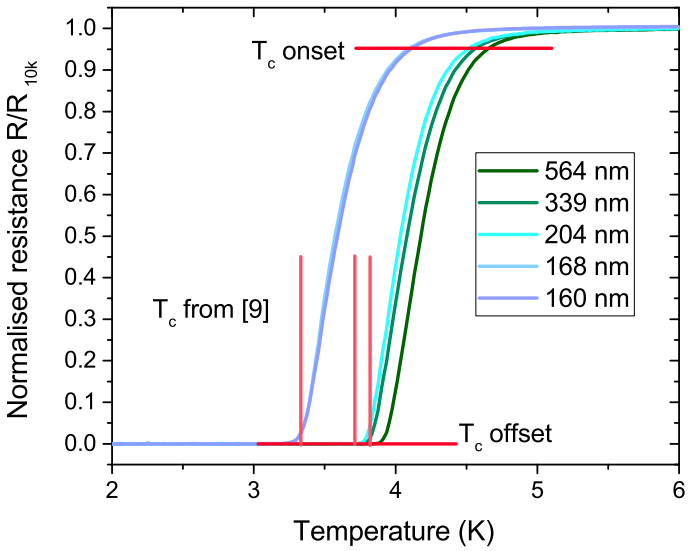

FIGURE 4.11 Resistance data, adapted from (11). The vertical red lines mark the T_C values as defined in (11). T_C onset here is taken as when the resistance for each film drops by 5%. The T_C offset is defined when the normalised resistance reaches zero, marked at T_C zero on this figure.

41; 6) as the T_C onset and the temperature when the resistance is zero, these values are also included on figure 4.10. The T_C onset for the resistance data being defined as a significant deviation from the normal, which is taken as when the resistance has dropped by 5% from it's value at 10 K.

4.3.1.2 CRITICAL TEMPERATURE COMPARISON

Figure 4.12 shows all the T_C values defined so far for each thickness from the BNCD film set. It is clear from all of these that as the film thickness increases the T_C increases. This is exactly expected as the boron concentration will increase with film thickness. The link between boron concentration and temperature having already been discussed in chapter 3.

It is clear from figure 4.12 that there is a significant difference between the resistivity and magnetic measurements defined T_C onset, differing by at least 1 K. This difference in the measurement methods occurs for all the films. The T_C offset and T_C fluctuation (T_C defined by (11)) also appears to occur before the AC T_C onset however the variation is at most 0.5 K for the thinnest films and decreases for the thicker films.

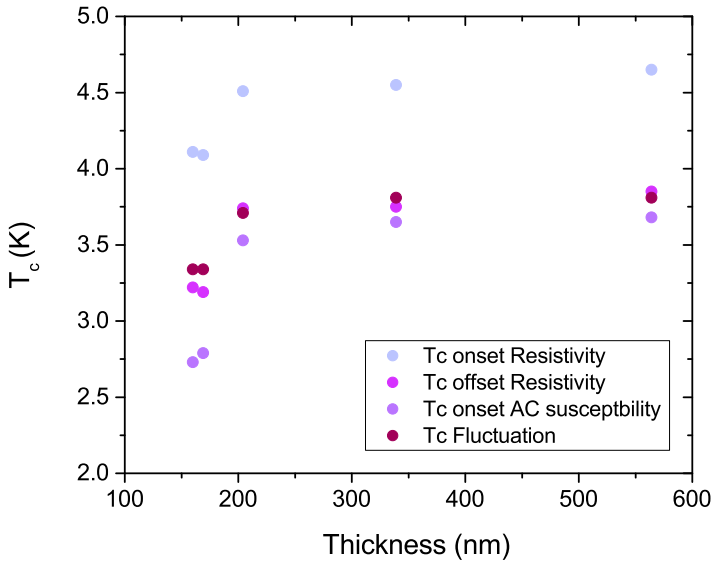

FIGURE 4.12 Comparison of the T_C values defined so far for the BNCD film set.

Looking at these results it seems that the typical resistivity method of stating T_C as the midpoint of the transition, after defining T_C onset and T_C offset, is inaccurate when compared with magnetic measurements. Ref. (11) define their T_C in relation to the conduction. Their results show three distinct fluctuation regions in the conductivity of the BNCD film set during the transition, which come about due to the granularity of the films. They define T_C as the point when the fluctuations have ceased and the conductivity tends to infinity. The AC results show that only once this has happened is the sample able to produce a sufficient Meissner field. This result shows that the only way to extract a reliable T_C from resistivity measurements from BNCD films is to consider T_C fluctuation.

4.3.1.3 VOLUME FRACTION

The same method that was applied to the Nb film was then applied to the measured BNCD films. Figure 4.13 shows the difference in the behaviour of χ'_{ext} and χ'_{in} of the BNCD films when a measurement field of 0.40 A/m was applied.

The results of the χ'_{in} suggest that the samples all go fully superconducting i.e. the samples are able to produce a meissner effect that encompasses their whole volume. If the sample had significant voids or normal material the superconducting grains could not couple together so as to give $\chi_{in} \approx -1$. The issue with this result

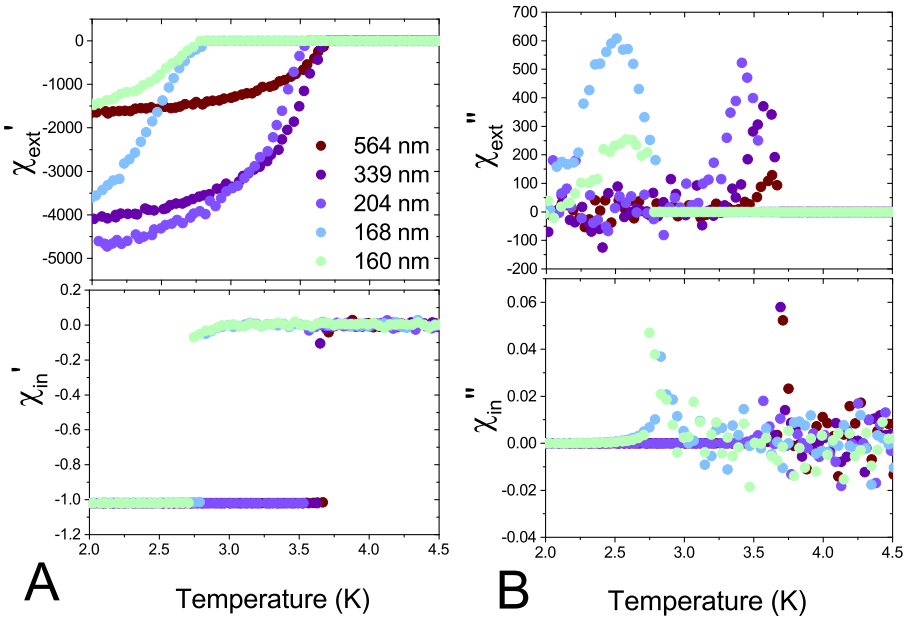

FIGURE 4.13 A) shows a comparison of χ'_{ext} and χ'_{in} versus temperature for the different films with a measurement field of 0.40 A/m. B) shows a comparison of χ'_{ext} and χ'_{in} versus temperature for the different films with a measurement field of 0.40 A/m. The insert comparing colour to thickness applies to all graphs.

is that the transition becomes immediate and loses all detail. This does not make sense when compared with the original result of χ'_{ext}. The results here show that the transition clearly continues pass this initial result. This becomes more apparent in panel B looking at the difference between χ'_{ext} and χ'_{in}. The detail in the AC losses reduces completely. As stated earlier the demagnetization factor only works for homogeneously magnetized ellipsoids with linear magnetic response (105). The granular effect of the films which is present and shown as the AC losses is clearly lost when applying this factor. These results show that application of a demagnetization factor is too simplistic for BNCD films; resulting in an unrealistic transition and loss of information in the χ''_{in} data particularly.

Whilst this detail has been lost it does not mean the percent of superconducting material is not 100. The final result of the transition is still $\chi'_{in} \approx -1$, only the detail is lost and the transition width suppressed. In order to make the J_C calculations, which require the transition detail, it was assumed that the film is fully superconducting. Therefore the external susceptibility was normalised so that $\chi' = -1$. This follows the decision made by Herzog *et al*, who also normalize their external susceptibility assuming ideal conditions before comparing their results to the theoretical values of the Brandt model. If the BNCD films are not fully superconducting this will become evident in the comparison in the next section.

4.3.2 CRITICAL CURRENT DENSITY

Figure 4.14 shows the coles-coles plot for the thickest film substrate and the susceptibilities for the different applied fields. The signal does not follow the theoretical values predicted by the Brandt model; although as the applied field increases it looks like the results are aligning more with the model. As was previously discussed in the method section of this chapter the peak of χ'' does increase with applied field, see figure 4.8. It does not appear to have reached a saturation value yet though. If films are following this model then applying higher fields to this sample for comparison would produce the expected results. It is also possible that the sample is not fully superconducting and that this manipulation of the data is incorrect. The data also appears to be following the model in the range $-0.2 \leq \chi' \leq 0$ unlike the samples discussed in ref. (107). Probably the result of using a smaller field and therefore J_C shows less variation with these applied fields.

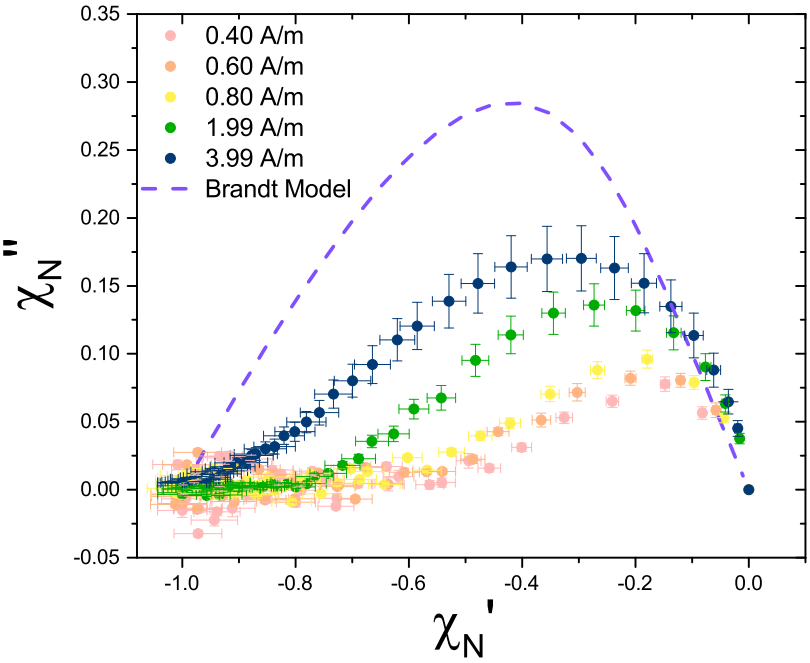

FIGURE 4.14 Coles-coles plot of the BNCD film with thickness 564 nm. The insert shows the different applied films. The error bars have been calculated by error propagation from the standard error of the measured magnetic moment and the volume.

As has been discussed ideally if the samples are identical aside from the thickness and grain size then J_C ought to increase as the films thickness decreases. This is

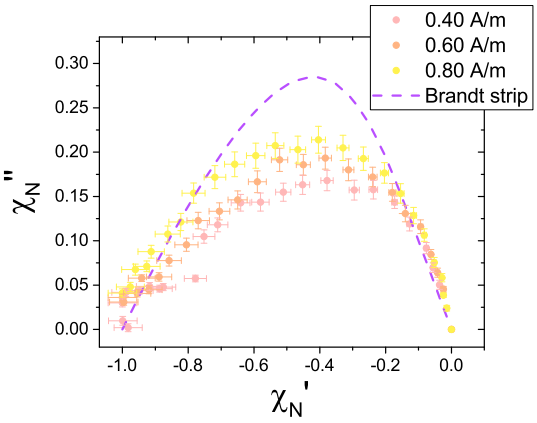

FIGURE 4.15 Coles-coles plot of the BNCD film with thickness 168 nm. The insert shows the different applied fields.

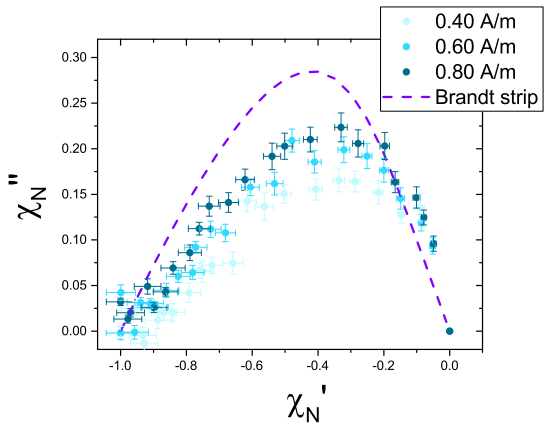

FIGURE 4.16 Coles-coles plot of the BNCD film with thickness 160 nm. The insert shows the different applied fields.

due to the grains decreasing and the number of pinning centres increasing. If this is the case then for the same field strengths application of the model and process to the data ought to produce a better fit to the models. Figure 4.15 and figure 4.16 show the coles-coles plots of the two thinnest films as the data did begin to start following the model more closely. The two highest fields for each of these has been ignored because a full transition is not observed and therefore the susceptibilities can not be normalised. Figure 4.15 for the film with a thickness of 168 nm follows the theoretical values from the Brandt model the best of all the films. Although there is some clear variation between films that are only 8 nm different that seems unusual.

Following the method set out in the J_C calculation section; the data for the 168 nm thick film and the applied fields 0.60 and 0.80 A/m, which best follow the theoretical values, were fitted to determine their peaks. The 0.60 A/m data set was fitted with a spline however the 0.80 A/m set was fitted with a cubic polynomial. This was to correct for an outlier in the data set, whose presence when spline fitting found the peak at a point that did not fit the data trend. This fitting can be seen in 4.17. Having determined the values of χ'' and χ' at the peak h was calculated using (4.11) and (4.12). Using this h and (4.13) values of J_C for each value of $H_{applied}$. J_C is $390 \pm 45\ A/cm^2$ and $580 \pm 90\ A/cm^2$ for 0.60 A/m and 0.80 A/m respectively. Given the few numbers of data points, there is little point in scaling this behaviour with the field. These initial values are an order of magnitude lower than published values J_C values for BNCD films; which give $J_C \sim 10^4 A/cm^2$ (111; 112), although these films have a thickness $\sim 10\mu m$. Considering the peak of χ'' is not yet saturated for these measurements a smaller J_C is not unexpected.

It is clear from these results that higher values are required for further investigation. A repeat set of measurements was performed on the thickest film of the BNCD set; the results can be seen in figure 4:19. The increase in field, as expected, shows an increase in the peak and the shifting of the data to better match the theoretical values. However above 6 A/m the end of the transition shifts below the measured temperature range. The normalization applied to the sample is no longer relevant and the final value of χ'' shifts higher. Figure 4:20 shows a specific set of applied fields from figure 4.19. The data for the fields 4.51, 4.99, 6.01 A/m more closely aligns with the theoretical predictions. 7.00 A/m starts to show an increase from zero in the final value of χ'' with 9.00 A/m being the highest field applied. These measurements do also show the initial expected increase in the peak of χ''. Therefore J_C estimations can be made for some these applied fields. J_C is $770 \pm 90\ A/cm^2$, $860 \pm 95\ A/cm^2$ and $1.13 \pm 0.12 \times 10^3\ A/cm^2$ for 4.51 A/m, 4.99 A/m and 6.01 A/m respectively. Figure 4.18 shows an example of fitting the data measured for an applied field of 6.01 A/m.

The greater alignment with the theoretical predictions with increased field for the thickest film and the increase in alignment witch film decreasing does suggest that the films are fully superconducting.

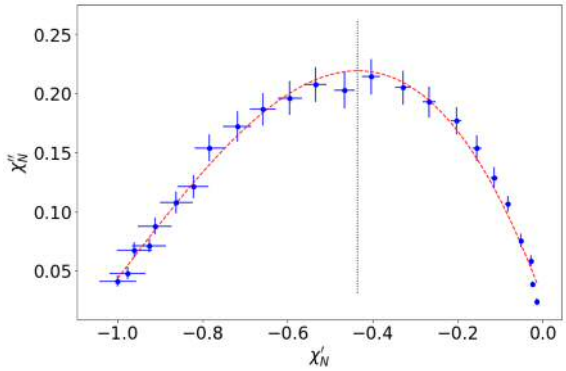

FIGURE 4.17 Example of polynomial fitting to determine the peak for the film with thickness 168 nm when a field of 0.80 A/m is applied.

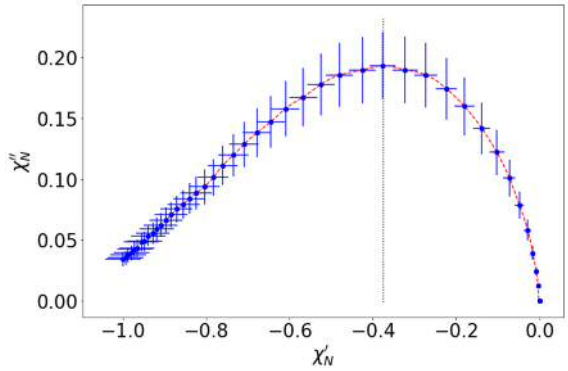

FIGURE 4.18 Example of spline fitting to determine the peak for the film with thickness 564 nm when a field of 6.01 A/m is applied.

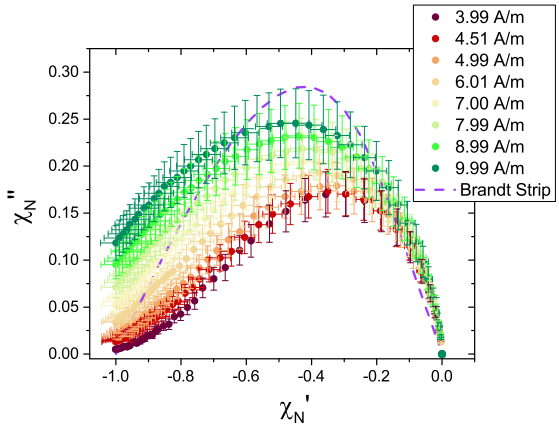

FIGURE 4.19 Coles-coles plot of the BNCD film with thickness 564 nm. The insert shows the different applied fields.

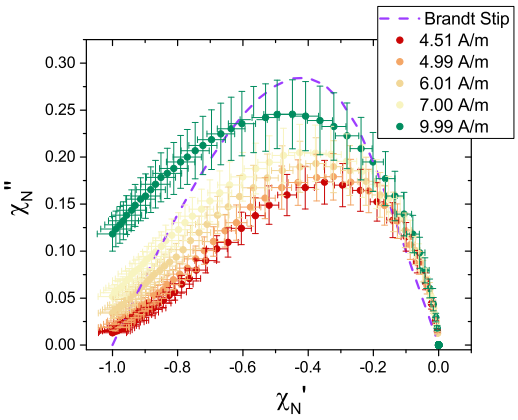

FIGURE 4.20 Coles-coles plot of the BNCD film with thickness 564 nm. The insert shows the different applied fields.

4.4 CONCLUSIONS

4.4.1 CRITICAL TEMPERATURE

The critical temperature of the BNCD films measured by AC susceptibility were found to be noticeably lower than critical temperature onset and offset values determined by resistivity measurements. It has been shown that for BNCD films magnetic measurements are in greater agreement with a T_C defined in relation to the conduction diverging as done by ref.(11).

The AC susceptibility measurements of all the films also do not show two transitions; which would be the result of weak coupling between the grain and grain boundaries (95). The lack of two transitions suggests that the BNCD film grains are coupled strongly enough that this field range can not separate them. Higher applied fields to the thickest sample also did not reveal a second transition.

4.4.2 VOLUME FRACTION AND CRITICAL CURRENT DENSITY

The volume fraction calculations show that the films are made up of a 100% superconducting material. However these results also show an unrealistic transition period, looking more like type I superconductors with no vortex state. This does not mean that the films are not fully superconducting. Using a demagnetization factor to analyse susceptibility requires that the material behaves as a homogeneously magnetized ellipsoid with a linear magnetic response. These three requirements are usually not satisfied by superconductors with vortex pinning (105).

The result of using this method upon the films seems to be the loss of transition detail only. The agreement of the χ' vs χ'' predictions with the ideal theoretical values of the Brandt model also supports this conclusion. The greater alignment with the theoretical predictions with increased field for the thickest film and the increase in alignment with film decreasing does suggest that the films are fully superconducting. The thicker film in particular which was measured with higher fields starts to align more closely with the theoretical values from the Brandt model.

The peak of χ'' however did not reach its saturation point for any of the measured BNCD films. Therefore a true value for J_C could not be calculated for any of these results nor could a comparison be made between the different film thicknesses. J_C could only be successfully calculated for the second thinnest film (168 nm) and the thickest film at higher applied fields. Due to the lack of reaching a saturation value for the peak χ'' these results could only be lower boundary values. This proves true when compared with the literature values for the J_C of BNCD films (111; 112) which are an order of magnitude greater than the values found for two of the films measured in this BNCD set. The thickest films at higher fields having J_C is 770 ± 90 A/cm^2, 860 ± 95 A/cm^2 and $1.13 \pm 0.12 \times 10^3$ A/cm^2 for 4.51 A/m, 4.99 A/m and 6.01 A/m respectively. For the second thinnest; J_C is 390 ± 45 A/cm^2 and 580 ± 90 A/cm^2 for 0.60 A/m and 0.80 A/m respectively. $J_C \sim 10^4 A/cm^2$ having been obtained from (111; 112). Ref. (111; 112) calculated these values from M(H) curves, according to the Bean model. Their results compared against temperature and from fields $0 - 2 \times 10^5$ A/m. The values calculated for the thicker film at higher fields is closer comparatively to these literature values than the thinner film. These films from the initial measurements do appear to be following the Brandt model behaviour.

Chapter 5
Magnetic Relaxation

This chapter concerns the magnetic field dependence of the superconductivity of BNCD films; within is detailed further magnetic relaxation measurements following the initial measurements made in (12). They are evidence in support of a superconducting glass state in the phase diagram. The full work of (12) shows evidence in electrical resistivity measurements and magnetic relaxation measurements.

The thickest film, with a thickness of 564 nm, from the BNCD set is measured in this chapter. It's magnetic relaxation rate is determined at intervals of 0.1 K between the temperatures 1.9K and 3.7 K. The relaxation rates temperature dependence is then compared against other materials relaxation rates. The sample clearly shows magnetic relaxation, which is unsurprising given its granular nature. The first record of this behaviour being explicitly published however is in 2018, in (13). Ref. (13) calculates a pinning potential through resistivity measurements and compares how this varies with magnetic field. The temperature dependence of the relaxation rate for a BNCD film is novel. It also allows for observation of other relaxation rate features typical of a superconducting glass state.

5.1 Introduction to Magnetic Relaxation

As discussed in chapter 2 vortex creep occurs as a result of pinning centres within a sample distorting the vortex lattice. Magnetic relaxation relates to when vortex creep changes the magnetic moment of a sample with time. Thus the measured magnetic relaxation can be thought of as being caused by the spontaneous motion vortices out of their pining sites. Such motion usually arises from thermal activation, but is can also arise from quantum tunnelling or other external activation, such as mechanical vibrations.

The concept of thermal activation causing hopping of vortices or bundles of vortices out of their pinning potential wells was first suggested by Anderson (46) to explain the results of Kim *et al.* (48) on Niobium–zirconium tubes. This section will give a simplified derivation of the key equations for the relaxation rate. First the relaxation rate is presented using a conventional Arrhenius relation. The hopping time t is given in terms of the potential energy barrier height, U the Boltzmann constant k_B and the temperature T:

$$t = t_0 \exp\left(\frac{U}{k_B T}\right) \tag{5.1}$$

The pre-exponent t_0 is the referred to as the "effective" hopping attempt time. Experiments made through extrapolating to $U = 0$ have found t_0 to be in the range $1 - 10$ microseconds (42).

Further insight into the non-equilibrium behavior of pinned vortices comes from considering the force per unit volume exerted by the vortices on each other in a density-gradient configuration. This force, derived by Friedel *et al.* (113), has the following form

$$\mathbf{F} = (1/c)\mathbf{J} \times \mathbf{B} \tag{5.2}$$

where $\mathbf{J}$ is the spatially averaged supercurrent density and $\mathbf{B}$ is the spatially averaged induction field. Its form is similar to the Lorentz force of electrodynamics. Without a pinning force to counter this Lorentz force the vortices will relax to their uniform equilibrium configuration. The current density at which the Lorentz force equals the maximum pinning force determines the critical current density J_C.

Therefore as a result of this U is a decreasing function of J. In a first approximation, the net barrier is reduced linearly with the current J, according to

$$U = U_0\left[1 - J/J_{C0}\right] \tag{5.3}$$

where U_0 is the barrier height in the absence of a driving force, and J_{C0} corresponds to the critical current density required to tilt the barrier to zero in this approximation. Substituting (5.1) into (5.3) and solving for J gives the classic equation of flux creep

$$J = J_{C0}\left[1 - \frac{k_B T}{U_0} \ln\left(\frac{t}{t_0}\right)\right] \tag{5.4}$$

Magnetization is proportional to J according to the Bean's critical state model as discussed in chapter 2. Therefore from (5.4) it is possible see some of

the main features of vortex creep, namely the magnetization is expected to decay logarithmically in time and to drop with temperature. This has been shown to hold true provided that measurement is taken on a sufficiently long time scale. Deviations from logarithmic decay were reported in the initial stages of magnetic relaxation studies on (42; 114). This initial deviation was explained by Gurevich and Küpfer (115) as being due to a transient redistribution of magnetic flux over the sample cross section. The duration of this stage is determined by the sample size, vortex creep rate and the rate of change of the magnetic field. This effect can take between $1 - 100$ seconds after a magnetic field decrease (42). Although, as a result of the measurement set up, up to ten minutes of initial magnetization can be ignored in order to make sure this state has passed (114).

According to (5.4), the relaxation rate depends on the limiting critical current density J_{C0}, the barrier height U_0, and the effective attempt time t_0. To eliminate one or more of these parameters it is convenient to evaluate a normalized relaxation rate $S \equiv (dM/d\ln t)/M$ corresponding to a logarithmic derivative of magnetization versus time. The normalized relaxation rate can be derived directly from (5.4)

$$S \equiv \frac{1}{M}\frac{dM}{d\ln t} = \frac{-k_B T}{U_0 - k_B T \ln(t/t_0)} \tag{5.5}$$

For low temperature superconductors (below 30 K) U_0 dominates and therefore the above becomes

$$S = -\frac{k_B T}{U_0} \tag{5.6}$$

Thus in the Anderson-Kim theory, a measurement of the normalized relaxation rate determines the pinning barrier U_0.

Later versions of the theory expanded upon (5.3) and considered non-linear $U(J)$ dependencies. The full impact of which only became apparent after the development of the vortex-glass (116) and collective-creep theories (117). The key result in these theories being that the barrier diverges as the current J approaches zero.

In the vortex-glass model, there are two states that the system can be in and they undergo a thermodynamic phase transition from one to the other. One state is the metastable state created by interactions with the pinning centres and the other vortices; the second state is a "vortex liquid" state, where the vortices are highly mobile. Figure 5.1 shows an example of this type of phase diagram compare with a typical transitions for a type II superconductor.

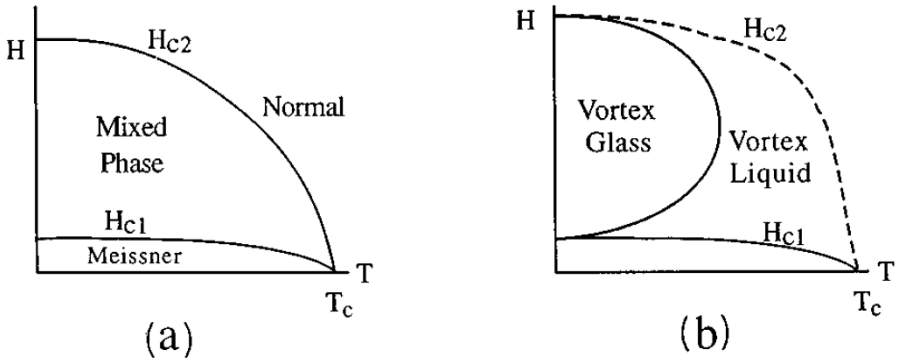

FIGURE 5.1 Magnetic phase diagrams (schematic) for (a) a conventional superconductor, and (b) for high temperature superconductor. Reprinted figure with permission from (42) DOI Copyright (1996) by the American Physical Society.

Collective-creep theory assumes weak random pinning and treats the vortex system as an elastic medium. Contrary to the original vortex creep model, where the volume V of the thermally activated vortices was constant, in the collective-creep model V depends on the current density J and becomes infinitely large for J$\rightarrow$ 0.

Both models have the same equation for $J(T,t)$ despite this different. They also introduce an additional parameter μ which influences S. The calculation of μ varies for each model and can be dependent upon both temperature and field. The calculation of this factor is beyond the scope of this thesis.

To illustrate the differences in the $U(J)$ relation between the three models already discussed, see figure 5.2.

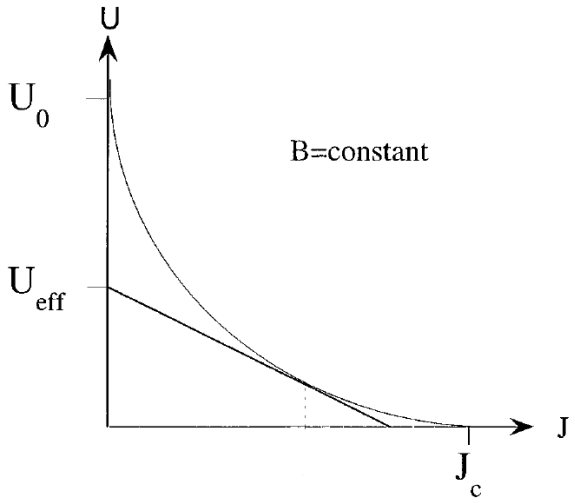

FIGURE 5.2 A schematic illustration of a nonlinear and linear [Eq. (5.3)] functional form of $U(J)$ at a constant magnetic field B. Using (5.3) to determine the pinning barrier yields an apparent value U_{eff} which is smaller than the true pinning potential U_0. Reprinted figure with permission from (42) DOI Copyright (1996) by the American Physical Society.

5.2 EXPERIMENTAL METHOD

5.2.1 EQUIPMENT

The data was taken using the Quantum Design Vibrating Sample Magnetometer (VSM) option for the PPMS, see figure 5.3 for an equipment schematic. The basic measurement is made by oscillating the sample near a detection (pick-up) coil and synchronously detecting the voltage induced. The time-dependent induced voltage is given by the following equation:

$$V_{coil} = \frac{d\phi}{dt} = \left(\frac{d\phi}{dz}\right)\left(\frac{dz}{dt}\right) \tag{5.7}$$

where ϕ is the magnetic flux enclosed by the pick-up coil, z is the vertical position of the sample with respect to the coil, and t is time. For a sinusoidally oscillating sample position, the voltage is based on the following equation:

$$V_{coil} = 2\pi f C m A \sin(2\pi f t) \tag{5.8}$$

where C is a coupling constant, m is the DC magnetic moment of the sample, A is the amplitude of oscillation, and f is the frequency of oscillation. The acquisition of magnetic moment measurements involves measuring the coefficient of the sinusoidal voltage response from the detection coil.

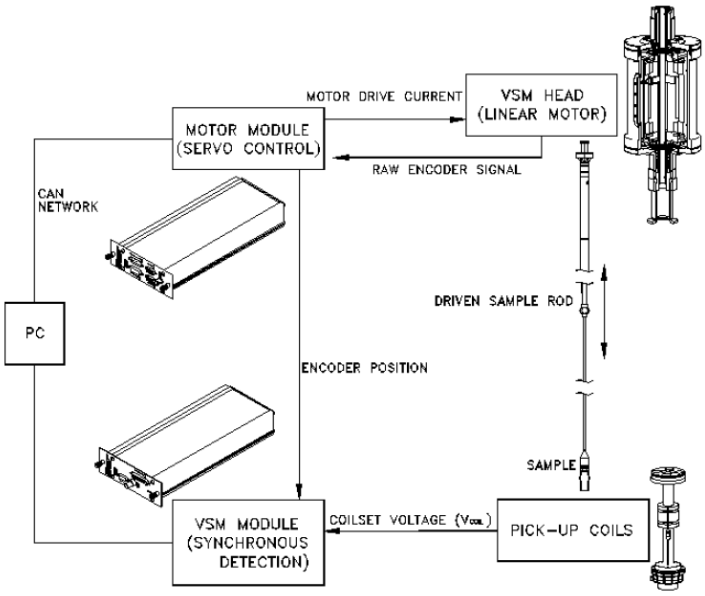

FIGURE 5.3 The sample is attached to the end of a sample rod that is driven sinusoidally. The centre of oscillation is positioned at the vertical centre of a gradiometer pick-up coil. The precise position and amplitude of oscillation is controlled from the VSM motor module. The voltage induced in the pick-up coil is amplified and lock-in detected in the VSM detection module. The VSM detection module uses the position encoder signal as a reference for the synchronous detection. This encoder signal is obtained from the VSM motor module, which interprets the raw encoder signals from the VSM linear motor transport. The VSM detection module detects the in-phase and quadrature-phase signals from the encoder and from the amplified voltage from the pick-up coil. These signals are averaged and sent to the VSM application running on the PC. Reprinted from (118), ©Quantum Design, Inc. 2019.

5.2.2 EXPERIMENTAL PROCESS OVERVIEW

The thickest sample from the BNCD film thickness varying set was chosen to perform this series of magnetic relaxation measurements. It was chosen because it had the highest T_C meaning that using the VSM system the greatest data could be taken across the temperature range available. The magnetic relaxation measurement for this sample follows the procedure recommended by (42), a review covering magnetic relaxation for high temperature superconductors. This process recommends that the sample be cooled to the chosen temperature and then a magnetic hysteresis (MH) loop be measured; from the virgin curve the lower critical field H_{C1}, referred to as the field of minimum magnetization H_m in this paper, is then determined. H_m will be used to describe this field going forward. The first field for full flux penetration, H^*, is approximately $1.5H_m$. The irreversibility field

H_{irr}, above which the magnetization shows reversible behaviour was also determined from the initial MH loops. These values determined the sample can be warmed and then field cooled to the desired measurement temperature. A field H that is smaller than H_{irr} (to allow for magnetic relaxation) but large enough (at least $3H^*$) to ensure full penetration and approximately linear flux profiles must then be applied to the sample. This field is then decreased by a step $2H^*$ and the magnetization (M) measured as a function time (t). S can then be calculated by plotting M against $\ln t$ and using an amended (5.5), $S \equiv (dM/d\ln t)/M_0$, where M_0 is the magnetization at $t = 0$. Then an effective pinning potential can be found using S and (5.6).

The aim of this experiment was to determine $S(T)$. The base temperature of the PPMS is 1.9 K and the T_C onset for this film is, as discussed in chapter 4, ≈ 3.5 K. Therefore the temperature range was chosen as $1.9 - 3.7$ K with measurements at intervals of 0.1 K.

5.2.2.1 MHLOOPS

The initial MH loops to determine H_{irr}, H^* and H_m were taken at 2 K, figure 5.4 shows three test measurements of the virgin curve, which were use to find H_m.

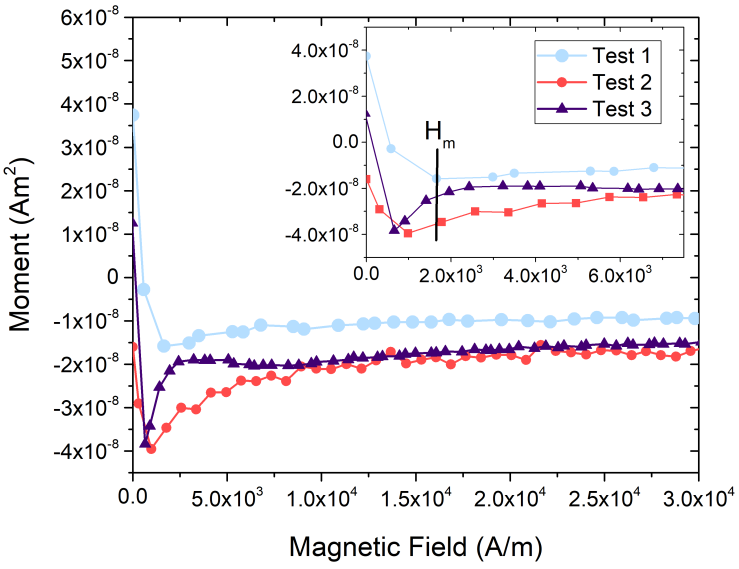

FIGURE 5.4 Plot of the magnetic moment versus the applied magnetic field. The field H_m (the minimum magnetization), is marked on the close up of the measurement data. After this point the magnetic moment noticeably increase for test 2 and test 3, with test 1 increasing only marginally. The variation in tests is a result of adjustments made to the measurement sequence in order to improve the magnetisation curve.

The H_m value was determined to be between $\approx 640 - 1710$ A/m. H^* was calculated using the highest value of H_m, $H^* = 1.5(H_m) \approx 2570$ A/m. H_{irr} is significantly greater than this at $\approx 3.0 \times 10^5$ A/m. The applied field needs to be at least $3H^*$, so the applied field for this measurement was then selected as $4.5 \times (H_m) = 1.5 \times 2570 = 7720$ A/m. This field would be dropped back to 2570 A/m after 10 seconds beginning the magnetization measurement.

The initial MH loops were taken at 2K instead of 1.9 K due to an issue in the sample mounting, it would brush the walls of the coil set, thus leading to chamber warming by 0.1 K. The sample mounting was adjusted allowing for measurements at base temperature. Figure 5.5 shows MH loops at 1.9 K, 2.0 K, 2.5 K and 3.0 K along with a marker showing the initial applied field. The field values chosen when measuring at 2 K produced the needed conditions for magnetic relaxation at the different temperatures so were kept for the rest of the measurement.

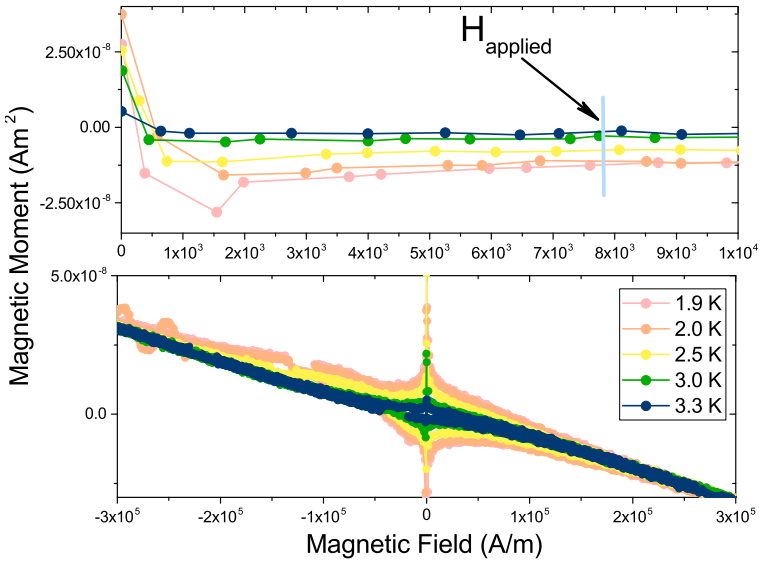

FIGURE 5.5 $H_{applied}$ (initial applied field for measurement) are all marked on the 2 K measurement. These fields for the temperature range keep the sample in the magnetic irreversibility state and so can be applied for all the relaxation measurements.

5.2.2.2 RELAXATION MEASUREMENT

Figure 5.6 shows the behaviour of the temperature and the magnetic field respectively during the first 30 minutes of the magnetic relaxation measurements, the chosen temperature was 2.1 K.

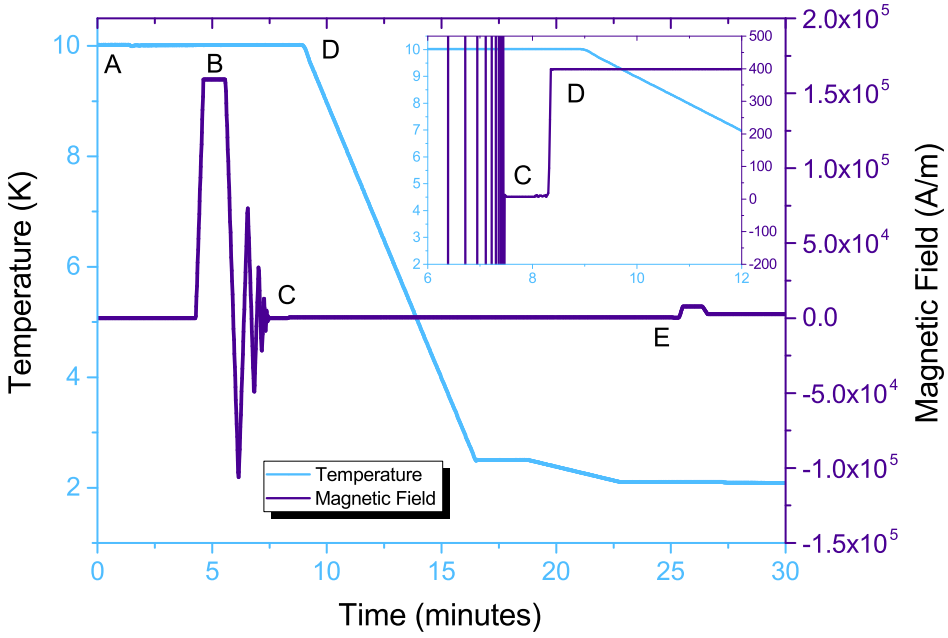

FIGURE 5.6 Shows the behaviour of the temperature and the magnetic field respectively during the first thirty minutes of the two hour magnetic relaxation measurement for five repeated cases. A) The sample was warmed to 10 K, well above its critical temperature and centred between the coil sets. B) The magnet was set linearly ramping at 7960 A/m per second to 1.59×10^5 A/m in persistent mode, held for 10 seconds and then oscillated back down to 0 A/m at 7960 A/m per second; this was performed in order to minimise any remnant field in the magnet. C) The field was set to 400 A/m in persistent mode at a rate of at 400 A/m per second. D) The sample was cooled from 10 K to 2.5 K at 1.0 K per minute and then cooled to 2.1 K at 0.1 K per minute. E) A persistent field of 7720 A/m was applied linearly to the sample, ramp rate 800 A/m per second, for 10 seconds. The field was then linearly dropped at a rate of 400 A/m per second to 2570 A/m. The VSM module then begins measuring the moment 10 seconds after the field has stabilised at 2570 A/m.

The full measurement lasts two hours; five test measurements were performed in order to ensure accurate relaxation rate measurements and these lasted one hour. These measurements will be discussed further in the next section, figure 5.6 still applies to the 30 minutes. The markers A, B and C correspond to different actions performed before measuring in order to ensure consistency.

Firstly at stage A the chamber was set to 10 K, well above the sample's T_C, in order to 'reset' the measurement and the sample was then centred between the coil sets to optimise the measurement of the moment.

At stage B the magnet was then set linearly ramping at 7960 A/m per second to 1.59×10^5 A/m in persistent mode, held for 10 seconds and then oscillated

back down to 0 A/m at 7960 A/m per second; this was performed in order to make sure there was no magnetic flux trapped within the magnet. The field reported by the PPMS comes from considering the current passing through the magnet circuit, the field being a function of said current. The current is determined by the potential drop over a calibrated resistor (119). The output field does not take into account any background sources or remnant field in the magnet. Stage B aims to minimise any remanence by applying a relatively high field and then oscillating this back to zero.

Stage B did minimise these background effects however the final field after stage completion whilst small was not consistent after each repetition. Stage C dealt with this variation by applying a persistent field of 400 A/m, linearly ramped at 400 A/m per second, during the cooling of the sample from 10 K to 2.1 K.

Stage D indicates when the sample began cooling from 10 K down to 2.1 K. The cooling was done in two stages, 10 K to 2.5 K at a rate of 1 K per minute and then 2.5 K to 2.1 K at a rate of 0.1 K per minute.

At Stage E the sample is set up for measuring magnetic relaxation after a step down in the external field. A linear persistent field of 7720 A/m was then applied to the sample for ten seconds, at a ramping rate of 800 A/m per second. This was linearly ramped down at a rate of 400 A/m per second to a persistent field of 2570 A/m. The VSM module then begins measuring the moment 10 seconds after the field has stabilised at 2570 A/m.

5.2.2.3 DEFINING THE RELAXATION STARTING POINT

In order to achieve consistency between each measurement a comparison was made between five magnetic relaxation measurements taken at 2.1 K. This task was performed in order to determine when the measurement started compared to when the magnetic relaxation of the sample began. The moment the field is dropped, in this case from 7720 A/m to 2570 A/m, the sample enters the meta stable state which it can then relax out of. As discussed previously this measurement is taken over a long time scale, the aim being to find S during the logarithmic decay. A measurement time of two hours was chosen to ensure data quality. The following section discusses the five comparison measurements and the selection of the initial time stamp ($t = 0$) for this set up.

Figure 5.7 shows a close up of stage E from figure 5.6, the crosses on the graph indicate when the VSM begins taking measurements. The x axis which represents measurement time has the zero point as when the system is stable at 10K.

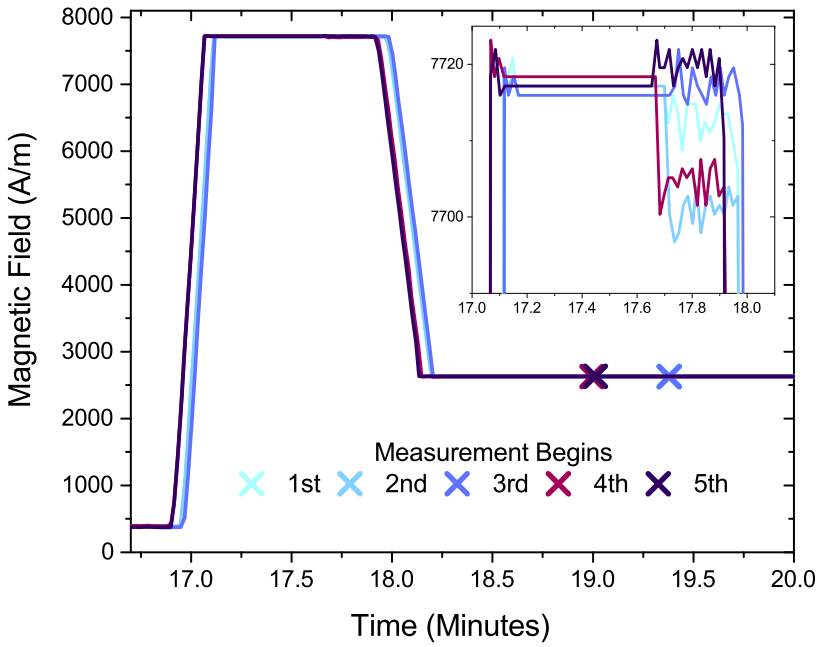

FIGURE 5.7 A close up of stage E from figure 5.6, the crosses indicate the point when the VSM module begins measuring the magnetic moment. The insert shows a close up of the magnetic fields behaviour when 7720 A/m is applied to the sample. This clearly shows the variation in the starting points when the time axis zero point is set to when the sequence starts.

Although the sequence used is nominally identical it is clear there was some variation with when the measurement began.

Now the difference in measurement starting time might be the result of ramp rate variations. The insert of figure 5.7 shows that the time when the magnetic field begins to drop varies for each measurement; which is likely influencing the measurements' start times. There could also be other delays in the system measurement that have led to the time difference.

As stated the relaxation process begins when 7720 A/m starts to drop. As already discussed, the magnetic field starts varying a few seconds before dropping. Therefore figure 5.8 sets $t = 0$ at the last stable point of each measurements' magnetic field at 7720 A/m, before it starts decreasing.

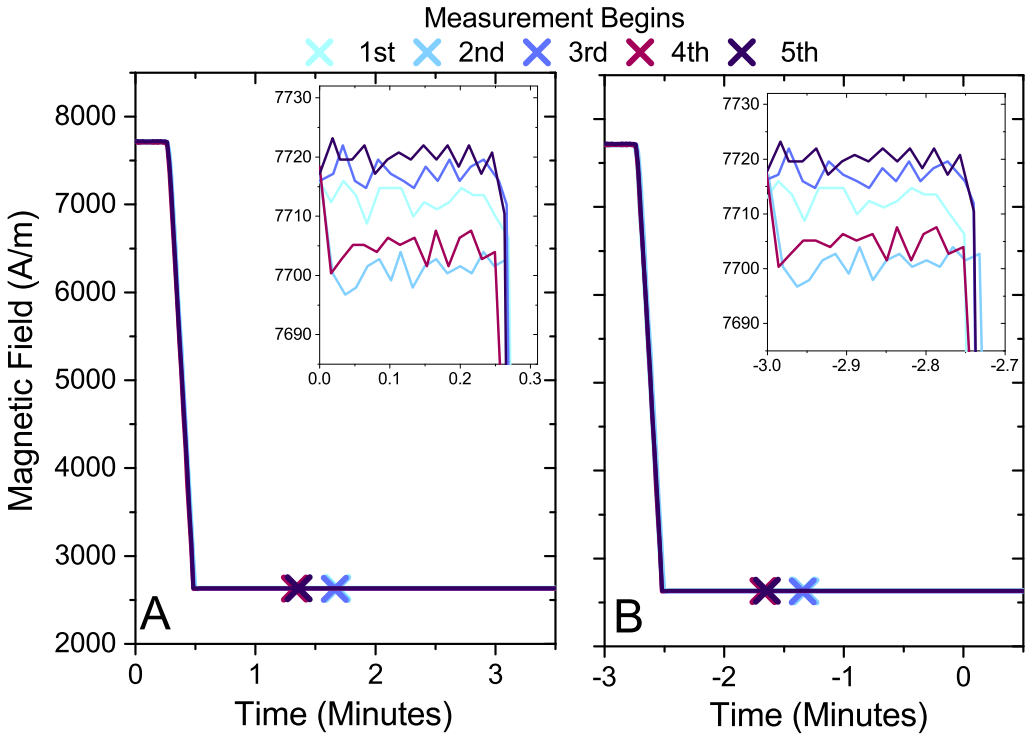

FIGURE 5.8 Graph A shows an adjusted figure 5.7 with the zero point in the minute axis set to the last stable point before the field begins to vary and then drop. There is a twenty second time variation in the starting point of the measurement. Graph B adjusts the zero mark to three minutes after the last stable point before the field begins to vary and then drop.

Figure 5.8 graph A shows the behaviour of the magnetic field for the five measurements with the reset time axis, t_0 being the last stable point before the field begins to vary and then drop. This reset shows that a ramping rate variation can not be the cause of the measurement start time difference. The field reaches 2570 A/m for all the films at approximately 30 seconds after $t = 0$. The measurement variation after this time reset is still evident with two measurements starting 20 twenty seconds after the other three. To account for this difference $t = 0$ will need to be defined as at least 2 minutes after this zero point. Ideally the best time to define $t = 0$ would be 3 minutes after the last stable point of 7720 A/m. This physically accounts for the magnetic field change, ignores 100 seconds of transient phase and gives the same start time for all the measurements. These changes are marked in an adjusted graph B of figure 5.8.

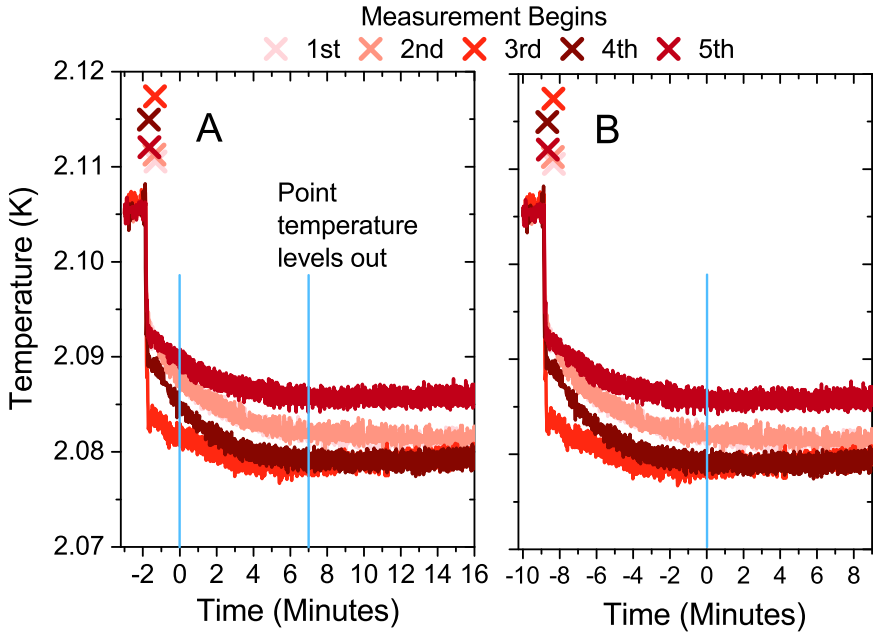

FIGURE 5.9 Graph A shows the change in temperature that happens for all five data sets after the measurement begins. The zero mark is the same as when it was set in figure 5.7. The temperature shift appears to level out after the first sevens minutes of the experiment. Therefore graph B shifts zero mark to this new point.

An additional issue that needs to be accounted for is that when the measurement begins there is a sudden drop and drift in the temperature, see figure 5.9. Whilst the change in temperature is minor the change appears to level at around seven minutes after the previously defined zero mark. Therefore in order to account for this shift $t = 0$ was shifted to this time stamp. Seven minutes is not an atypical amount of initial time to ignore when taking magnetic relaxation measurement (114). Having established a starting point and explained the measurement process the relaxation rate of the five test measurements can be calculated.

5.2.2.4 CALCULATING S

After defining the initial time for the measurement the appropriate magnetic moment data can be used to calculate the magnetization. The changing magnetization is then plotted against $\ln t$, where t is the time measured in seconds. Figure 5.10 is an example of the changing magnetization data versus $\ln t$. The gradient of the slope of the data and it's standard error were calculated using a linear polynomial fit, also shown. This gradient and standard error were then normalized by the initial magnetization to obtain S and its standard error.

Figure 5.11 shows the S and standard error for the five test measurements.

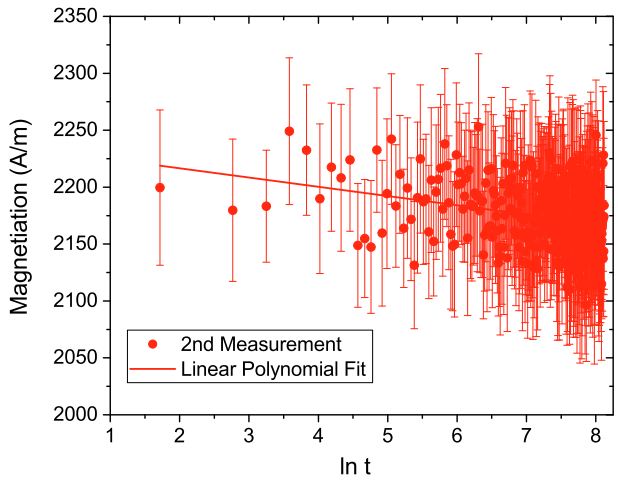

FIGURE 5.10 Example of of the relaxation rate measurement. The gradient of the slope of the data and it's standard error were calculated using a linear polynomial fit. This gradient and standard error were then normalized by the initial magnetization to obtain S and its standard error.

There is clearly some variation but it is possible to fit a horizontal straight line through the majority of the data when considering the standard error; showing that a repeatable value of S can be achieved by this setup. Therefore $t = 0$ is defined for further measurements as *10 minutes after the last stable point of the magnetic field at 7720 A/m*.

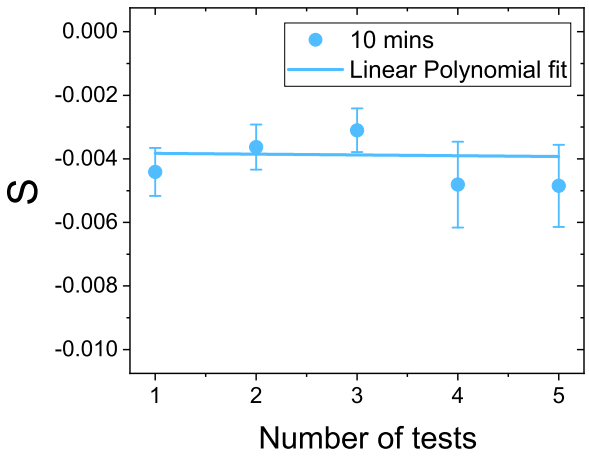

FIGURE 5.11 S and standard error for the five test measurements. It is possible to fit a horizontal straight line through the majority data when considering the standard error; showing that this setup gives a repeatable S result.

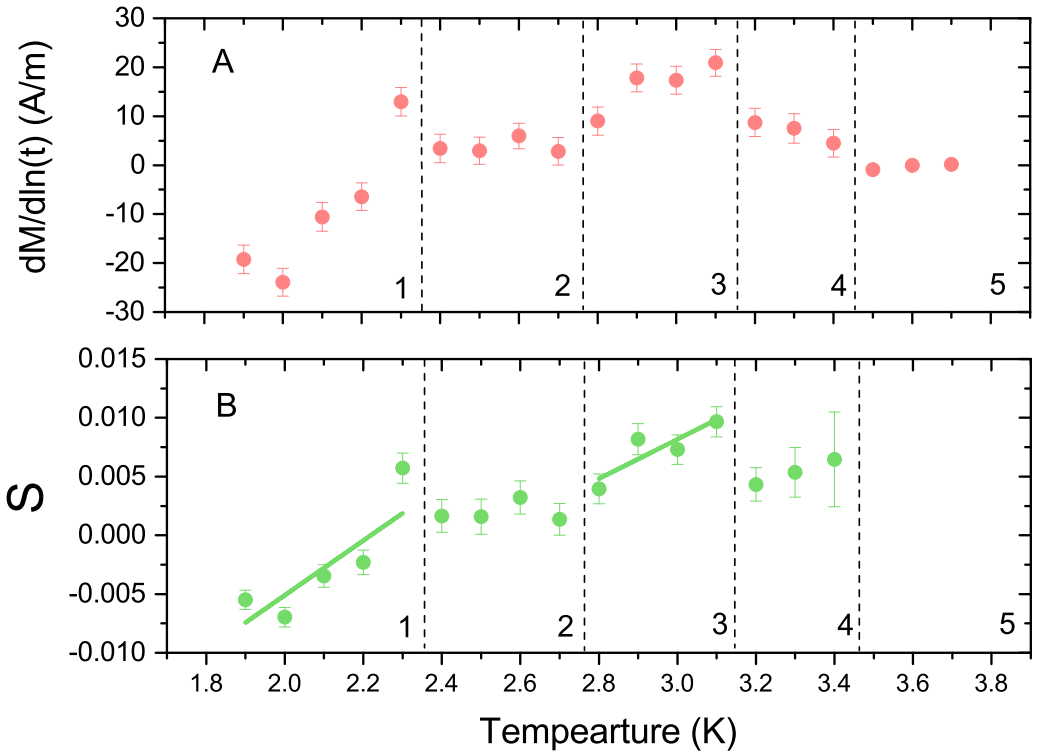

FIGURE 5.12 Relaxation Rates. A) shows the $dM/d\ln t$ and its standard error against temperature whereas B) shows these same values normalized. A) is included to show why the values from section 5 have not been plotted as of course no relaxation is detected above the T_C. Both graphs have been divided into five sections due to the different features.

5.3 RESULTS AND DISCUSSION

5.3.1 TEMPERATURE DEPENDENCY OF THE RELAXATION RATE

Figure 5.12 shows both $dM/d\ln t$ (fig 5.12 A) and S (fig 5.12 B) for the film at different temperatures. The graphs in figure 5.12 have been divided into five different sections which show different features. Section 1 shows a negative S which is very loosely linear. The result looks loosely linear so an effective pining potential using (5.6) can be calculated, a result of 3.7 ± 1.4meV is found. This is one order of magnitude smaller than values calculated for high temperature superconductors which are typically of the order 10 meV (42). This value in Kelvin is $\approx 40 \pm 16$ K.

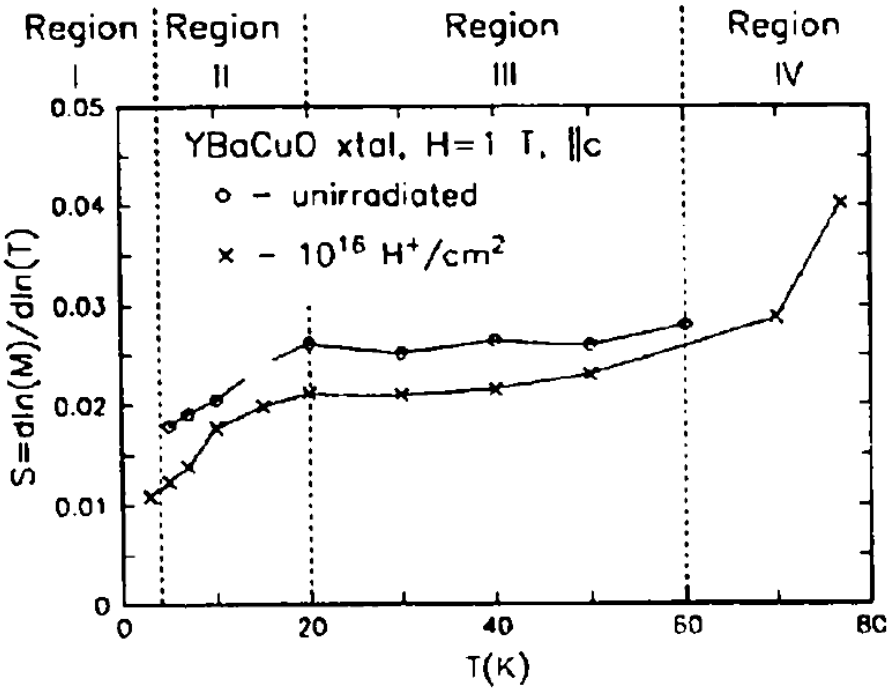

FIGURE 5.13 Normalized magnetic relaxation rate S vs. temperature T for a fully oxygenated YBCO crystal, unirradiated and proton-irradiated. Dashed lines delineate different regions of relaxation behaviour. Reprinted from (120) DOI, Copyright (1991), with permission from Elsevier.

Section 2 shows a common feature from vortex creep and collective creep theories. This plateau arises in the intermediate temperature range. It is present in a number of studies on YBCO materials and has been confirmed in a variety of samples of other samples including BSCCO crystals and polycrystalline TBCCO (42). An example of such can be seen in figure 5.13 from (120), region III. The two curves in figure 5.13 represent the results before and after irradiation with 3 MeV protons to introduce additional pinning centers. The results show a curve upwards before plateauing in the temperature range 20 K to 40 K. In YBCO studies this plateau falls into a specific narrow S range, $0.02 - 0.04$, which is the same for both crystal and films. Although the plateau value for S has been shown to have some field dependence (42). Vortex glass and collective flux pinning theories both predict this type of plateau although neither explain the field dependence (120; 121). The difference in the models is a result of a non-linear $U(J)$. The relaxation rate predicted for these models takes the form

$$S = k_B T / [U_0 + \mu k_B T \ln (t/t_0)] \tag{5.9}$$

which is obviously different from the Anderson-Kim prediction, Eq. (5.6). Equation (5.9) predicts that the normalized relaxation rate decreases with time. Additionally with increasing temperature, the second term in the denominator dominates U_0, and S approaches the limit (42)

$$S = 1/[\mu \ln t/t_0] \tag{5.10}$$

Unless μ is dependent on T, or t_0 is strongly dependent on T, this formula predicts that S will have a plateau, much as is observed in region III of Fig. 5.13. Its presence in this BNCD film offers an area of potential future study as to its temperature and field dependence. The temperature range of the plateau in the diamond is considerably smaller, at 0.4 K, to YBCO's 20 K.

There is an unusual feature in the crossing of section 2 to section 3. The relaxation rate increasing once more is not atypical for higher temperature superconductors, see again figure 5.12 region IV. This happens when the temperature approaches T_C, where experimental limitations are more severe as a result of the magnetization becoming smaller. Therefore there is uncertainty about whether this rate is increasing, decreasing or maintain the same constant value. This result is particularly unusual in that it is increasing *and* changes sign. This also shows some weakly linear behaviour which allows for the calculation of an effective pinning potential using (5.6). The value here is 5.1 ± 1.9meV , which is within errors of the value calculated for section 1.

Figure 5.14 shows the initial magnetization for each temperature measurement. There is an unexpected bump in the measurement itself which is not present for this film in other magnetic moment versus temperature measurements, see chapter 4. The decay of the magnetization is the important feature here, so the fact the initial magnetization is similar does not mean it is responsible for the plateau, despite this feature encompassing section 2 and 3.

Interestingly together section 3 and 4 of (A) in figure 5.12 look like a peak which can be seen in some high temperature superconductors instead of a plateau (42). Considering the magnetization results it is difficult to determine if this peak is the result of experimental limitations or a feature of BNCD films, or even just this film particularly. The first step towards looking at this would be working out the field dependence of the peak/plateau.

Section 5 of (A) shows the transition from superconducting to normal i.e. the decay goes to zero. Therefore S was not calculated for these values.

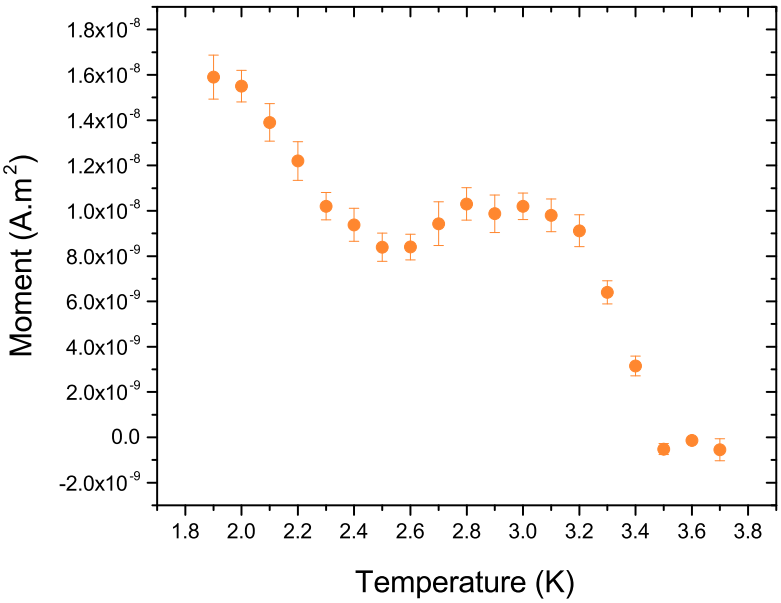

FIGURE 5.14 Showing the initial magnetization for each temperature measurement. There is an unexpected bump in the measurement itself which is not present for this film in other magnetic moment versus field measurements.

5.3.2 COMPARISON WITH OTHER BNCD PINNING POTENTIAL

The pinning potential calculated for this film at $\approx 40 \pm 16$ K and $\approx 60 \pm 22$ K for the two linear regions of the data. Theses are a factor of 2 smaller than the only other published pinning potential available for diamond (13). Their films were granular and grown to 2 and a half times thicker than this film at 1.5 μm. The boron concentrations were varied, the B/C ratios being 7500 ppm, 8750 ppm and 9500 ppm. The ratio used for this film was 12800 ppm which is ≈ 0.68 times greater than these films. The lowest pinning potentials were measured with an applied field of 4.0×10^5 A/m, with values calculated to be 187 K, 280 K, and 313 K for the respective B/C ratios. The pinning potential as has been discussed is dependant upon the critical current density. All of the aforementioned factors influence this value. An intuitive conclusion, which would need to be more rigorously tested, is that a higher boron concentration leads to a lower pinning potential. Although ref. (13) determine their pinning potential value via resistivity measurements which require the use of T_C in the relation:

$$\ln \rho = \ln \rho_{0f} + \frac{U_0}{T_C} - \frac{U_0}{T} \tag{5.11}$$

ref. (13) define T_C as the onset of the decrease in their resistivity, a flawed definition as highlighted chapter 4 when dealing with BNCD films. This method of finding U_0 does not allow for the measurement of the relaxation plateau, so this thesis and ref. (12) currently contain the only measurement of this feature for BNCD films.

5.4 CONCLUSION

The results clearly show magnetic relaxation is present within the sample. The temperature dependency of the S also showed a plateau in its results which is a typical feature that appears in high temperature superconductors. The existence of which is explained by both vortex glass and collective vortex creep models with the relation (5.10). The next step in determining which of the two models applies to diamond would further require field dependent measurements.

An effective pinning potential value of the order of meV was calculated for the linearly changing S of BNCD film. This value is a factor of 2 smaller than the only published value of diamond available (13) and typical high temperature measurements. A variation which could be due to the increase thickness and boron concentrations of the sample grown for ref. (13). Alternatively the variation could be a result of the different measurement processes and ref. (13) not taking account of fluctuations within the film and T_C accordingly.

Chapter 6
Effect of Slurry composition on Chemical Mechanical Polishing of Diamond

As discussed in chapter 3 NCD thin films grown by CVD have an intrinsic surface roughness, which hinders the development and performance of the films' various applications. Traditional methods of diamond polishing are not effective on NCD thin films. Films either shatter due to the combination of wafer bow and high mechanical pressures or produce uneven surfaces, which led to the adaptation of the chemical mechanical polishing (CMP) technique for NCD films. The aim of this final experimental chapter was to gain understanding and improve the chemical mechanical polishing (CMP) technique for NCD films.

Within this chapter the effect of slurry composition and pH upon polishing rates is compared. This was done by polishing a series of NCD thin films for three hours using a Logitech Tribo CMP System in conjunction with a polyester/polyurethane polishing cloth and six different slurries. The reduction in surface roughness was measured hourly using an atomic force microscope. The final surface chemistry was examined using X-ray photoelectron spectroscopy and a scanning electron microscope. It was found that of all the various properties of the slurries, including pH and composition, the particle size was the determining factor for the polishing rate. The smaller particles polishing at a greater rate than the larger ones. This result was published in (14).

6.1 WHY POLISH?

The inherent surface roughness of the BNCD (and NCD) films is an issue for NEMS production because a higher value lowers the Q factor of the device. As the resonators become thinner (or narrower), the surface-to-volume ratio grows. Eventually, the surface properties start to play a significant role in the dissipation, and the bulk properties no longer dominate. If the surface contains a large amount of defects these have been shown to contribute significantly to damping in thin-beam resonators through forming additional energy reservoirs and/or mediating an harmonic mode coupling (1; 122; 123). In the case of SQUIDS a higher surface roughness has been shown to produce a louder noise in its measured signal (124). Significantly reducing this roughness improves the performance of both the NEMS and SQUID. Ideal values for the surface roughness of NEMS being < 2 nm (1).

As the surface roughness is the result of the growth process one method to reduce it is to try to alter this process. For example it is possible to reduce surface roughness by interrupting the crystal growth and limiting the maximum size of the diamond grains. This is done by reducing the H_2 and/or increasing the CH_4 content of the plasma. This unfortunately also leads to an increase in the sp^2 content of the material at the grain boundaries which in turn reduces the Young's modulus (4; 125; 126). Also for films grown under these conditions it is difficult to achieve a roughness lower than 5 nm root mean square (RMS) (127).

Another technique involves etching away the silicon substrate and using the nucleation diamond grains as the surface (128). The surface roughness will be significantly less this side of the diamond film. Unfortunately the quality of this side of the diamond film is inferior to the upper coalesced film with reduced values of Young's modulus and thermal conductivity (128). This technique also requires thick free standing films and complex fabrication processes (128).

Alternatively, surface roughness can be reduced through polishing the as-grown rough NCD thin films. Historically diamond polishing has involved the use of diamond on diamond in a contact mechanical polishing mechanism (129). This process is impractical for NCD thin films because it produces uneven wear rates and the films are susceptible to shattering. The uneven wear rate is a result of the mechanical polishing of diamond being highly dependent upon both the crystallographic orientation of the diamond and azimuthal angle of polishing (130; 131). As stated the surface roughness of NCD thin films is a result of crystallographic orientation growth variation therefore, this type of polishing can lead to protruding crystals left behind on the film surface (132). Potential shattering is the result of the

high pressures typical of mechanical polishing and the characteristic wafer bow of the NCD thin films (133). There is an initial wafer bow always present in the substrate which is then compounded during cooling after CVD growth as a result of the difference in the coefficient of thermal expansion between the diamond film and its non-diamond substrate (134; 135). The bow then places additional stress on the NCD thin film, especially when pushed against planar surfaces, making it more susceptible to damage whilst being subjected to heavy mechanical polishing, see figure 6.1 for a schematic of the wafer bow.

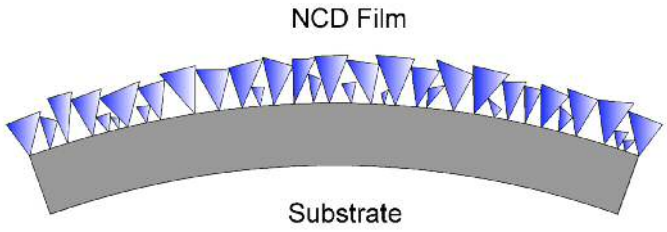

FIGURE 6.1 Exaggerated schematic showing the wafer bow present in the films. Taken from (136).

To overcome these issues, the gentle chemical mechanical polishing (CMP) technique was adapted by Thomas *et al* (136) to apply to diamond. This technique utilises a soft polyester based pad as the polishing base and a silica based colloid as the polishing slurry at room temperature. It is a commonly used technique in the integrated circuit (IC) fabrication industry for polishing silicon wafers (137) and has been shown to successfully polish both NCD (136) and bulk single crystal diamond (SCD) (138).

In both of the aforementioned studies a basic polishing slurry containing silica (SiO_2) particles was used. In the present study, three different polishing particles, ceria (CeO_2), alumina (Al_2O_3) and silica, all common to the IC fabrication polishing industry, were used to examine how composition affects the polishing rates. For each particle type there was an acidic (pH $\approx$ 6) and a basic (pH $\approx$ 9) slurry. The aim of this study was to compare and contrast the different slurries to better understand how silica, a material with a density 2.4 $\frac{g}{cm^3}$ and a hardness of 7 (139) on the Mohs scale, is able to polish diamond of density 3.52 $\frac{g}{cm^3}$ (140) and hardness 10. (139) The significant difference in hardness and density does not mean polishing is impossible; harder materials can be polished by softer particles for example tantalum by silica (141; 142; 143).

6.2 EXPERIMENTAL PROCEDURE

6.2.1 SLURRIES

The silica polishing slurry was Syton SF-1 Alalkine Colloidal Polishing Slurry from Logitech, which was made acidic in house through the addition of phosphoric acid (H_3PO_4). The alumina particle based polishing slurries were supplied by Saint Gobain, brand names Polycrystalline Alumina Polishing Slurry 9240 and Polycrystalline Alumina Polishing Slurry 9245. Finally, the ceria based polishing slurry was supplied by Eminess, brand name Ultra-Sol Optiq, which arrived basic and was also acidified. Table 6.1 shows a summary of the specific properties of each individual slurry. The particle size and particle content was provided by the slurry manufactures. The particle diameters were also measured using a Malvern Zetasizer Nano Z device using a dynamic light scattering (DLS) technique. To do this the slurries were diluted to a 1/1000 ratio and then measured. pH values of the concentrations used were measured using a Mettler Toledo Fivego pH meter.

TABLE 6.1 Properties of Slurries adapted from (14). Density and hardness values taken from (139). The particle size and particle content were provided by the slurry manufacturers. DLS particle diameters and pH were measured in this work.

Property	Silica	Alumina	Ceria
Density ($\frac{g}{cm^3}$)	2.2 - 2.6	4.0	7.1
Hardness (Mohs)	6-7	9	6
Particle diameter measured using DLS (μm)	0.1 $\pm$ 0.06 (Basic) 0.1 $\pm$ 0.06 (Acidic)	1.0 $\pm$ 0.18 (Basic) 0.2 $\pm$ 0.05 (Acidic)	0.5 $\pm$ 0.17 (Basic) 0.5 $\pm$ 0.19 (Acidic)
Particle size according to Manufacturers (μm)	Not Available	0.4 (Basic) 0.3 (Acidic)	0.4 (Basic) 0.4 (Acidic)
Particle content (%)	15 - 50	20 (Basic) 20 (Acidic)	20 (Basic) 20 (Acidic)
pH of Solution	9.6 5.6	9.1 5.8	8.9 5.8

6.2.1.1 DLS

The principle of dynamic light scattering is that fine particles and molecules that are in constant random thermal motion, Brownian motion, diffuse at a speed related to their size, smaller particles diffusing faster than larger particles and their temperature. The temperature being constant then the diffusion speed can be measured to determine the size. The Malvern Zetasizer Nano Z device measures the diffusion speed by analysing speckle patterns of the sample after it has been illuminated with a laser. The scattering intensity at a specific angle will fluctuate with time, and this is detected using a sensitive avalanche photo diode detector (APD). The intensity changes are analysed with a digital auto correlator which generates a correlation function. This curve can be analysed to give the size and the size distribution, also known as particle count or intensity.

Figure 6.2 shows an example of the DLS output for the basic alumina polishing slurry. Three measurements were taken for each sample and the average is stated as the particle diameter in table 6.1. In order to account for errors in size a Gaussian curve was fitted to the DLS data of each slurry, from this the full width half maximum (FWHM) of each intensity peak was calculated. This was then converted into a standard deviation about the mean average particle size using the relation FWHM = 2.35σ. The standard deviations are included along with the particle diameter in table 6.1.

6.2.2 FILM POLISHING

The details of the films growth can be found in chapter 3, section 3.2.2. The root mean square (RMS) roughness of each film was measured using a Park Systems' Park XE-100 atomic force microscope (AFM) with a Tespa-V2 tip in non-contact mode. The XY spatial resolution was 20 nm and the Z spatial resolution was 0.2 nm. The Parks provided software XEI data processing was used to analyse each AFM image. An average of three 25 μm^2 areas of the as-grown films showed that they all had an approximate RMS average of 25.1 ± 2.7 nm.

The NCD films were polished by CMP using a Logitech Tribo polishing system in conjunction with a SUBA-X polishing pad and the chosen slurry, at intervals of 1 hour for a total of 3 hours. Before use, the polyester polishing pad was conditioned for 30 minutes using an abrasive conditioning chuck, which consists of a nickel plate embedded with diamond grit, and DI H_2O to ensure it had

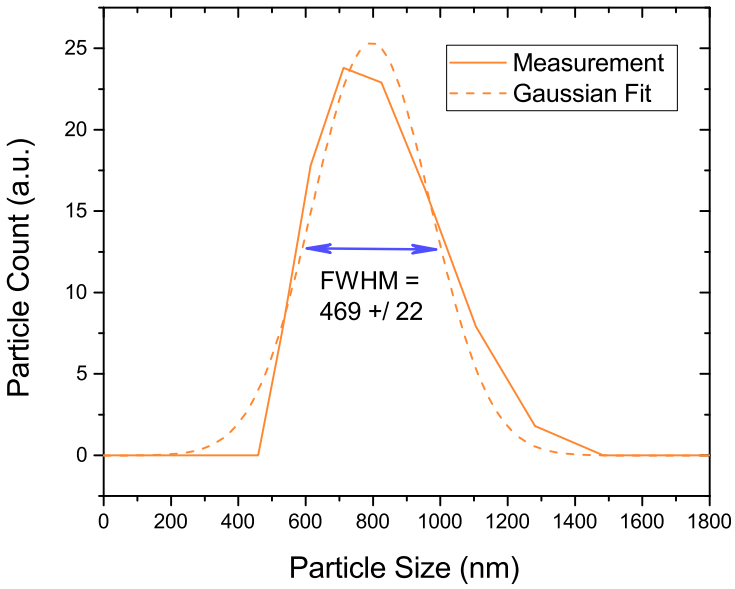

FIGURE 6.2 An example of the DLS particle size measurement for the basic alumina polishing slurry along with a Gaussian curve fitted to the data.

a high surface roughness for maximum polishing action and slurry distribution (144). During film polishing, both the pad and carrier were kept at 60 rpm rotating in opposite directions, while the carrier swept across the pad and a down pressure was kept at 2 psi. A pressure of 20 psi was applied to the back of the wafer in order to crudely flatten NCD film wafer bow. After initial wetting of the plate, the feed slurry rate was kept at 40 ml/min. At hourly intervals the films underwent a clean using the standard SC1 process and their roughness and thickness were measured. A schematic of this process can be seen in figure 6.3.

For comparison of the surface chemistry of each film after the maximum duration of polishing, X-ray photoelectron spectroscopy (XPS) data was taken using a Thermo Scientific^{TM} K-Alpha^{+} spectrometer. XPS is a quantitative spectroscopic technique that measures the elemental composition at the parts per thousand range, empirical formula (simplest positive integer ratio of atoms present in a compound), chemical and electronic state of the elements that exist within the top 0 to 10 nm of the sample. XPS spectra are obtained by irradiating a material with a beam of X-rays while simultaneously measuring the kinetic energy and number of electrons that escape from the measurement region.

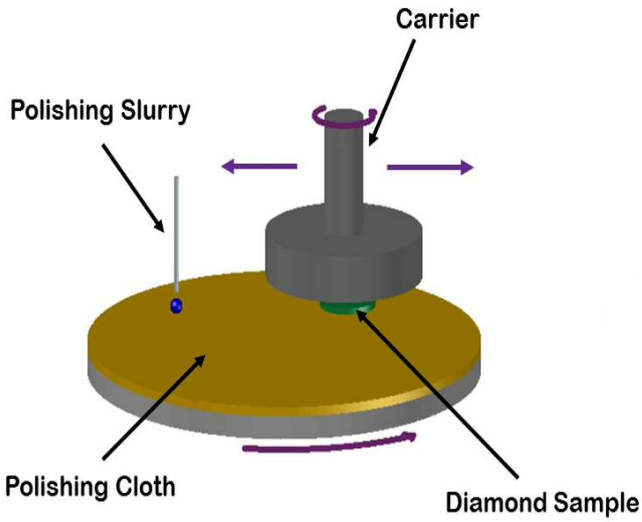

FIGURE 6.3 A schematic of the Logitech Tribo polishing system, the different components are labelled in the figure, taken from (14).

Spectra were acquired using a monochromatic Al source operated at 72 W (6 mA x 12 kV) and at pass energies of 40 and 150 eV for high resolution and survey scans respectively over an analysis area of 400 μm. Charge compensation was achieved using the K-Alpha charge neutralisation system, which employs a combination of both electrons and low energy argon ions. Spectra requiring charge neutralisation were subsequently calibrated to the C(1s) line at 285.0 eV. The results were analysed using the software CasaXPS. SEM images were also taken of the final films using the in-lens detector of a Raith eLine system operated at 10 kV and a working distance of 10 mm.

6.2.3 SUPERCONDUCTIVITY AFTER POLISHING

The effect of CMP upon the superconductivity of a BNCD film was studied in ref. (90). The motivation for this work was to determine whether the CMP processes described previously would significantly affect the superconductivity of the BNCD films. It is well known that some methods of polishing can result in subsurface sample damage that could potentially degrade the superconducting properties (145; 146). For example, Wu *et al.* (147) reported an unexpected loss of superconductivity after mechanical polishing. From the described experiment, it is not clear if the sample no longer showed superconductivity, or if T_C was lowered to a temperature that was simply not achievable with their experimental apparatus. While X-ray diffraction (XRD) revealed no significant structural changes induced by the polishing process, the boron concentration was reported to be reduced by

approximately six times the original value. Though this may suggest an inhomogeneous boron distribution in the sample, the overall conclusion from their work should be that mechanical polishing of BNCD films can have marked effects on the superconducting properties.

The BNCD film, whose growth was described in chapter 3, was polished using the same Logitech Tribo polishing system and polyurethane impregnated polyester felt polishing pad and alkaline colloidal silica polishing slurry described in the previous section. Prior to polishing, the felt pad was conditioned with a chuck embedded with diamond grit for 30 minutes to promote the optimum surface texture. The sample and the polishing pad were rotated in opposite directions at 60 rpm with a down-load of 2 psi, a slurry feed rate of 40 ml/min and a backing pressure of 20 psi was applied to the wafer. During polishing, in situ conditioning was used throughout to maintain the optimal surface texture of the polishing pad. The film was polished intermittently for 14 hours in total with T_C measurements made as the surface roughness decreased.

The T_C measurements of the whole wafer were made by clamping the sample to a variable temperature stage on the cold plate of a pumped liquid 4He cryostat. A diode thermometer and a surface mount heater were glued centrally to the exposed underside of the wafer. A symmetrical jig with a 1 cm^2 arrangement of spring loaded pins was pushed directly onto the film surface and a four-terminal measurement of the film resistance was made using an AVS-47B AC resistance bridge. The results of which can be seen in figure 6.4.

Figure 6.4 shows the resistance measurements for the B-NCD film at varying stages of polishing. The inset shows the variation of normalised resistance with temperature from 1.6 K to room temperature. Focusing on the temperature range below 10 K, the as-grown film had a $T_C = 4.2$ K with a transition width, $\Delta T_C = 0.5$ K. In this work T_C was defined as the midpoint of the transition; which as chapter 4 discusses is not the most accurate method for defining T_C for BNCD films.

Following the first six hours of polishing, T_C is initially reduced by 0.5 K with a corresponding increase in the width of the transition by 0.1 K. The measured resistive T_C then increases until the original value is recovered, though the reason for this is not immediately clear. As can be seen in figure 6.4, a change in the T_C definition would not resolve this issue. It is possible that as material is removed from the surface, some percolative pathways through the film are removed which could lead to a broadening of the transition width. As the film is polished, a

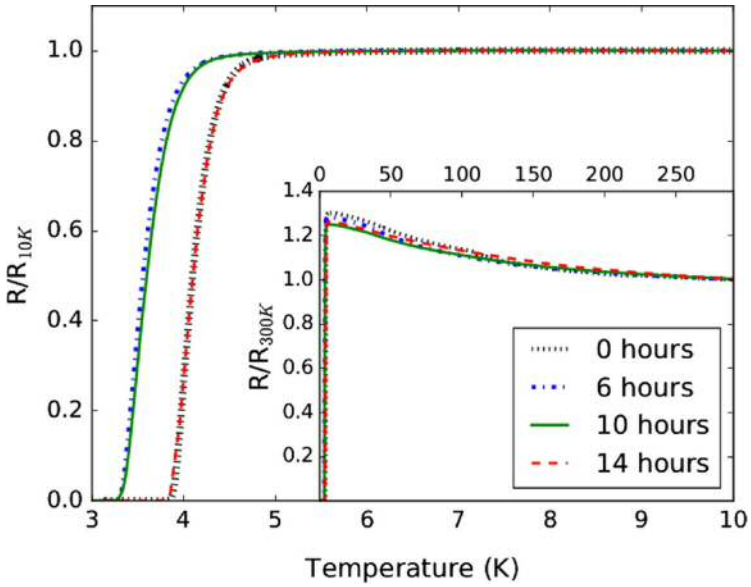

FIGURE 6.4 Resistive superconducting transition of the BNCD film at various stages of polishing. The inset shows the variation of resistance with temperature from 1.6 K to room temperature. The measurement of R(T) for the 14-h polished film is dashed (red) to show that it lies almost exactly on top of the data for the as-grown film (black). Image taken from (90).

reduction in the average grain size could also lead to changes in T_C and ΔT_C (148). Since CMP is a gentle method of polishing involving small mechanical forces, it is not believed that there is any subsurface damage to the film in the same way it is introduced in mechanical polishing. Additionally, the difference could be the result of the experimental set up. The measurement of T_C, in this case, was made by pressing contacts directly onto the surface of an unpatterned 2-inch wafer. Whilst the I-V characteristics of the contacts were checked for linearity at several temperatures, it could not be guaranteed that the contacts were made to identical points on the wafer for each T_C measurement. If there is a local variation in T_C, this could result in small measurable differences.

Following the 14 hours of CMP needed to reduce the surface roughness to < 2 nm RMS, the values of T_C and ΔT_C are unchanged. In figure 6.4, these data are dashed to clearly show that they lie on top of those for the unpolished film. In contrast to the findings of Wu *et al.* (147) that suggest that mechanical polishing can significantly change or even destroy the superconductivity in BNCD films, this work found that CMP does not destroy the superconductivity as measured by the resistive transition temperature.

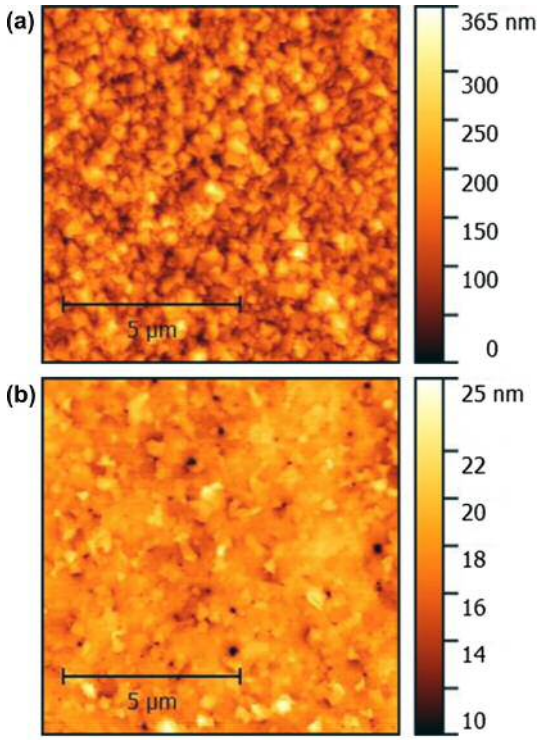

FIGURE 6.5 AFM images for the (a) as grown and (b) post 14 hours of polishing film. Image taken from (90).

Following each polishing step, the film was SC-1 cleaned for 20 min to remove remaining slurry from the surface. The surface morphology at decreasing surface roughness was studied by the same AFM and SEM. Figure 6.5 shows the AFM images before and 14 hours after polishing.

It was demonstrated by Klemencic *et al.* in ref. (90) that the CMP of a BNCD film could be performed without inducing significant changes to its superconducting transition temperature. This result implies that the conclusions of the effect of slurry composition on polishing rate can be applied to the BNCD films as well NCD films, without fear of loss of superconductivity.

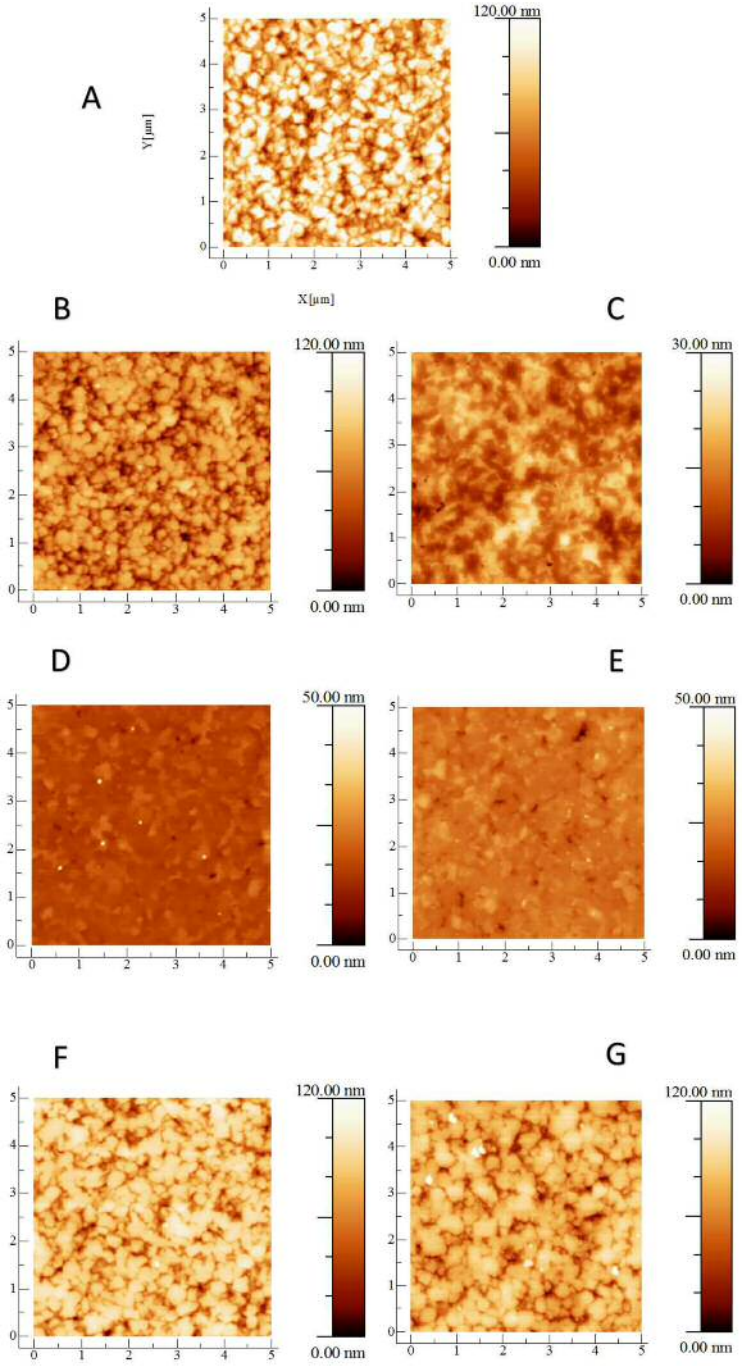

FIGURE 6.6 AFM images of the NCD films taken from (14). A) Shows the as-grown NCD film and is included here for comparison with the polished films. B) NCD film after 3 hours of basic alumina polishing. C) NCD film after 3 hours of acidic alumina polishing. D) NCD film after 3 hours of basic silica polishing. E) NCD film after 3 hours of acidic silica polishing. F) NCD film after 3 hours of basic ceria polishing. G) NCD film after 3 hours of acidic ceria polishing. There is a strong variation in the roughness reduction of each film for the different slurries which will be discussed in greater detail in the next section.

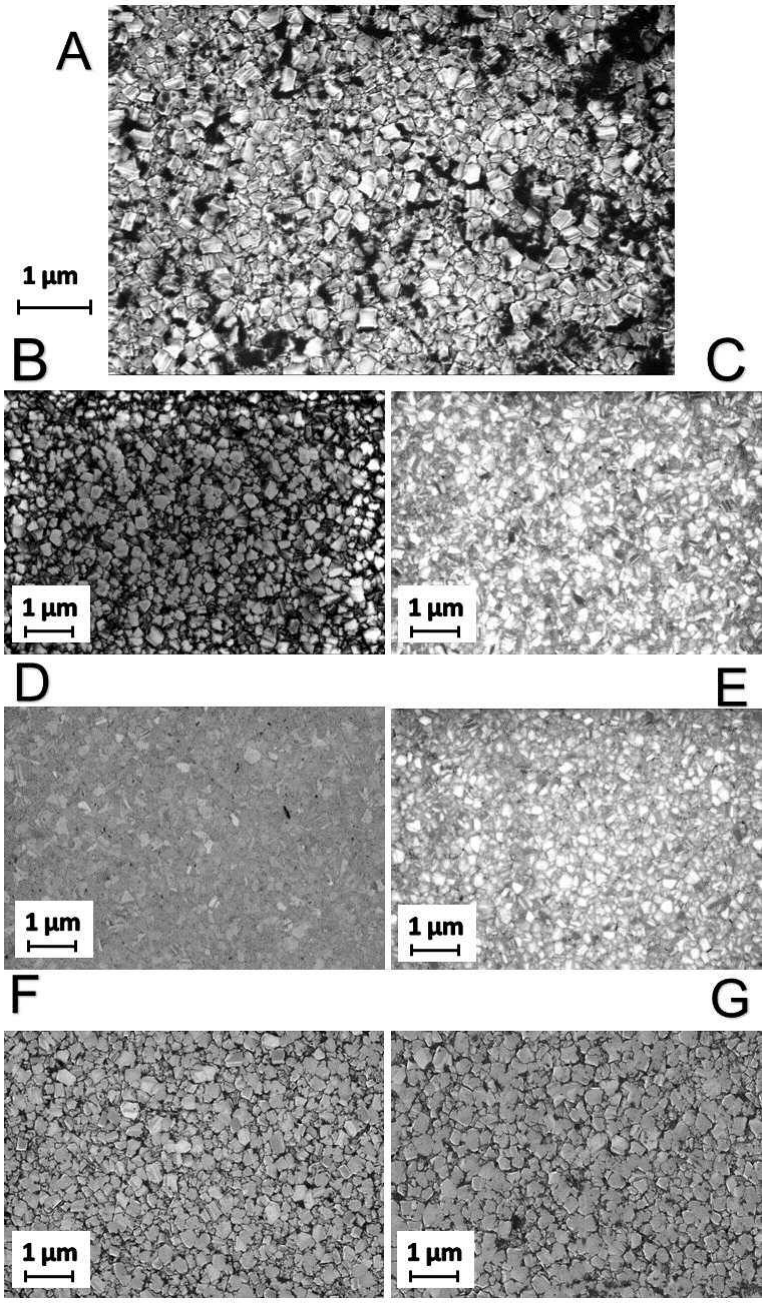

FIGURE 6.7 SEM images of the NCD films taken from (14). A) Shows the as-grown NCD film and is included here for comparison with the polished films. B) NCD film after 3 hours of basic alumina polishing. C) NCD film after 3 hours of acidic alumina polishing. D) NCD film after 3 hours of basic silica polishing. E) NCD film after 3 hours of acidic silica polishing. F) NCD film after 3 hours of basic ceria polishing. G) NCD film after 3 hours of acidic ceria polishing. It is clear just from these images that there is a variation in the roughness reduction of the different slurries, which will be discussed in the next section.

6.3 RESULTS AND DISCUSSION

6.3.1 MORPHOLOGY

Figure 6.6 shows AFM images of seven NCD thin films and figure 6.7 shows SEM images of the same set of films. Image A for each case is the as-grown film and is included in the set for comparison against six polished films. The small white dots on the surface of figure 6.6 D are dust particles; they are only visible because the surface is so smooth that minor particles can be observed as perturbations. Rougher AFM's do not show these dots due to tip convolution and the dust particles being very small compared to surface roughness. The dust particles are few in number and sufficiently minor that they are unlikely to significantly the effect the AFM measurement. If they were any other type of defect on the surface they would have appeared on the SEM image of the same sample, as can be seen from Figure 6.7 D they do not. It clear just from these images that there is a significant variation in the roughness reduction of the different slurries. The measured roughness from the AFM measurements will be discussed in due course however observations can be made simply from looking at SEM and AFM images. The surface of the NCD thin film polished by basic silica (D) and the surface of the NCD thin film polished by acidic silica (E) are significantly smoother than the as-grown film (A). Whereas the surface polished by basic ceria (F) and the surface polished by acidic ceria (G) appears similar to the as-grown film. Interestingly the surface polished by basic alumina looks similar to the surfaces polished by ceria (G and F), whilst the surface polished by acidic alumina (C) is smoother than these but not as smooth as the silica-polished surfaces (D and E). This can be seen from both the AFM and SEM images.

Figure 6.8 graphically shows the reduction in the RMS roughness of each film after each hour of polishing up to a total of 3 hours. The average RMS of three 25 μm^2 areas of each polished film is plotted with their respective standard deviation. Figure 6.9 shows the corresponding thickness reduction. For those slurries that polished with the greater rate there is also a corresponding greater reduction in the thickness of the diamond. This is to be expected as the polishing is removing the roughness layer in order to produce a more uniform film. The zero mark for each graph being the roughness and thickness respectively of the as-grown diamond film. Only three hours of polishing were performed for this study because wear rate was seen to drop significantly after the first hour and an observable difference in polishing was recorded within this time period.

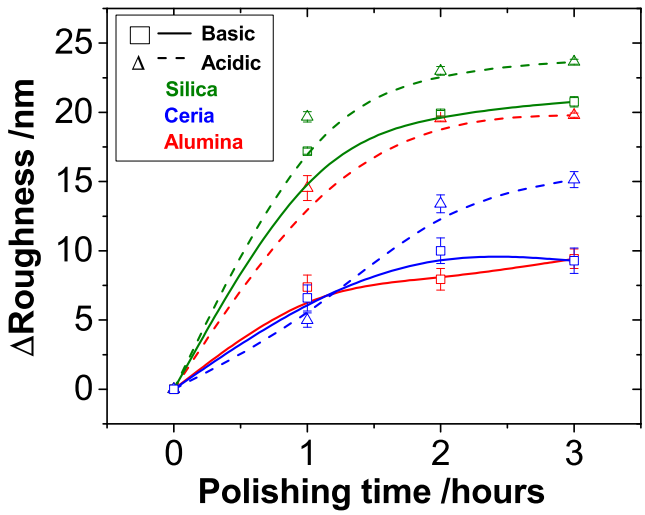

FIGURE 6.8 The reduction in the RMS roughness of each film after each hour of polishing up to a total of 3 hours taken from from (14). The average RMS of three 25 μm^2 areas of each polished film is plotted with their respective standard deviation. The zero mark being the roughness of the as-grown diamond film.

It can be clearly seen in figure 6.8 that regardless of particle type, the acidic slurry always leads to a greater RMS roughness reduction compared to its basic counterpart. However, the variation between basic and acidic is inconsistent between particles. In the 3 hours the acidic silica polishing slurry reduced the surface roughness by 23.7 $\pm$ 0.4 nm, the basic version of this slurry reduced surface roughness in the same time by 20.8 $\pm$ 0.6 nm. Whilst not within errors this is at most a difference of 3.8 nm. In contrast, the alumina particles show a difference of 10.4 $\pm$ 1.0 nm. The ceria particles show 5.8 $\pm$ 1.1 nm. This particle inconsistency shows that the pH alone cannot be a deciding polishing factor.

A comparison of the results considering only the particle composition shows that the silica particles polish at greater rates than the ceria particles but there is an inconsistency here with the alumina slurries. The acidic alumina polishes at a rate similar to the silica but the basic alumina at a rate comparable to ceria. This large variation between the alumina slurries means particle composition, and therefore their particles properties such as Mohs hardness and density, is not the only deciding polishing factor.

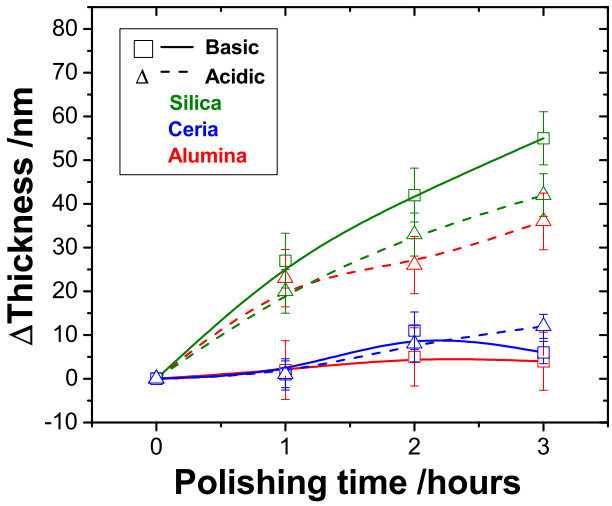

FIGURE 6.9 The change in the thickness of the NCD films during the three hours of polishing taken from from (14). The zero mark being the thickness of the as-grown diamond film. For those slurries that polished with the greater rate, see figure 6.8, there is also a corresponding greater reduction in the thickness of the diamond. This is to be expected as the polishing removes the diamond peaks.

Comparing figure 6.8 with the other known slurry properties in table 6.1, a relationship between polishing rate and particle size is revealed. Figure 6.10 plots the diameter of the respective particles and their standard deviation, as measured by DLS, against the change in roughness after 2 hours of polishing. There is a clear correlation between the diameter and rate, with the smaller particles polishing faster than the larger particles. The faster rate is most likely due to an increase in contact area as a result of the use of smaller sized particles. The particle content % of the slurries is within an order of magnitude of each other, this means those slurries with smaller particles will also contain a greater number of said particles.

6.3.2 X-RAY PHOTOELECTRON SPECTROSCOPY

XPS was taken of the six polished films and an as-grown film in order to compare the surface chemistry before and after polishing. The aim being to observe if the components from the slurry were bonding to the surface to facilitate CMP. The dust particles previously noticed by the AFM are highly unlikely to be the components of the slurries (ceria, silica or alumina) so there was no concern regarding contamination of the XPS data. The results of which are displayed in figure 6.11.

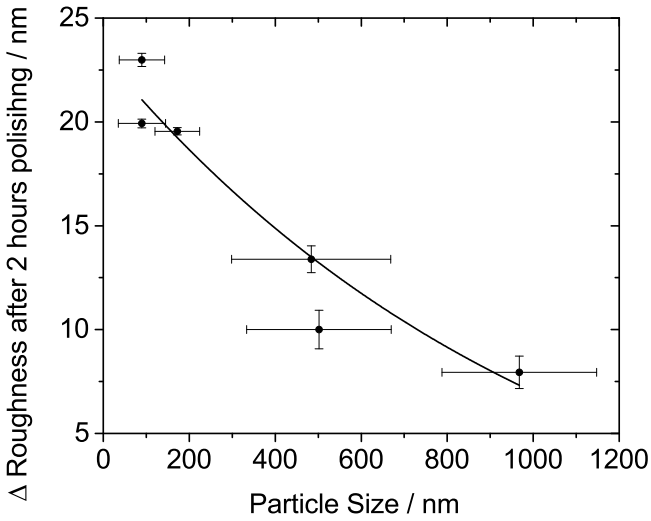

FIGURE 6.10 Change in the RMS roughness after 2 hours polishing compared against the size of the polishing particles and their respective standard deviation, measured by DLS. Image taken from from (14). There is a clear correlation between particle size and rate. Smaller particles, with a diameter less than 200 nm, polish NCD thin films at a greater rate than the larger ones, with a diameter greater than 500 nm.

Panel A shows that the only NCD thin films whose surface chemistry significantly changed were those polished by the ceria particle slurries. In the case of these two films, ceria particles remained bonded to the surface, detected around 900 eV, even after cleaning using the standard SC1 process. There was a very weak Al_2 signal on the film that was polished using the basic alumina slurry but not for the acidic alumina. It is possible that the cleaning removed any trace of the Al and Si that was previously bonded to the surface.

Panel B depicts only the O1s signal of the surface; a sweep of binding energy from 520 eV up to 550 eV. The major peak at 532 eV corresponds to the C-O bond. A second peak can be observed at 530 eV corresponding to the Ce-O bond. Panel B shows that aside from ceria there is no other change to the type of oxygen bonds present on the surface. Panel C shows only the C1s signal with a sweep from 280 eV to 300 eV. Only the C-C bond is present with no other change observed before and after polishing.

Table 6.2 shows the O1s/C1s ratio for the unpolished film and the six polished films. Comparing these values shows how the oxygen environment relative to the carbon environment has changed after polishing. For all the films polished there was an increase in the oxygen environment on the surface implying the

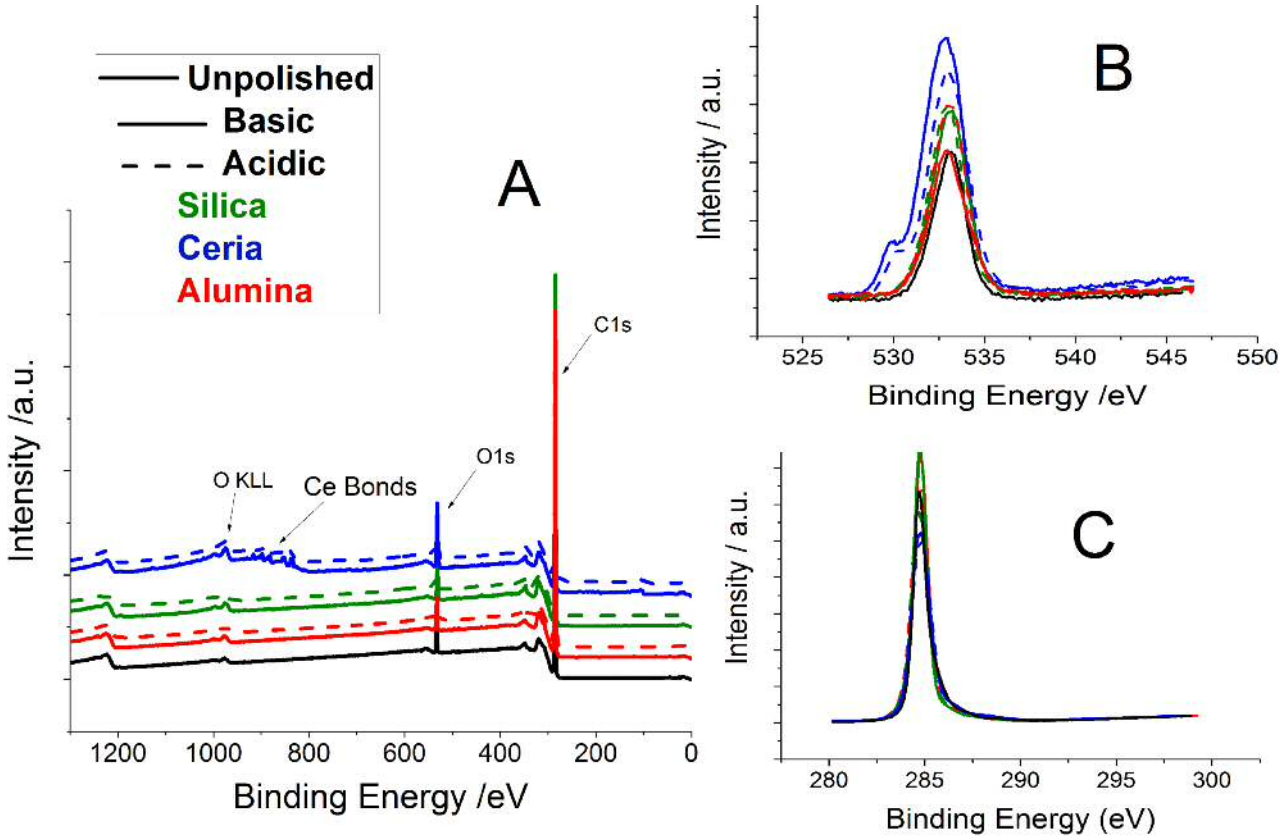

FIGURE 6.11 XPS data of the 6 polished films and an as grown film. Panel A shows a sweep of the binding energy from 0 to 1200 revealing on a broad spectrum what is present on the surface of the diamond films, Panel B shows the O1 peaks and Panel C the C1 peaks. Image taken from from (14).

chemical nature of the technique. There was some variation between the oxidation levels. Those films polished by ceria show the highest increase to its oxygen environment. The film polished with basic alumina shows very little oxygen increase.

6.3.3 DISCUSSION

Thomas *et al* proposed that the CMP of NCD thin films followed a mechanism similar to the CMP of silicon dioxide (136). In this more traditional polishing process, the hydroxide ions within the polishing fluid react with the surface siloxane (Si-O-Si) bonds, creating a silanol based passivation layer $(Si(OH)_4)$ (149) (150). Silica particles within the polishing fluid will then attach themselves to the hydrated groups of the passivation layer. The polishing pad then introduces a shearing force on said silica particles. If the energy from this shearing action is larger than the binding energy, the molecule will be removed resulting in polishing of the surface. Relating this process to diamond then a passivation layer would

TABLE 6.2 The O1s/C1s ratios for the films before and after polishing taken from from (14). The oxygen concentration is seen to increase after polishing for all the films. For all the films polished there was an increase in the oxygen environment on the surface implying the chemical nature of the technique. There was some variation between the oxidation levels.

Polishing slurry	O1/C1 ratio
None	0.1613
Basic alumina	0.1680
Acidic alumina	0.2022
Basic silica	0.2033
Acidic silica	0.2247
Acidic ceria	0.3123
Basic ceria	0.3567

be formed by the increase of carbonyl and hydroxyl groups on the surface allowing the polishing slurry particles to bond to its surface. Figure 6.12 shows a diagram of their proposed model.

Table 6.2 of this study shows that there is an increase in the oxygen content on the surface of all the diamond films, this is regardless of whether an acidic or basic slurry was used. In the case of ceria, which appears to remain on the surface to some degree although not in quantities enough to be observed by AFM or SEM, there is the greatest increase in oxygen content. The increase in oxygen suggests there is a reaction occurring on the surface of the NCD films which could be facilitating the polishing particles bonding to the surface. Although there is no evidence for a passivation layer forming due to carbonyl and hydroxyl groups, otherwise there would have been a greater oxygen content on the surface of the films which were polished with the basic slurries. The basic slurries only had a pH of ≈ 9 so it is possible a stronger basic solution could produce a passivation layer. The polishing mechanism then requires, according to previous literature (151; 136; 149; 150), the following relative differences in binding energies: C-C $<$ C-O $\leq$ Ce-O/Si-O/Al-O. The current accepted values for the various bond strengths are shown in table 6.3. Comparing the bond strength of the Al-O bond and the C-C bond (see table 6.3) the C-C bond is clearly stronger and therefore Al-O should not be capable of polishing the diamond films if this were the polishing mechanism.

This anomaly can be explained by results from Peguiron *et al* (153). The authors performed density functional theory calculations on the degradation of the diamond surface when in contact with silica and silicon, duplicating the model

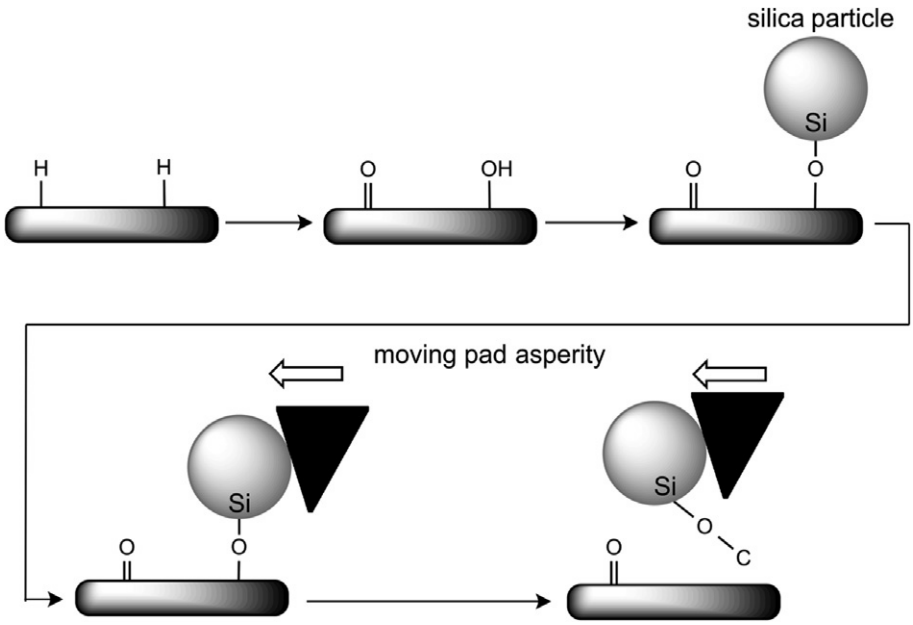

FIGURE 6.12 Proposed polishing mechanism from from (136). The hydrogen surface is oxidised by the polishing fluid and increases the carbonyl (C=O) and hydroxide (OH) content on the surface. As with the CMP of SiO_2, the hydroixde ions facilitate attachment of silica particles to the surface. The shearing force of the rough polishing pad then removes the bond carbon atom from the surface.

TABLE 6.3 The bond strength of the different bond types for each polishing particle (152) (136).

Bond	Strength kJ/mol^{-1}
Ce-O	795
Al-O	511
Si-O	800
O-C	1077
C-C	610

described by Thomas *et al* (136). They discovered that in a silicon particle bonded to diamond system, once a shearing force was applied this would always result in deformation of the silicon. However in the silica bonded to diamond system, once a shearing force was applied C-C bond breakage was shown, although this was not with great regularity. They summarised that this is the result of activation (weakening) of C-C bonds between the terminating zigzag carbon chains and the underlying diamond bulk atoms. This weakening is two-fold requiring first that a pilot atom such as Si, O or H bond to the surface. The results of this study show oxygen bonding to the surface. It is possible that if the silicon is bonding to the surface it is being removed after being cleaned by the standard SC1 process and hydrogen is not detectable by XPS. Then the weakening process requires that the

pilot atom be attached to, or replaced by, a covalent and highly polar material, such as silica not silicon. This connection further weakens the C-C bond resulting in a breakage when a shearing force is applied. They concluded that polishing by this mechanism could also be achieved with alumina.

This study has shown that it is possible to polish NCD films using alumina as predicted. This mechanism could provide an explanation for why ceria does not polish to the same rate as silica. Ceria contains both ionic and covalent bonding, with the ionic bond dominating (154). This variation in bonding could also be the reason that the ceria remains bonded to the diamond film surface where the alternatives do not. It is possible that the covalent bonding whilst not dominant might be enough to provide the C-C bond weakening. Regardless ceria still polishes at a similar or greater rate than the basic alumina slurry.

The model proposed by Perguinon *et al* (153) explains why alumina polishes, and possibly explains why ceria polishes, but it does not explain the variation between the alumina basic and acidic slurries. This variation can be explained if their particle size is considered in regards to the polishing rate, as figure 6.10 clearly shows. This implies that the CMP of NCD thin films follows a contact-area mechanism where the roughness reduction is determined by the contact area of the particles to the sample, hence inversely proportional to the particle size. This relationship has been observed in the CMP of other materials (155), although in cases apart from diamond the density and hardness of the polishing particles play a more significant role (155).

6.4 CONCLUSIONS

This chapter has shown that the CMP of NCD thin films is a chemical process that increases the O1s oxygen content on the surface of the films. Further changes have been proposed to the mechanism of the CMP of NCD thin films. Firstly it has been shown that CMP is not limited to slurries containing silica polishing particles. Three oxide polishing particles, ceria (CeO_2), alumina (Al_2O_3) and silica (SiO_2), were tested under acidic and basic conditions. It was found the acidic alumina slurry polishes at a similar rate as the basic silica and acidic silica slurries, which agrees with separate theoretical predictions. However, the basic alumina polished at a significantly lower rate. This study shows that this is a result of the order of magnitude difference between the diameters of the polishing particles. It was found that of all the various properties of the slurries, including pH and composition, the particle size was a determining factor for the polishing rate. The

particles with a smaller diameter capable of a greater RMS roughness reduction than those with a large diameter. This implies that the CMP of NCD thin films follows a contact-area mechanism where the rate roughness reduction is determined by the contact area of the particles to the sample. Smaller particles are able to bond in greater numbers to the NCD thin films' surface leading to more instances of C-C bond weakening and therefore successful polishing.

CHAPTER 7
CONCLUSION AND FURTHER WORK

The work conducted for this thesis is part of a larger project which aims to first, fabricate and characterise diamond superconducting nano-electro-mechanical systems (NEMS) and superconducting quantum interference devices (SQUIDS); then use these devices to investigate macroscopic quantum states. In order to achieve the final goals of this project initial fabrication and characterisation targets needed to be achieved first. This thesis focuses on three such areas which have been discussed in the past three chapters. Firstly the superconductivity of the BCND films before construction needs to be characterised. Boron doped diamond's behaviour as a superconductor is still an area of active interest. This thesis has two components that focus on characterising particularly superconducting aspects of the BNCD films.

Chapter 4 used an AC susceptibility technique to measure how the critical temperature, the superconducting fraction and critical current density changes with film thickness. The critical temperatures of the BNCD films measured by AC susceptibility were found to be noticeably lower than critical temperature onset and offset values determined by resistivity measurements. It has been shown that for BNCD films magnetic measurements are more in agreement with a T_C defined in relation to the conduction diverging as done by ref. (11). These results also show that, for all the films within the set, the grains are coupled together strongly enough to not show two transitions at these applied fields. Higher applied fields to the thickest sample also did not reveal a second transition.

The volume fraction calculations show that the films are made up of a 100% superconducting material. However, these results also show an unrealistic transition period, looking more like type I superconductors with no vortex state. This

does not mean that the films are not fully superconducting as the method of analysis requires that the film behaves as a homogeneously magnetized ellipsoid with a linear magnetic response; these three requirements usually are not satisfied in superconductors with vortex pinning (105). The result of using this method upon the films seems to be the loss of transition detail only. The agreement of the χ' vs χ'' predictions with the ideal theoretical values of the Brandt model also supports this conclusion. The greater alignment with the theoretical predictions as the field increased for the thickest film and the increase in alignment with film decreasing does suggest that the films are fully superconducting. The thicker film in particular which was measured with higher fields starts to align more closely with the theoretical values from the Brandt model. This suggests that the growth recipe used is able to produce films made of fully superconducting material between the region $160 - 564$ nm.

The peak of χ'' did not reach its saturation point for any of the measured BNCD films. Therefore a true value for J_C could not be calculated for any of these results nor could a comparison be made between the different film thicknesses. A lower boundary value of J_C could only be successfully calculated for the second thinnest film (168 nm) and the thickest film at higher applied fields. For the thickest films at higher fields J_C is 770 ± 90 A/cm^2, 860 ± 95 A/cm^2 and $1.13 \pm 0.12 \times 10^3$ A/cm^2 for 4.51 A/m, 4.99 A/m and 6.01 A/m respectively. For the second thinnest; J_C is 390 ± 45 A/cm^2 and 580 ± 90 A/cm^2 for 0.60 A/m and 0.80 A/m respectively. These values an order of magnitude smaller than literature values available for the J_C of BNCD films (111; 112). $J_C \sim 10^4 A/cm^2$ having been obtained from (111; 112). Ref. (111; 112) calculated these values from M(H) curves, according to the Bean model. Their results compared against temperature and from fields $0 - 2 \times 10^5$ A/m. The values calculated for the thicker film at higher fields are closer comparatively to these literature values than the thinner film. These films from the initial measurements do appear to be following the Brandt model behaviour. Therefore this method could be used to obtain accurate values of J_C for all the films in the thickness varying set, provided they were taken in an AC susceptibility measurement system with a base temperature < 1.9 K. The lower temperature range allowing for the application of higher fields whilst still measuring the full transition.

Chapter 5 measures the temperature dependence of the magnetic relaxation for the thickest film of BNCD film thickness varying set. The results clearly show magnetic relaxation is present within the sample. The temperature dependency

of the S also showed a plateau in its results which is a typical feature that appears in high temperature superconductors. The existence of which is explained by both vortex glass and collective vortex creep, models. The next step in determining which of the two models applies to diamond would further require field dependent measurements.

An effective pinning potential value of the order of meV was calculated for the linearly changing S of BNCD film. This value is a factor of 2 smaller than the only published value of diamond available (13) and typical high temperature measurements. A variation which could be due to the increased thickness and boron concentrations of the sample grown for ref. (13). Alternatively, the variation could be a result of the different measurement processes and ref. (13) not taking account of fluctuations within the film and T_C accordingly.

Chapter 6 was concerned with improving the chemical mechanical polishing (CMP) of the thin films; a necessary production step, which improves device performance, before device construction. This chapter has shown that the CMP of NCD thin films is a chemical process that increases the O1s oxygen content on the surface of the films. Further changes have been proposed to the mechanism of the CMP of NCD thin films. Firstly it has been shown that CMP is not limited to slurries containing silica polishing particles. Three oxide polishing particles, ceria (CeO_2), alumina (Al_2O_3) and silica (SiO_2), were tested under acidic and basic conditions. It was found the acidic alumina slurry polishes at a similar rate as the basic silica and acidic silica slurries, which agrees with separate theoretical predictions. However, the basic alumina polished at a significantly lower rate. This study shows that this is a result of the order of magnitude difference between the diameters of the polishing particles. It was found that of all the various properties of the slurries, including pH and composition, the particle size was a determining factor for the polishing rate. The particles with a smaller diameter capable of a greater RMS roughness reduction than those with a large diameter. This implies that the CMP of NCD thin films follows a contact-area mechanism where the rate roughness reduction is determined by the contact area of the particles to the sample. Smaller particles are able to bond in greater numbers to the NCD thin films' surface leading to more instances of C-C bond weakening and therefore successful polishing.

Each of the three chapters present opportunities for further work. In chapter 4 J_C values were calculated which were an order of magnitude lower than literature values. This was expected given the lack of saturation conditions being met. Since the films showed behaviour in line with the Brandt model this method shows

promise for the calculation of J_C for all the films in the thickness varying set. In order to complete this comparison, data would need to be taken in an AC susceptibility measurement system with a base temperature < 1.9 K. The lower temperature range allowing for the application of higher fields whilst still measuring the full transition. Chapter 5 shows the existence of a plateau in the temperature region. This is a typical feature in high temperature superconductors. In YBCO studies this plateau falls into a specific narrow S range. The next stage into studying this feature would be to look into the field dependence of the plateau S value up to at least 10^6 A/m, the field to which the YBCO samples have been tested (42). Following this, the next questions are whether the plateau appears for the other films in the thickness varying set and if the plateau S value varies. Further work for chapter 6 would be to look into the chemical aspect of the CMP of diamond. This lead to a study by the Cardiff diamond foundry (156) where various redox agents were added to an alkaline SF1 polishing slurry (the same used for the experiments in chapter 4); in order to see if the bonding density of the particles to the diamond surface could be improved. The key result is that the addition of redox agents did not increase the density of oxygen-containing species on the surface but did accelerate the process of attachment and removal of Si or O atoms within the slurry particles to the diamond surface. These results are in line with the model already proposed by Peguiron *et al* (153), discussed in chapter 6. It is clear from references (153; 156; 14) the larger the diamond/silica interface, the higher the probability and rate of wear of the diamond surface. Further discussion can be found in (157).

BIBLIOGRAPHY

[1] M. Imboden and P. Mohanty, "Dissipation in nanoelectromechanical systems," *Physics Reports*, vol. 534, no. 3, pp. 89 – 146, 2014.

[2] S. Giblin, O. Williams, D. Read, and R. Haley, "Driving to the quantum world on a diamond bridge.," *EPSRC Proposal submission*, 2014.

[3] M. Imboden, P. Mohanty, A. Gaidarzhy, J. Rankin, and B. Sheldon, "Scaling of dissipation in megahertz-range micromechanical diamond oscillators," *Applied Physics Letters*, vol. 90, 03 2007.

[4] O. A. Williams, "Nanocrystalline diamond," *Diamond and Related Materials*, vol. 20, pp. 621–640, 2011.

[5] O. Williams, A. Kriele, J. Hees, M. Wolfer, W. MÃijller-Sebert, and C. Nebel, "High young's modulus in ultra thin nanocrystalline diamond," *Chemical Physics Letters*, vol. 495, no. 1, pp. 84 – 89, 2010.

[6] E. A. Ekimov, V. A. Sidorov, E. D. Bauer, N. N. Mel'nik, N. J. Curro, J. D. Thompson, and S. M. Stishov, "Superconductivity in diamond," *Nature*, vol. 428, p. 542, 2004.

[7] E. Bustarret, "Superconducting diamond: an introduction," *physica status solidi (a)*, vol. 205, no. 5, pp. 997–1008, 2008.

[8] T. Bautze, S. Mandal, O. A. Williams, P. Rodére, T. Meunier, and C. Bäuerle, "Superconducting nano-mechanical diamond resonators," *Carbon*, vol. 72, pp. 100 – 105, 2014.

[9] K. C. Schwab and M. L. Roukes, "Putting mechanics into quantum mechanics," *Physics Today*, vol. 58, pp. 36–42, July 2005.

[10] S. Etaki, M. Poot, I. Mahboob, K. Onomitsu, H. Yamaguchi, and H. S. J. van der Zant, "Motion detection of a micromechanical resonator embedded in a d.c. squid," *Nature Physics*, vol. 4, p. 785, 2008.

[11] G. M. Klemencic, J. M. Fellows, J. M. Werrell, S. Mandal, S. R. Giblin, R. A. Smith, and O. A. Williams, "Fluctuation spectroscopy as a probe of granular superconducting diamond films," *Phys. Rev. Materials*, vol. 1, p. 044801, Sep 2017.

[12] G. M. Klemencic, J. M. Fellows, J. M. Werrell, S. Mandal, S. R. Giblin, R. A. Smith, and O. A. Williams, "Observation of a superconducting glass state in granular superconducting diamond," *Submitted to Scientific Reports*, September 2018.

[13] D. Kumar, S. Samanta, K. Sethupathi, and M. S. R. Rao, "Flux pinning and improved critical current density in superconducting boron doped diamond films," *Journal of Physics Communications*, vol. 2, no. 4, p. 045015, 2018.

[14] J. M. Werrell, S. Mandal, E. L. H. Thomas, E. B. Brousseau, R. Lewis, P. Borri, P. R. Davies, and O. A. Williams, "Effect of slurry composition on the chemical mechanical polishing of thin diamond films," *Science and Technology of Advanced Materials*, vol. 18, no. 1, pp. 654–663, 2017. PMID: 29057022.

[15] H. K. Onnes, "Further experiments with liquid helium. c. on the change of electric resistance of pure metals at very low temperatures, etc. iv. the resistance of pure mercury at helium temperatures," *Comm. Phys. Lab. Univ. Leiden*, vol. 120b, 1911.

[16] H. K. Onnes, "Further experiments with liquid helium. d. on the change of electric resistance of pure metals at very low temperatures, etc. v. the disappearance of the resistance of mercury," *Comm. Phys. Lab. Univ. Leiden*, vol. 122b, 1911.

[17] H. K. Onnes, "Further experiments with liquid helium. g. on the electrical resistance of pure metals, etc. vi. on the sudden change in the rate at which the resistance of mercury disappears.," *Comm. Phys. Lab. Univ. Leiden*, vol. 124c, 1911.

[18] F. London and H. London, "The electromagnetic equations of the supraconductor," *Proceedings of the Royal Society of London A: Mathematical, Physical and Engineering Sciences*, vol. 149, no. 866, pp. 71–88, 1935.

[19] A. C. Rose-Innes and E. H. Rhoderick, *Introduction to superconductivity*. Oxford; New York; Toronto; Sydney; Paris; Braunschweig: Pergamon Press, 1st ed., 1969.

[20] J. N. Rjabinin and L. W. Shubnikow, "Magnetic properties and critical currents of supra-conducting alloys," *Nature*, vol. 135, Jan 1935.

[21] J. Bardeen, L. N. Cooper, and J. R. Schrieffer, "Theory of superconductivity," *Phys. Rev.*, vol. 108, pp. 1175–1204, Dec 1957.

[22] F. Dahlem, P. Achatz, O. A. Williams, D. Araujo, E. Bustarret, and H. Courtois, "Spatially correlated microstructure and superconductivity in polycrystalline boron-doped diamond," *Phys. Rev. B*, vol. 82, p. 033306, Jul 2010.

[23] B. Sacépé, C. Chapelier, C. Marcenat, J. Kačmarčik, T. Klein, M. Bernard, and E. Bustarret, "Tunneling spectroscopy and vortex imaging in boron-doped diamond," *Phys. Rev. Lett.*, vol. 96, p. 097006, Mar 2006.

[24] K. Winzer, D. Bogdanov, and C. Wild, "Electronic properties of boron-doped diamond on the border between the normal and the superconducting state," *Physica C: Superconductivity and its Applications*, vol. 432, no. 1, pp. 65 – 70, 2005.

[25] "73 - on the theory of superconductivitiy," in *Collected Papers of L.D. Landau* (D. T. Haar, ed.), pp. 546 – 568, Pergamon, 1965.

[26] L. Gor'kov, "Microscopic derivation of the ginzburg-landau equations in the theory of superconductivity," *JETP*, vol. 9, p. 1364, December 1959.

[27] H. Fröhlich, "Theory of the superconducting state. i. the ground state at the absolute zero of temperature," *Phys. Rev.*, vol. 79, pp. 845–856, Sep 1950.

[28] E. Maxwell, "Isotope effect in the superconductivity of mercury," *Phys. Rev.*, vol. 78, pp. 477–477, May 1950.

[29] C. A. Reynolds, B. Serin, and L. B. Nesbitt, "The isotope effect in superconductivity. i. mercury," *Phys. Rev.*, vol. 84, pp. 691–694, Nov 1951.

[30] D. R. Tilley and J. Tilley, *Superfluidity and Superconductivity*. Techno House, Redcliffe Way, Bristol BS1 6NX, England: IOP Publishing, 3rd ed., 1990.

[31] L. N. Cooper, "Bound electron pairs in a degenerate fermi gas," *Phys. Rev.*, vol. 104, pp. 1189–1190, Nov 1956.

[32] A. T. Hirshfeld, H. A. Leupold, and H. A. Boorse, "Superconducting and normal specific heats of niobium," *Phys. Rev.*, vol. 127, pp. 1501–1507, Sep 1962.

[33] R. L. Dolecek, "Adiabatic magnetization of a superconducting sphere," *Phys. Rev.*, vol. 96, pp. 25–28, Oct 1954.

[34] R. E. Glover and M. Tinkham, "Conductivity of superconducting films for photon energies between 0.3 and $40kT_c$," *Phys. Rev.*, vol. 108, pp. 243–256, Oct 1957.

[35] M. A. Biondi, M. P. Garfunkel, and A. O. McCoubrey, "Millimeter wave absorption in superconducting aluminum," *Phys. Rev.*, vol. 101, pp. 1427–1429, Feb 1956.

[36] W. S. Corak, B. B. Goodman, C. B. Satterthwaite, and A. Wexler, "Atomic heats of normal and superconducting vanadium," *Phys. Rev.*, vol. 102, pp. 656–661, May 1956.

[37] A. Rose-Innes, *Introduction to Superconductivity 2nd Edition*. Oxford; New York; Toronto; Sydney; Paris; Braunschweig: Pergamon Press, 2nd ed., 1978.

[38] P. Anderson, "Theory of dirty superconductors," *Journal of Physics and Chemistry of Solids*, vol. 11, no. 1, pp. 26 – 30, 1959.

[39] A. Abrikosov, "On the magnetic properties of superconductors of the second group," *JETP*, vol. 5, pp. 1174–1182, December 1957.

[40] Y. Takanoa, M. Nagao, I. Sakaguchi, M. Tachiki, T. Hatano, K. Kobayashi, H. Umezawa, and H. Kawarada, "Superconductivity in diamond thin films well above liquid helium temperature," *Appl. Phys. Lett.*, vol. 85, p. 2851, 2004.

[41] Y. Takanoa, M. Nagao, T. Takenouchi, H. Umezawa, I. Sakaguchi, M. Tachiki, and H. Kawarada, "Superconductivity in polycrystalline diamond thin films," *Diamond and Related Materials*, vol. 14, pp. 1936–1938, 2005.

[42] Y. Yeshurun, A. P. Malozemoff, and A. Shaulov, "Magnetic relaxation in high-temperature superconductors," *Rev. Mod. Phys.*, vol. 68, pp. 911–949, Jul 1996.

[43] C. P. Bean, "Magnetization of high-field superconductors," *Rev. Mod. Phys.*, vol. 36, pp. 31–39, Jan 1964.

[44] C. P. Bean, "Magnetization of hard superconductors," *Phys. Rev. Lett.*, vol. 8, pp. 250–253, Mar 1962.

[45] A. I. Larkin and Y. N. Ovchinnikov, "Pinning in type ii superconductors," *Journal of Low Temperature Physics*, vol. 34, pp. 409–428, Feb 1979.

[46] P. W. Anderson, "Theory of flux creep in hard superconductors," *Phys. Rev. Lett.*, vol. 9, pp. 309–311, Oct 1962.

[47] Y. B. Kim, C. F. Hempstead, and A. R. Strnad, "Magnetization and critical supercurrents," *Phys. Rev.*, vol. 129, pp. 528–535, Jan 1963.

[48] Y. B. Kim, C. F. Hempstead, and A. R. Strnad, "Critical persistent currents in hard superconductors," *Phys. Rev. Lett.*, vol. 9, pp. 306–309, Oct 1962.

[49] S. Tennant, "Iv. on the nature of the diamond," *Philosophical Transactions of the Royal Society of London*, vol. 87, pp. 123–127, 1797.

[50] E. L. H. Thomas, *Nanocrystalline diamond for nano-electro-mechanical systems*. PhD thesis, Cardiff University, 2017.

[51] F. P. Bundy, H. P. Bovenkerk, H. M. Strong, and R. H. W. Jr., "Diamond-graphite equilibrium line from growth and graphitization of diamond," *The Journal of Chemical Physics*, vol. 35, no. 2, pp. 383–391, 1961.

[52] H. O. Pierson, *"Chapter 2: The element carbon," in Handbook of Carbon, Graphite, Diamonds and Fullerenes*. Oxford: William Andrew Publishing, 1st ed., 1993.

[53] F. P. Bundy, H. T. Hall, H. M. Strong, and R. H. Wentorf Jun, "Man-made diamonds," *Nature*, vol. 176, p. 51, 1955.

[54] H. Sumiya and S. Satoh, "High-pressure synthesis of high-purity diamond crystal," *Diamond and Related Materials*, vol. 5, no. 11, pp. 1359 – 1365, 1996.

[55] P. W. May, "Diamond thin films: a 21st-century material," *Philosophical Transactions of the Royal Society of London A: Mathematical, Physical and Engineering Sciences*, vol. 358, no. 1766, pp. 473–495, 2000.

[56] V. V. Danilenko, "On the history of the discovery of nanodiamond synthesis," *Physics of the Solid State*, vol. 46, pp. 595–599, Apr 2004.

[57] J. Donnet, E. Fousson, T. Wang, M. Samirant, C. Baras, and M. P. Johnson, "Dynamic synthesis of diamonds," *Diamond and Related Materials*, vol. 9, no. 3, pp. 887 – 892, 2000.

[58] A. Krueger, "The structure and reactivity of nanoscale diamond," *J. Mater. Chem.*, vol. 18, pp. 1485–1492, 2008.

[59] N. R. Greiner, D. S. Phillips, J. D. Johnson, and F. Volk, "Diamonds in detonation soot," *Nature*, vol. 334, p. 440, 1988.

[60] A. Krüger, F. Kataoka, M. Ozawa, T. Fujino, Y. Suzuki, A. Aleksenskii, A. Y. Vul', and E. . Osawa, "Unusually tight aggregation in detonation nanodiamond: Identification and disintegration," *Carbon*, vol. 43, no. 8, pp. 1722 – 1730, 2005.

[61] V. N. Mochalin, O. Shenderova, D. Ho, and Y. Gogotsi, "The properties and applications of nanodiamonds," *Nature Nanotechnology*, vol. 7, p. 11, 2011.

[62] J. C. Angus, A. Argoitia, R. Gat, Z. Li, M. Sunkara, L. Wang, and Y. Wang, "Chemical vapour deposition of diamond," *Philosophical Transactions of the Royal Society of London A: Mathematical, Physical and Engineering Sciences*, vol. 342, no. 1664, pp. 195–208, 1993.

[63] M. N. R. Ashfold, P. W. May, C. A. Rego, and N. M. Everitt, "Thin film diamond by chemical vapour deposition methods," *Chem. Soc. Rev.*, vol. 23, pp. 21–30, 1994.

[64] O. A. Williams, O. Douhéret, M. Daenen, K. Haenen, E. Ōsawa, and M. Takahashi, "Enhanced diamond nucleation on monodispersed nanocrystalline diamond," *Chemical Physics Letters*, vol. 445, no. 4-6, pp. 255–258, 2007.

[65] X. Jiang, K. Schiffmann, and C.-P. Klages, "Nucleation and initial growth phase of diamond thin films on (100) silicon," *Phys. Rev. B*, vol. 50, pp. 8402–8410, Sep 1994.

[66] P. Smereka, X. Li, G. Russo, and D. Srolovitz, "Simulation of faceted film growth in three dimensions: microstructure, morphology and texture," *Acta Materialia*, vol. 53, no. 4, pp. 1191–1204, 2005.

[67] D. Pines, "Superconductivity in the periodic system," *Phys. Rev.*, vol. 109, pp. 280–287, Jan 1958.

[68] M. L. Cohen, "Superconductivity in many-valley semiconductors and in semimetals," *Phys. Rev.*, vol. 134, pp. A511–A521, Apr 1964.

[69] R. D.Parks, *M. L. Cohen, in: Superconductivity, Vol. 1*. New York: Marcel Decker, 1st ed., 1964.

[70] R. A. Hein, J. W. Gibson, R. Mazelsky, R. C. Miller, and J. K. Hulm, "Superconductivity in germanium telluride," *Phys. Rev. Lett.*, vol. 12, pp. 320–322, Mar 1964.

[71] J. F. Schooley, W. R. Hosler, and M. L. Cohen, "Superconductivity in semiconducting srtio$_3$," *Phys. Rev. Lett.*, vol. 12, pp. 474–475, Apr 1964.

[72] E. Bustarret, C. Marcenat, P. Achatz, J. Kačmarčik, F. Lévy, A. Huxley, L. Ortéga, E. Bourgeois, X. Blase, D. Débarre, and J. Boulmer, "Superconductivity in doped cubic silicon," *Nature*, vol. 444, pp. 465–468, November 2006.

[73] J. Kačmarčik, C. Marcenat, C. Cytermann, A. Ferreira da Silva, L. Ortega, F. Gustafsson, J. Marcus, T. Klein, E. Gheeraert, and E. Bustarret, "Superconductivity in boron-doped homoepitaxial (001)-oriented diamond layers," *physica status solidi (a)*, vol. 202, no. 11, pp. 2160–2165, 2004.

[74] E. Bustarret, J. Kačmarčik, C. Marcenat, E. Gheeraert, C. Cytermann, J. Marcus, and T. Klein, "Dependence of the superconducting transition temperature on the doping level in single-crystalline diamond films," *Phys. Rev. Lett.*, vol. 93, p. 237005, Dec 2004.

[75] Y. Takano, "Superconductivity in cvd diamond films," *Journal of Physics: Condensed Matter*, vol. 21, May 2009.

[76] W. Gajewski, P. Achatz, O. A. Williams, K. Haenen, E. Bustarret, M. Stutzmann, and J. A. Garrido, "Electronic and optical properties of boron-doped nanocrystalline diamond films," *Phys. Rev. B*, vol. 79, p. 045206, Jan 2009.

[77] K. Winzer, D. Bogdanov, and C. Wild, "Electronic properties of boron-doped diamond on the border between the normal and the superconducting state," *Physica C: Superconductivity and its Applications*, vol. 432, pp. 65–70, Mar 2005.

[78] G. Baskaran, "Resonating valence bond states in 2 and 3d: Brief history and recent examples," *Indian Journal of Physics*, vol. 89, pp. 583–592, 2006.

[79] P. W. ANDERSON, "The resonating valence bond state in la2cuo4 and superconductivity," *Science*, vol. 235, no. 4793, pp. 1196–1198, 1987.

[80] J. Nakamura, N. Yamada, K. Kuroki, T. Oguchi, K. Okada, Y. Takano, M. Nagao, I. Sakaguchi, T. Takenouchi, H. Kawarada, R. C. C. Perera, and D. L. Ederer, "Holes in the valence band of superconducting boron-doped diamond film studied by soft x-ray absorption and emission spectroscopy," *Journal of the Physical Society of Japan*, vol. 77, no. 5, p. 054711, 2008.

[81] S. HÃijfner, M. A. Hossain, A. Damascelli, and G. A. Sawatzky, "Two gaps make a high-temperature superconductor?," *Reports on Progress in Physics*, vol. 71, no. 6, p. 062501, 2008.

[82] R. Sharma, *Superconductivity Basics and Applications to Magnets*. Cham, Heidelberg, New York, Dordrecht, London: Springer Series in Materail Science, 1st ed., 2015.

[83] C. Varma, "Mind the pseudogap," *Nature*, vol. 468, p. 184, 2010.

[84] T. Yoshida, M. Hashimoto, S. Ideta, A. Fujimori, K. Tanaka, N. Mannella, Z. Hussain, Z.-X. Shen, M. Kubota, K. Ono, S. Komiya, Y. Ando, H. Eisaki, and S. Uchida, "Universal versus material-dependent two-gap behaviors of the high-T_c cuprate superconductors: Angle-resolved photoemission study of $la_{2-x}sr_xcuo_4$," *Phys. Rev. Lett.*, vol. 103, p. 037004, Jul 2009.

[85] J. Mareš, P. Hubík, M. Nesládek, D. Kindl, and J. Krištofik, "Weak localization - precursor of unconventional superconductivity in nanocrystalline boron-doped diamond," *Diamond and Related Materials*, vol. 15, no. 11, pp. 1863 – 1867, 2006. Proceedings of the joint 11th International Conference on New Diamond Science and Technology and the 9th Applied Diamond Conference 2006.

[86] J. Mareš, M. Nesládek, P. Hubík, D. Kindl, and J. Krištofik, "On unconventional superconductivity in boron-doped diamond," *Diamond and Related Materials*, vol. 16, no. 1, pp. 1 – 5, 2007.

[87] T. Nishizaki, Y. Takano, M. Nagao, T. Takenouchi, H. Kawarada, and N. Kobayashi, "Scanning tunneling microscopy and spectroscopy studies of superconducting boron-doped diamond films," *Science and Technology of Advanced Materials*, vol. 7, pp. S22 – S26, 2006.

[88] O. A. Williams, O. Douhéret, M. Daenen, K. Haenen, E. . Osawa, and M. Takahashi, "Enhanced diamond nucleation on monodispersed nanocrystalline diamond," *Chemical Physics Letters*, vol. 445, no. 4, pp. 255 – 258, 2007.

[89] B. L. Willems, G. Zhang, J. Vanacken, V. V. Moshchalkov, S. D. Janssens, K. Haenen, and P. Wagner, "Granular superconductivity in metallic and insulating nanocrystalline boron-doped diamond thin films," *Journal of Physics D: Applied Physics*, vol. 43, no. 37, p. 374019, 2010.

[90] G. M. Klemencic, S. Mandal, J. M. Werrell, S. R. Giblin, and O. A. Williams, "Superconductivity in planarised nanocrystalline diamond films," *Science and Technology of Advanced Materials*, vol. 18, no. 1, pp. 239–244, 2017. PMID: 28458745.

[91] M. Nikolo, "Superconductivity: A guide to alternating current susceptibility measurements and alternating current susceptometer design," *American Journal of Physics*, vol. 63, 1995.

[92] Quantum and Design, *Physical Property Measurement System AC Measurement System (ACMS) Option User's Manual*. California, United States: Author, 4th ed., 2003.

[93] M. Youssif, A. Bahgat, and I. Ali, "Ac magnetic susceptibility technique for the characterization of high temperature superconductors," *Egyptian Journal of Solids*, vol. 23, no. 2, pp. 231–250, 2000.

[94] B. Lorenz, R. L. Meng, and C. W. Chu, "High-pressure study on mgb_2," *Phys. Rev. B*, vol. 64, p. 012507, Jun 2001.

[95] R. B. Goldfarb, M. Lelental, and C. A. Thompson, *Alternating-Field Susceptometry and Magnetic Susceptibility of Superconductors*, pp. 49–80. Boston, MA: Springer US, 1991.

[96] D. Martien, *Introduction to AC Susceptability*. Quantum Design.

[97] W. M. Haynes, *CRC Handbook of Chemistry and Physics*. Boca Raton, FL: CRC Press: CRC Press, 97th edition ed., 2016.

[98] R. Masuda, S. Kitao, Y. Kobayashi, M. Seto, R. Haruki, X.-W. Zhang, and S. Kishimoto, "Dependence of incoherent nuclear resonant scattering of synchrotron radiation on the number of resonant nuclei," *Journal of the Physical Society of Japan*, vol. 76, no. 2, p. 023710, 2007.

[99] M. P. Sarachik, D. R. He, W. Li, M. Levy, and J. S. Brooks, "Magnetic properties of boron-doped silicon," *Phys. Rev. B*, vol. 31, pp. 1469–1477, Feb 1985.

[100] R. König, A. Schindler, and T. Herrmannsdörfer, "Superconductivity of compacted platinum powder at very low temperatures," *Phys. Rev. Lett.*, vol. 82, pp. 4528–4531, May 1999.

[101] R. Singh, R. Lal, U. C. Upreti, D. K. Suri, A. V. Narlikar, V. P. S. Awana, J. Albino Aguiar, and M. Shahabuddin, "Superconductivity in zn-doped tetragonal $LaBaCaCu_3o_{7-ffi}$ systems," *Phys. Rev. B*, vol. 55, pp. 1216–1222, Jan 1997.

[102] T. Puig, A. Palau, X. Obradors, E. Pardo, C. Navau, A. Sanchez, C. Jooss, K. Guth, and H. C. Freyhardt, "The identification of grain boundary networks of distinct critical current density in yba 2 cu 3 o 7âĹŠ x coated conductors," *Superconductor Science and Technology*, vol. 17, no. 11, p. 1283, 2004.

[103] P. Laurent, J. F. Fagnard, B. Vanderheyden, N. H. Babu, D. A. Cardwell, M. Ausloos, and P. Vanderbemden, "An ac susceptometer for the characterization of large, bulk superconducting samples," *Measurement Science and Technology*, vol. 19, no. 8, p. 085705, 2008.

[104] C. Poole, H. Farach, and C. R.J., *Magnetic Properties, In: Superconductivity*. 84 Theobald's Road, London WC1X 8RR, UK,: Elsevier Ltd., 2nd ed., 2007.

[105] E. H. Brandt, "Superconductor disks and cylinders in an axial magnetic field. i. flux penetration and magnetization curves," *Phys. Rev. B*, vol. 58, pp. 6506–6522, Sep 1998.

[106] E. Pardo, D.-X. Chen, and A. Sanchez, "Demagnetizing factors for completely shielded rectangular prisms," *Journal of Applied Physics*, vol. 96, pp. 5365–5369, Nov. 2004.

[107] T. Herzog, H. A. Radovan, P. Ziemann, and E. H. Brandt, "Experimental test of theories describing the magnetic ac susceptibility of differently shaped superconducting films: Rectangles, squares, disks, and rings patterned from $yba_2cu_3o_{7-\delta}$ films," *Phys. Rev. B*, vol. 56, pp. 2871–2881, Aug 1997.

[108] B. J. Jönsson, K. V. Rao, S. H. Yun, and U. O. Karlsson, "Method to extract the critical current density and the flux-creep exponent in high-T_c thin films using ac susceptibility measurements," *Phys. Rev. B*, vol. 58, pp. 5862–5867, Sep 1998.

[109] M. Wurlitzer, M. Lorenz, K. Zimmer, and P. Esquinazi, "ac susceptibility of structured $yba_2cu_3o_7$ thin films in transverse magnetic ac fields," *Phys. Rev. B*, vol. 55, pp. 11816–11822, May 1997.

[110] J. R. Clem and A. Sanchez, "Hysteretic ac losses and susceptibility of thin superconducting disks," *Phys. Rev. B*, vol. 50, pp. 9355–9362, Oct 1994.

[111] G. Zhang, S. Turner, E. Ekimov, J. Vanacken, M. Timmermans, T. Samuely, V. Sidorov, S. Stishov, Y. Lu, B. Deloof, B. Goderis, G. Tendeloo, J. Vondel, and V. Moshchalko, "Global and local superconductivity in boron-doped granular diamond," *Adv. Mater.*, vol. 26, pp. 2034–2040, 2014.

[112] K. Natsui, T. Yamamoto, T. Watanabe, Y. Kamihara, and Y. Einaga, "Modulation of critical current density in polycrystalline boron-doped diamond by surface modification," *Physica Status Solidi (B) Basic Research*, vol. 250, no. 9, pp. 1943–1949, 2013. cited By 5.

[113] J. Friedel, P. G. De Gennes, and J. Matricon, "Nature of the driving force in flux creep phenomena," *Applied Physics Letters*, vol. 2, no. 6, pp. 119–121, 1963.

[114] M. F. Schmidt, N. E. Israeloff, and A. M. Goldman, "Applicability of high-t_c paradigms to magnetic relaxation and irreversibility in superconducting nb," *Phys. Rev. B*, vol. 48, pp. 3404–3416, Aug 1993.

[115] A. Gurevich and H. Küpfer, "Time scales of the flux creep in superconductors," *Phys. Rev. B*, vol. 48, pp. 6477–6487, Sep 1993.

[116] M. P. A. Fisher, "Vortex-glass superconductivity: A possible new phase in bulk high-t_c oxides," *Phys. Rev. Lett.*, vol. 62, pp. 1415–1418, Mar 1989.

[117] M. V. Feigel'man, V. B. Geshkenbein, A. I. Larkin, and V. M. Vinokur, "Theory of collective flux creep," *Phys. Rev. Lett.*, vol. 63, pp. 2303–2306, Nov 1989.

[118] I. Quantum Design, *Vibrating Sample Magnetometer (VSM) Option UserâĂŹs Manual*. California, United States: Author, 2011.

[119] Q. Design, *Physical Property Measurement System Hardware Manual*. California, United States: Author, 2011.

[120] A. Malozemoff, "Flux creep in high temperature superconductors," *Physica C: Superconductivity*, vol. 185-189, pp. 264 – 269, 1991.

[121] L. Miu, D. Miu, T. Petrisor, A. El Tahan, G. Jakob, and H. Adrian, "Origin of the plateau in the temperature dependence of the normalized magnetization relaxation rate in disordered high-temperature superconductors," *Phys. Rev. B*, vol. 78, p. 212508, Dec 2008.

[122] X. Huang, X. Feng, C. Zorman, M. Mehregany, and M. Roukes, "Vhf, uhf and microwave frequency nanomechanical resonators," *New Journal of Physics*, vol. 7, 2005.

[123] O. Ergincan, G. Palasantzas, and B. J. Kooi, "Influence of surface modification on the quality factor of microresonators," *Phys. Rev. B*, vol. 85, p. 205420, May 2012.

[124] I. Avci, B. Algul, R. Akram, A. Bozbey, M. Tepe, and D. Abukay, "Signal performance of dc-squids with respect to ybco thin film deposition rate," *Sensors and Actuators A: Physical*, vol. 153, 2009.

[125] W. L. Liu, M. Shamsa, I. Calizo, A. A. Balandin, V. Ralchenko, A. Popovich, and *et al.*, "Thermal conduction in nanocrystalline diamond films: Effects of the grain boundary scattering and nitrogen doping," *Applied Physics Letters*, vol. 89, no. 17, p. 171915, 2006.

[126] D. Bhusari, J. Yang, T. Wang, S. Lin, K. Chen, and L. Chen, "Highly transparent nano-crystalline diamond films grown by microwave cvd," *Solid State Communications*, vol. 107, no. 6, pp. 301–305, 1998.

[127] O. Williams, A. Kriele, J. Hees, M. Wolfer, W. M*ü*ller-Sebert, and C. Nebel, "High youngs modulus in ultra thin nanocrystalline diamond," *Chemical Physics Letters*, vol. 495, no. 1-3, pp. 84–89, 2010.

[128] J. G. Rodriguez-Madrid, G. F. Iriarte, J. Pedros, O. A. Williams, D. Brink, and F. Calle, "Super-high-frequency saw resonators on aln/diamond," *IEEE Electron Device Letters*, vol. 33, pp. 495–497, April 2012.

[129] Y. Chen and L. Zhang, *Polishing of Diamond Materials*. Portalnd: Springer Series, 1st ed. ed., 2013.

[130] S. E. Grillo and J. E. Field, "The polishing of diamond," *Journal of Physics D: Applied Physics*, vol. 30, no. 2, p. 202, 1997.

[131] B. S. El-Dasher, J. J. Gray, J. W. Tringea, J. Biener, A. V. H. C. Wild, E. WÃűrner, and *et al.*, "Crystallographic anisotropy of wear on a polycrystalline diamond surface," *Applied Physics Letters*, vol. 88, pp. 241915–1 – 241915–3, 2006.

[132] U. Bögli, A. Blatter, S. Pimenov, E. Obraztsova, A. Smolin, M. Maillat, and *et al.*, "Tribological properties of smooth polycrystalline diamond films," *Diamond and Related Materials*, vol. 4, no. 7, pp. 1009–1019, 1995.

[133] Y. Chen and L. Zhang, *Polishing of Diamond Materials*. Portalnd: Springer Series, 1st ed. ed., 2013.

[134] Q. H. Fan, J. Grácio, and E. Pereira, "Residual stresses in chemical vapour deposited diamond films," *Diamond and Related Materials*, vol. 9, no. 9âĂŞ10, pp. 1739–1743, 2000.

[135] M. J. Edwards, C. R. Bowen, D. W. E. Allsopp, and A. C. E. Dent, "Modelling wafer bow in silicon-polycrystalline cvd diamond substrates for gan-based devices," *Journal of Physics D: Applied Physics*, vol. 43, no. 38, p. 385502, 2010.

[136] E. L. H. Thomas, G. W. Nelson, S. Mandal, J. S. Foord, and O. A. Williams, "Chemical mechanical polishing of thin film diamond," *Carbon*, vol. 68, pp. 473–479, 2014.

[137] P. B. Zantye, A. Kumar, and A. Sikder, "Chemical mechanical planarization for microelectronics applications," *Materials Science and Engineering: R: Reports*, vol. 45, no. 3-6, pp. 89–220, 2004.

[138] E. L. H. Thomas, S. Mandal, E. B. Brousseau, and O. A. Williams, "Silica based polishing of (100) and (111) single crystal diamond," *Science and Technology of Advanced Materials*, vol. 15, no. 3, p. 035013, 2014.

[139] M. R. Oliver, D. Evans, D. Stein, T. Tucker, D. B. James, K. Robinson, and *et al.*, *Chemical-Mechanical, Planarization of Semiconductor Materials*. Portalnd: Springer Series, 1st ed. ed., 2003.

[140] Y. Chen and L. Zhang, *Polishing of Diamond Materials*. Portalnd: Springer Series, 1st ed. ed., 2013.

[141] C. L. Neslen, W. C. Mitchel, and R. L. Hengehold, "Effects of process parameter variations on the removal rate in chemical mechanical polishing of 4h-sic," *Journal of Electronic Materials*, vol. 30, pp. 1271–1275, 2001.

[142] Y. Ahn, J. Yoon, C. Baek, and Y. Kim, "Chemical mechanical polishing by colloidal silica-based slurry for micro-scratch reduction," *Wear*, vol. 257, pp. 785–789, 2004.

[143] S. V. Babu, A. Jindal, and Y. Li, "Chemical-mechanical planarization of cu and ta," *JOM*, vol. 53, no. 6, pp. 50–52, 2001.

[144] J. McGrath and C. Davis, "Polishing pad surface characterisation in chemical mechanical planarisation," *Journal of Materials Processing Technology*, vol. 153-154, pp. 666–673, 2004.

[145] P.-N. Volpe, P. Muret, F. Omnes, J. Achard, F. Silva, O. Brinza, and A. Gicquel, "Defect analysis and excitons diffusion in undoped homoepitaxial diamond films after polishing and oxygen plasma etching," *Diamond and related materials*, vol. 18, no. 10, pp. 1205–1210, 2009.

[146] I. Friel, S. Clewes, H. Dhillon, N. Perkins, D. Twitchen, and G. Scarsbrook, "Control of surface and bulk crystalline quality in single crystal diamond grown by chemical vapour deposition," *Diamond and related materials*, vol. 18, no. 5, pp. 808–815, 2009.

[147] D. Wu, Y. C. Ma, Z. L. Wang, Q. Luo, C. Z. Gu, N. L. Wang, C. Y. Li, X. Y. Lu, and Z. S. Jin, "Optical properties of boron-doped diamond," *Physical review. B Condensed matter and materials physics.*, vol. 73, no. 1, 2006.

[148] G. Zhang, S. D. Janssens, J. Vanacken, M. Timmermans, J. Vacík, G. W. Ataklti, W. Decelle, W. Gillijns, B. Goderis, K. Haenen, P. Wagner, and V. V. Moshchalkov, "Role of grain size in superconducting boron-doped nanocrystalline diamond thin films grown by cvd," *Physical review. B Condensed matter and materials physics.*, vol. 84, no. 21, 2011.

[149] M. Krishnan, J. W. Nalaskowski, and L. M. Cook, "Chemical mechanical planarization: Slurry chemistry, materials, and mechanisms," *Chemical Reviews*, vol. 110, pp. 178–204, 2010.

[150] H. Hochenga, H. Y. Tsaia, and Y. T. Sub, "Modelling and experimental analysis of the material removal rate in the chemical mechanical planarization of dielectric films and bare silicon wafers," *The Electrochemical Society*, vol. 148, pp. G581–G586, 2001.

[151] N. K. Penta, P. R. D. Veera, and S. V. Babu, "Role of poly(diallyldimethylammonium chloride) in selective polishing of polysilicon over silicon dioxide and silicon nitride films," *Langmuir*, vol. 27, pp. 3502–3510, 2011.

[152] D. R. Lide, *'Section 9' CRC Handbook of Chemistry and Physics*. CRC Press, 84th ed. ed., 2003-2004.

[153] A. Peguiron, G. Moras, M. Walter, H. Uetsuka, L. Pastewka, and M. Moseler, "Activation and mechanochemical breaking of c-c bonds initiate wear of diamond (110) surfaces in contact with silica," *Carbon*, vol. 98, pp. 474–483, 2016.

[154] H. Nakamatsu, T. Mukoyama, and H. Adachi, "Ionic and covalent bonds in ceo2 crystal," *Chemical Physics Letters*, vol. 247, no. 1, pp. 168–172, 1995.

[155] W. Choi, J. Abiade, S.-M. Lee, and R. K. Singh, "Effects of slurry particles on silicon dioxide cmp," *Journal of the Electrochemical Society*, vol. 151, pp. G512–G522, 2004.

[156] S. Mandal, E. L. Thomas, L. Gines, D. Morgan, J. Green, B. Brousseau, Emmanuel, and O. Williams, "Redox agent enhanced chemical mechanical polishing of thin film diamond," *Carbon*, vol. 130, pp. 25–30, April 2018.

[157] S. Mandal, E. L. Thomas, G. M. Klemencic, J. Ash, B. Brousseau, Emmanuel, and O. Williams, *Chemical Mechanical Polishing of Nanocrystalline Diamond, In "Novel Aspects of Diamond"*. Switzerland AG: Springer Nature, 1st ed., 2019.